Optical Vortices:

Angular Momentum of Light,

Energy Propagation, and Imaging

by

Henry Sztul

A dissertation submitted to the Graduate Faculty in Physics in partial fulfillment of the requirements for the degree of Doctor of Philosophy, The City University of New York.

2008

This manuscript has been read and accepted for the Graduate Faculty in Physics in satisfaction of the dissertation requirement for the degree of Doctor of Philosophy.

Date	Distinguished Prof. Robert R. Alfano Chair of Examining Committee
Date	Prof. Steven G. Greenbaum Executive Officer

Prof. J. Gersten

Prof. S. Gayen

Prof. M. Lenzner

Prof. V. Menon

Dr. W. Wang
Supervisory Committee

THE CITY UNIVERSITY OF NEW YORK

Abstract

Optical Vortices:

Angular Momentum of Light,

Energy Propagation, and Imaging

by

Henry Sztul

Thesis Advisor: Distinguished Professor Robert R. Alfano

The aim of this thesis is to study salient properties of optical vortices. Optical vortices are a class of solution to Maxwell's equations, some having helical wavefronts and bear orbital angular momentum. Methods of generation of ultrashort and polychromatic optical vortices for use in imaging and spectroscopy are discussed. A new imaging technique that utilizes the optical force associated with a vortex is shown to improve image contrast in a turbid medium. Two new classes of beams are shown to have vortices and carry some well defined angular momentum.

In this thesis, I begin by laying down the mathematical origins of optical vortices and the angular momentum of light. Spin and orbital angular momentum are discussed and shown to be associated with Laguerre-Gaussian (LG) beams. Interesting properties of these beams are explored including an experimental and theoretical demonstration of Young's double-slit experiment. The azimuthal phase variation of the LG beam is taken into account when analyzing the interference due to the two slits.

A method of angular dispersion compensation is used to generate femtosecond LG beams. This thesis reports on the first autocorrelation measurements of LG beams. This compensation method is also used to generate supercontinuum vortices. The

white light vortices have tremendous potential in applications to optical spectroscopy with orbital angular momentum states.

A new technique is used to image through turbid media that relies on the optical forces associated with a high intensity optical vortex "guide" beam to drag scattering particles out of the path of a low intensity "signal" beam. First the transverse forces due to a Gaussian beam are shown to degrade imaging by pulling scatterers into the path of a second "signal" beam.

Finally, two new classes of optical waves are explored. A new cylindrical vector mode is described and classified as a hybrid-azimuthal polarization imaginary (HAPi) mode that has an azimuthally varying polarization including linear and circular polarization that gives rise to an azimuthally varying angular momentum. The propagation dynamics of optical Airy beams are also numerically analyzed and discussed. This class of beam is shown to have varying linear and angular momentum.

Dedicated to my wife, Rachel
Mahna-Mahna

Acknowledgments

First, I would like to thank my advisor, Robert Alfano for giving me the opportunity to pursue this research. I am very thankful for the time he has devoted to my research interests and for the freedom that he gave me to develop as a scientist. I thoroughly enjoyed our time spent discussing fundamental questions arising from optical vortices and the difficult problems that arise with this relatively new field in optics. The time he spent reviewing this dissertation and publications along the way is very appreciated.

I would like to thank the members of the IUSL that have helped me leading up to this dissertation. I would like to thank Ms. S. Kartazayeva, Dr. V Kartazayev, Dr. I. Zeylikovich, Dr. M. Alrubauee, Ms. C. Liu, Dr. X. Ni, and Mr. Yuri Budansky for their help with helpful discussion, experimental setup and apparatus. I would especially like to thank Dr. Wubao Wang for continual support throughout my graduate studies. Thanks also goes out to the members of my committee for their time and patience in my navigation through this process.

Thanks must also go to four people that helped me find my passion in the sciences. Mrs. Sandy Bornstein and Mr. Adam Holley were instrumental in guiding me through high school science in my chaotic endeavor that become the intellectual focus of my career to this point. I would also like to thank Professor Enrique "Kiko" Galvez, my mentor at Colgate University in sunny Hamilton, NY. I must acknowledge Kiko as the source of my love of donuts. I value my time spent in the basement of Lathrop and our ongoing friendship. My scientific experience at Colgate was also made complete through the help, encouragement, and friendship of Vic Mansfield. Vic recently lost his fight with cancer. His guidance, good nature, and insight into the connections between modern physics and religion will be missed.

I have been in school, in one way or another, for a very long time. Throughout the whole journey from Pre-K to Ph.D., my family has encouraged me and taken a direct interest in whatever it was I was studying. I am grateful to my parents and grandparents for facilitating this journey in education that has led to a doctoral dissertation on optical vortices (which I can only explain to them "donuts" made of light).

I am very fortunate that during my pursuit of this degree I succeeded in my pursuit of my wonderful wife, Rachel. She too has encouraged me along the way (despite not "getting it" when I talk physics sometimes). Her help in pushing me through the last couple years of life as a graduate student was instrumental in the completion of this work.

Finally, I would like to thank the NASA Center of Optical Sensing and Imaging, Corning Inc., the Graduate Center of the City University of New York, and the Institute of Ultrafast Spectroscopy and Lasers for their financial support.

Contents

List of Figures

Chapter 1

Introduction

1.1 Overview

Over the years scientists in a variety of disciplines have used the properties of light to investigate the inner workings of the physical, chemical, and biological worlds. Physicists, biologists, chemists, and astronomers have used the key properties of light in their investigation into how the universe in which we live evolves. These key properties of light include: intensity, frequency, wavelength, polarization, and coherence. It has been shown that polarization of light falls under a larger class of properties now known as the angular momentum of light [1]. Recently, the spatial and phase structure of light was shown to be related to the angular momentum and has also begun to be used in these studies [2].

From hurricanes to whirlpools, vortices have captivated peoples interest for millennia. *Optical vortices* are beams of twisted light that have phase or polarization singularities. Such beam profiles can be twisted like a corkscrew about the axis of travel and have zero intensity at their center. The vortex has a number associated with it know as the optical charge that represents the number of times the waves twist in one wavelength. The higher this number the faster the light spins around its axis and the larger the dark region at the center of the beam becomes. Wave dislocations and singularities were first explored by Nye and Berry in 1973 [3] and optical vortices were experimentally realized optically as carrying orbital angular momentum in the early 1990s [2, 4, 5].

Laser beams with optical vortices have emerged as a new and exciting form of light that has a varying phase structure as it propagates through space. These beams with helical wavefronts are shown to have orbital angular momentum (OAM), much like circularly polarized light has spin angular momentum (SAM), and that angular momentum can be transferred to matter. The amount of OAM a beam of light carries is proportional to how much the phase gradient of the light varies. This can be thought of as directly analogous to the angular momentum shown to be associated with circularly polarized light, known as SAM. Experimentally beams of light with spin and orbital angular momentum have both been realized. Light with circular polarization was shown to have SAM by Beth in 1936 [1] when a birefringent plate was made to rotate when hit with circularly polarized light. Reversing the helicity of the polarization resulted in reversing the direction of rotation of the hanging birefringent plate. Orbital angular momentum has been seen by the rotation of micro-particles

[6] and by Bose-Einstein condensates that are made to rotate when they are in the path of such beams of light [7, 8]. OAM has even been observed in single photon experiments [9]. New communications protocols can now be developed because of the ability to control an entirely new degree of freedom, the winding number [10]. Ultrafast uses of these helical beams are an unexplored territory that will lead to new dynamical processes involving orbital angular momentum in addition to spin.

The potential for the use of OAM in experiments is extraordinary because where as SAM, or polarization, of light lies in a two-dimensional basis (left- and right-circular polarization), OAM forms an infinite dimensional basis equal to the charge, or winding number, of the vortex beam. A number of possible experiments and applications using orbital angular momentum nature of light have yet to be exploited. Two areas in particular that lend themselves to be explored with beams of light with orbital angular momentum are imaging and spectroscopy.

1.1.1 Statement of thesis

This thesis focuses on the salient features of vortex beams by investigating the effect of the orbital angular momentum of light and spatial profiles in light-matter interactions. This investigation aims to show: optical imaging through turbid media is improved by use of optical vortex beams; and matter can be shown to be affected by optical vortex beams using spectroscopic techniques.

This research focuses on theoretical and experimental aspects of beams of light that have angular momentum. Chapter 1 of this thesis first shows the origins of the angular momentum of light and several solutions to Maxwell's equations that carry angular momentum and shows methods of generating these beams.

Chapter 2 describes, theoretically and experimentally, how light with angular momentum diffracts. Diffraction due to double slits is explored.

Chapter 3 shows the generation of femtosecond Laguerre-Gaussian beams that carry orbital angular momentum and the characterization of the pulse width of such beams. Chapter 4 extends this technique to generating Laguerre-Gaussian supercontinuum for applications in spectroscopy using orbital angular momentum states.

Chapter 5 shows experimentally that these vortex beams can be used to obtain information in a scattering medium.

Chapter 6 describes the field and angular momentum of hybrid-azimuthal beams and their generation for spectroscopy and imaging applications. The new, simple method shown in this thesis relies on spinning a single mode fiber.

Chapter 7 investigates the propagation of a class of beams, known as accelerating Airy beams, that are shown in this thesis to carry a superposition of angular momentum.

Finally, chapter 8 will discuss the possible direction of future work with light that has orbital angular momentum.

1.2 Principles of light with angular momentum

1.2.1 Maxwell's equations and the paraxial approximation

In a source free space electromagnetic radiation is described by Maxwell's equations,[84]

$$\nabla \cdot \vec{E} = 0 \tag{1.1}$$

$$\nabla \cdot \vec{B} = 0 \tag{1.2}$$

$$\nabla \times \frac{1}{\mu_o}\vec{B} = \frac{\epsilon_o}{c}\frac{\partial \vec{E}}{\partial t} \tag{1.3}$$

$$\nabla \times \vec{E} = -\frac{1}{c}\frac{\partial \vec{B}}{\partial t} \tag{1.4}$$

Taking the time derivative of Eq. 1.3, the curl of Eq. 1.4, and equating like terms we get the wave equation for the electric field,

$$\nabla^2 \vec{E} - \frac{1}{v^2}\frac{\partial^2 \vec{E}}{\partial t^2} = 0 \tag{1.5}$$

where $v = \frac{c}{\sqrt{\mu\epsilon}}$ is the speed of the wave of the $\vec{E}$-field. Using separation of variables, we can define $\vec{E}(x, y, z; t) = \vec{A}(x, y, z)\vec{E}(t)$ where $\vec{A}(x, y, z)$ is an arbitrary field and $\vec{E}(t) = \exp[i\omega t]$. Substituting this $\vec{E}(x, y, z; t)$ into Eq. 1.5, we are left with the scalar wave equation (also known as the Helmholtz equation),

$$(\nabla^2 + k^2)\vec{A}(x, y, z) = 0. \tag{1.6}$$

Let us assume a time independent electric field of the general form,

$$\vec{A}(x, y, z) = \vec{u}(x, y, z)\exp(-ikz), \tag{1.7}$$

where $\vec{u}(x, y, z)$ describes the wavefront of the beam and $\exp[-ikz]$ describes the travel of the $\vec{E}$-field in the z-direction. If Eq. 1.7 is substituted into the Helmholtz equations we see,

$$\Big(\frac{\partial^2 u}{\partial x^2} + \frac{\partial^2 u}{\partial y^2}\Big) + \frac{\partial^2 u}{\partial z^2} - 2ik\frac{\partial u}{\partial z} = 0 \tag{1.8}$$

We can assume that a wave will vary little along the direction of propagation in relation to the variation in the transverse plane, i.e.

$$\Big|\frac{\partial^2 u}{\partial z^2}\Big| << \Big|\frac{\partial u}{\partial z}\Big|, \Big|\frac{\partial^2 u}{\partial z^2}\Big| << \Big|\frac{\partial^2 u}{\partial x^2}\Big|, \Big|\frac{\partial^2 u}{\partial z^2}\Big| << \Big|\frac{\partial^2 u}{\partial y^2}\Big|. \tag{1.9}$$

This is know as the paraxial wave approximation and reduces Eq. 1.8 to the paraxial wave equation,

$$\nabla_\tau^2 \vec{u} - 2ik\frac{\partial \vec{u}}{\partial z} = 0 \tag{1.10}$$

where ∇_τ^2 is the second partial derivatives in the transverse plane. The form of the solution to this equation depends on the chosen coordinate system. Rectangular coordinates, i.e. (x, y, z), generally gives rise to a Hermite-Gaussian solution; cylindrical coordinates, i.e. (r, ϕ, z), gives a Laguerre-Gaussian solution; and elliptical coordinates, i.e. (η, ζ, z), gives an Ince-Gaussian solution to name a few. In fact, as we will see in Chapter 7, the solution to the paraxial wave equation in rectangular coordinates can even have a solution involving the Airy equation. The following sections describe the solutions to the paraxial wave equation in rectangular and cylindrical coordinate systems.

1.2.2 Solutions to the paraxial wave equation

The simplest solution to the paraxial approximation of the wave equation in rectangular and cylindrical coordinates are of the form,

$$\vec{u}(x, y, z) = \vec{\epsilon} u_0 \exp\Big(-ik\frac{x^2 + y^2}{2R(z)^2} - i\psi(z)\Big)\Big(\frac{-(x^2 + y^2)}{w(z)^2}\Big) \tag{1.11}$$

and

$$\vec{u}(r, \phi, z) = \vec{\epsilon} u_0 \exp\Big(-ik\frac{r^2}{2R(z)^2} - i\psi(z)\Big) \exp\Big(\frac{-r^2}{w(z)^2}\Big), \tag{1.12}$$

defined as the fundamental transverse electromagnetic, or TEM_{00}, wave. In both Eq.'s 1.11 and 1.12, $\vec{\epsilon}$ is the polarization of the field, the function $w(z)$ describes the waist of the Gaussian,

$$w(z) = w_0\sqrt{(z_r^2 + z^2)/z_r^2}, \tag{1.13}$$

where $z_r = \pi w_o^2/\lambda$ is the Rayliegh length and w_0 is the beam waist at $z = 0$. $R(z)$ descibes the curvature of the wavefront at any position along the z-axis,

$$R(z) = z - z_0, \tag{1.14}$$

and $\psi(z)$ in the Gouy phase acquired near the beam waist and is of the form,

$$\psi(z) = atan(z/z_r). \tag{1.15}$$

The Gouy phase is a $\pi/2$ phase shift that is acquired after light passes through a focal point. $\psi(z)$ increases from zero to $\pi/4$ for $z < z_r$, is $\pi/4$ for $z = z_r$ and increases from $\pi/4$ to $\pi/2$ for $z > z_r$. The spatial field distributions for the TEM_{00} beam is shown in Fig. (1.1) in two- and three-dimensions.

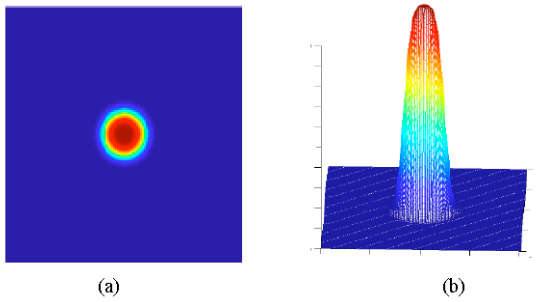

Figure 1.1: The spatial field amplitude distribution for a TEM_{00}wave in (a) 2- and (b) 3-dimensions.

The following are the derivations of higher order modes.

Hermite-Gaussian Modes

To solve the paraxial wave equation in **rectangular coordinates**, i.e. (x, y, z), we can use separation of variables and write the electric field amplitude as the product of two functions,

$$u(x, y, z) = u_n(x, z) \times u_m(y, z), \tag{1.16}$$

where n and m are indices, and solve the paraxial equation for u_n and u_m independently.[11] Let's assume the following is a solution to u_n,

$$u_n(x, z) = C_n \times h_n(x) \times \exp\Big(\frac{-kx^2}{2w(z)}\Big), \tag{1.17}$$

where C_n is a constant and h_n is a function yet to be determined and $w(z)$ is defined as above. Inserting u_n into Eq. 1.10 we obtain the following limitation for $h_n(x)$,

$$h_n^{''}(x) - \frac{2kx}{w(z)} h_n^{'}(x) + \frac{k^2x^2}{w(z)^2} h_n(x) = 0 \tag{1.18}$$

which is similar to form of the Hermite differential equation ,

$$H_n^{''} - 2(x/v)H_n^{'} + 2nH_n = 0. \tag{1.19}$$

Therefore h_n from Eq. 1.18 is in fact the Hermite polynomial, $H_n(\frac{\sqrt{2}x}{w(z)})$. The same method is used to obtain the form of $u_m(y,z)$ which is the same as $u_n(x,z)$ with the dependent variable of the Hermite polynomial being y instead of x.

The final normalized form of the electric field amplitude in rectangular coordinates becomes,

$$u_{m,n}(x,y,z) = C_{n,m}H_n\Big(\frac{x\sqrt{2}}{w(z)}\Big)H_m\Big(\frac{y\sqrt{2}}{w(z)}\Big)\exp\Big(-\frac{(x^2+y^2)}{w(z)^2}\Big)\exp\Big(\frac{-ik(x^2+y^2)}{2R(z)} - i\psi(z)\Big) \tag{1.20}$$

where $C_{n,m}$ are normalization constants for the x- and y-directions, z_r is the Rayleigh range and $R(z)$ and $w(z)$ are defined above. As before,

$$\psi(z) = (n+m+1)arctan(z/z_r), \tag{1.21}$$

is the Gouy phase adding a phase from 0 to $2\pi(n+m+1)$ across the focus of the beam.

The field distribution of these higher order Hermite-Gaussian modes have nodes in the x- and y- directions corresponding to the value of n and m, respectively. The order of the Hermite-Gaussian (HG) mode is given by,

$$N = n + m \tag{1.22}$$

where n and m are both positive integers.

The intensity distributions, $|u_{n,m}|^2$, for several values of $HG_{n,m}$ modes are shown in Fig (1.2). The polarization of these higher order modes are no different to the zero-order mode, except that the phase of the light changes by π across any node line. Across any node, however, there is a π-phase shift in the wave. The TEM_{00} mode is identical to the $HG_{0,0}$ mode. Hermite-Gaussian modes will be critical later in one method to generate beams optical vortices with orbital angular momentum.

Laguerre-Gaussian Modes

In cylindrical coordinates, the solution to the paraxial wave equation will contain Laguerre Polynomials. As we will see, Laguerre-Gaussian (LG) modes can be thought to be made up by a superposition of Hermite-Gaussian modes and has orbital angular momentum associated with the wave amplitude. To see this we must look at where these LG modes come from.

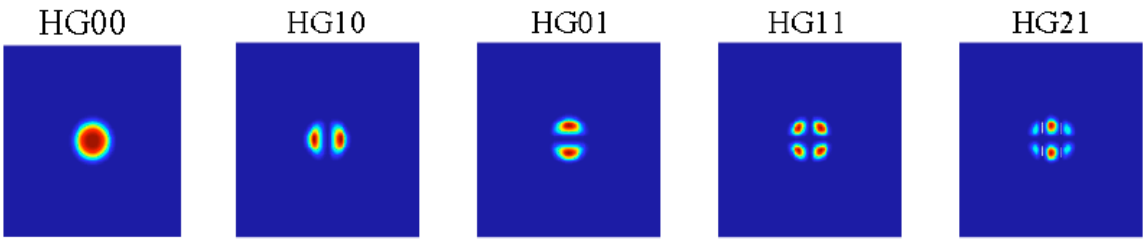

Figure 1.2: Various Hermite-Gaussian modes.

In **cylindrical coordinates**, i.e. (r, ϕ, z), we can re-write the electric field amplitude as,

$$u(r, \phi, z) = u_{p,l}(r, \phi, z), \tag{1.23}$$

where l and p are indices for the azimuthal and radial coordinates, respectively. Solving the paraxial equation for $u_{p,\ell}$ in a similar fashion as we did in the rectangular coordinate case above and the solution can be expanded in Laguerre modes and takes the form,[76]

$$u_{p,\ell} = C_{p,l} \times \Big(\frac{r\sqrt{2}}{w(z)}\Big)^{|l|} \times L_p^l\Big(\frac{2r^2}{w(z)^2}\Big) \times \exp\Big(\frac{-ikr^2}{2R(z)} - i\psi(z)\Big) \exp\Big(-il\phi\Big), \tag{1.24}$$

where $C_{p,l}$ is the normalization constant, $L_p^l(\frac{2r^2}{w(z)^2})$ is a generalized Laguerre polynomial, l is the azimuthal mode (also known as the winding number or charge), p is the radial mode, and

$$\psi(z) = (2p + |l| + 1)arctan(z/z_r) \tag{1.25}$$

is again the Gouy phase adding a phase from 0 to $2\pi(2p + l + 1)$ across the focus of the beam. The order of the Laguerre-Gaussian mode is given by,

$$N = 2p + |l| \tag{1.26}$$

where p is any positive integer and l is any integer, positive or negative. The intensity distributions, $|u_{p,l}|^2$, for several LG_p^l modes are shown in Fig (1.3). Notice the TEM_{00} modes is the equivalent of the LG_0^0.

The salient difference between the the solution to the paraxial equation in rectangular coordinates as in Eq. 1.20 and the solution in cylindrical coordinates as in Eq. 4.1 is the extra phase factor of $\exp(il\phi)$ which adds a variation to the phase of the wavefront and the $r^{|}l|$ term which is responsible for the size of the vortex as seen

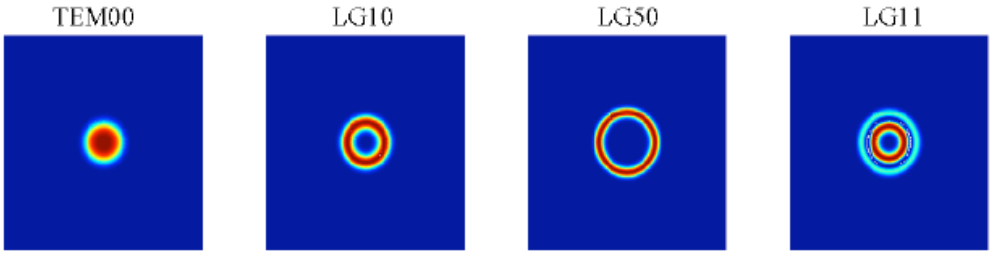

Figure 1.3: Various Laguerre-Gaussian modes

in Fig. 1.3. As we will see, both of these features in Eq. 4.1 contribute to the orbital angular momentum.

1.2.3 A description of optical vortices

The intensity and phase structure of such a Laguerre-Gaussian (LG) beams is shown in Fig. 1.4. The field distribution in the x-y plane described by Eq. 4.1 for (a) $l = 1$, (b) $l = 2$, (c) $l = 3$, and (d) $l = 5$ is shown. Clearly $l = 0$ would give the pure Gaussian wave described earlier in Eq. 1.11. A beam with $l = 1$ resembles a doughnut with a singularity or vortex at the beams center and the phase changes azimuthally from 0 to 2π once. If $l = 2$ the phase changes azimuthally from 0 to 2π twice, and so on. Fig. 1.5 shows the helical, twisting nature of the LG beam. In this figure the points that have the same phase form the helical surface where the number l corresponds to the number of twists in the helix ($l = 1$ is shown). The points, in the figure, show points of equal phase on each wave and the helical surface is the surface that connects all of these points. The plane shown is a plane of constant phase.

The Laguerre-Gaussian beam is an example of a larger class of beams known as optical vortices, that have phase or polarization singularities. Such beams can be twisted like a corkscrew about the axis of travel and have zero intensity at their center. The vortex has a number associated with it known as the optical charge that represents the number of times the waves twist in one wavelength. The higher this number the faster the light spins around its axis.

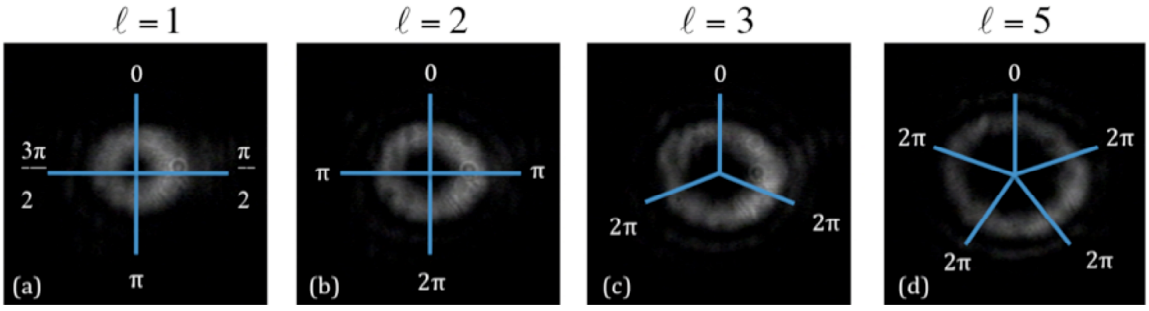

Figure 1.4: Intensity of Laguerre-Gaussian beams with (a) $l = 1$, (a) $l = 2$, (c) $l = 3$, and (d) $l = 5$. The phase of the field around the beam is shown.

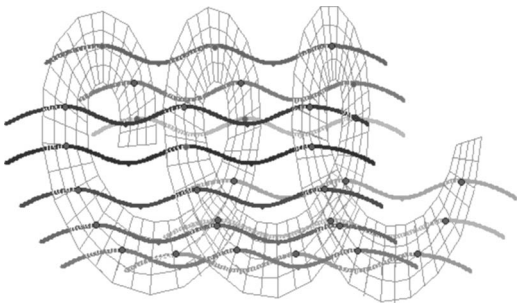

Figure 1.5: Perspective view of a Laguerre-Gaussian beam with $l = 1$. The helical surface is formed by points where the wave has the same phase (reproduced with permission from E. Galvez, Am. Jour. Phys., 74 335 (2006).)

1.3 Angular momentum of light

1.3.1 Spin angular momentum

Spin angular momentum (SAM) of light is intrinsic and comes purely from the vectorial nature of light, i.e. **polarization**. The amount of SAM associated with a beam of light will be derived and shown to come from circularly polarized waves and reducible to the amount of spin per photon.

First, it is convenient to derive the exact amount of SAM associated with a circularly polarized plane wave. Once this is complete it is nice to see what the calculation looks like for an arbitrary polarization state.

It is well known that electromagnetic fields have an associated energy flow, the

Poynting vector, given by,[84, 13]

$$\vec{S} = \epsilon_0 \vec{E} \times \vec{B}, \tag{1.27}$$

a linear momentum density, $\vec{p} \propto \vec{S}$, and an angular momentum density, $\vec{j} = \vec{r} \times \vec{p}$. Assuming a vector potential of the form,

$$\vec{A} = \hat{n} u(x, y, z) \exp(ikz) \tag{1.28}$$

where $\hat{n}$ is the complex direction of polarization (allowing for circular polarization), then the electric and magnetic fields are found in the Lorenz gauge as

$$\vec{B}(x, y, z) = ik\Big[\hat{z} \times \hat{n} u + (i/k)\hat{n} \times \nabla_\tau u\Big] \tag{1.29}$$

$$\vec{E}(x, y, z) = i\omega\Big[\hat{n} u + \hat{z}(i/k)\hat{n} \cdot \nabla_\tau u\Big] \tag{1.30}$$

where ∇_τ is the derivative in the transverse plane. So if the polarization, $\hat{n}$, is $\hat{n} = \hat{x} \pm i\hat{y}$ and $u(x, y, z) = \exp[-(x^2 + y^2)]$, i.e. we are working with a circularly polarized plane wave, then the following are the associated fields for such a circularly polarized, Gaussian vector potential:

$$\vec{B}(x, y, z) = ik\Big[(\hat{y} + i\hat{x}) + (2i/k)(-y + ix)\hat{z}\Big]u \tag{1.31}$$

$$\vec{E}(x, y, z) = i\omega\Big[(\hat{x} + i\hat{y}) - (2i/k)(x + iy)\hat{z}\Big]u \tag{1.32}$$

With these fields the linear and angular momentum densities are:

$$\vec{p} = \epsilon_0 \vec{E} \times \vec{B} = -2\epsilon_0 \omega k u^2 \hat{z} \tag{1.33}$$

$$\vec{j} = \vec{r} \times \vec{p} = 2\epsilon_0 \omega k r u^2 \hat{\phi} \tag{1.34}$$

where $\vec{r} \times \hat{z} = r\hat{\phi}$. A similar derivation can be carried out for a polarization of opposite helicity, i.e. $\hat{n} = \hat{x} - i\hat{y}$, leading to an angular momentum with opposite sign. These result shows that the angular momentum is proportional to the energy, u^2, and the initial polarization. To verify that this angular momentum is only present when we start with a circularly polarized vector potential, it is now beneficial to generalize the polarization state. If we had started with with some linear polarization state, $\hat{n} = \hat{x} + \hat{y}$ say, then the angular momentum in the $\hat{\phi}$-direction would indeed be zero.

Approaching this problem a bit more rigorously to generalize these calculations, let's now assume a polarization, $\hat{n} = \alpha\hat{x} + \beta\hat{y}$, where α and β can be complex. The

fields are now,

$$\vec{B} = \Big[(\frac{\partial u}{\partial z} + iku)(-\beta\hat{x} + \alpha\hat{y}) + (\beta\frac{\partial u}{\partial x} - \alpha\frac{\partial u}{\partial y})\hat{z}\Big]\exp(ikz) \tag{1.35}$$

$$\vec{E} = i\omega\Big[\alpha u\hat{x} + \beta u\hat{y} - (i/k)(\alpha\frac{\partial u}{\partial x} + \beta\frac{\partial u}{\partial y})\Big]\exp(ikz) \tag{1.36}$$

Taking the time-averaged cross product of $\vec{E} \times \vec{B}$ it is found that,

$$\vec{p} = \frac{\epsilon_0}{2}\Big[(\vec{E}^* \times \vec{B}) + (\vec{E} \times \vec{B}^*)\Big] \tag{1.37}$$

and using Eq.'s 1.35 and 1.36 we see,

$$\vec{p} = \frac{i\omega\epsilon_0}{2}\Big[(u\nabla u^* - u^*\nabla u) - 2ik\epsilon_0|u|^2\hat{z} + (\alpha\beta^* - \alpha^*\beta)(\nabla|u|^2 \times \hat{z})\Big]. \tag{1.38}$$

The first term is part of the angular momentum in the $\hat{\phi}$-direction which is zero for this form of the field amplitude. The term $(\alpha\beta^* - \alpha^*\beta)$ is the general polarization term we are interested in and is identified with the spin in the z-direction, σ, as it is in the $\hat{\phi}$-direction here and when crossed with $\hat{r}$ gives $\hat{z}$. If $\alpha = 1$ and $\beta = \pm i$, i.e. circularly polarization, then $(\alpha\beta^* - \alpha^*\beta) = \pm 2i$. If $\alpha = 1$ and $\beta = 1$, which is a linearly polarized beam has $(\alpha\beta^* - \alpha^*\beta) = 0$, i.e. there is no angular momentum. Therefore, σ can take the value of ± 1 which corresponds to the helicity of the circular polarization.

Noting that in cylindrical coordinates $|u|^2$ is ϕ-independent,

$$\nabla|u|^2 \times \hat{z} = -\hat{z} \times \frac{\partial|u|^2}{\partial r}\hat{r} = \frac{\partial|u|^2}{\partial r}\hat{\phi}$$

and looking now only at the z-component of the angular momentum density,

$$j_z = [\vec{r} \times (\epsilon_0\vec{E} \times \vec{B})]_z = r\epsilon_0(\vec{E} \times \vec{B})_\phi = \frac{\epsilon_0}{2}\omega r\sigma\frac{\partial|u|^2}{\partial r}. \tag{1.39}$$

This shows that the angular momentum is directly proportional to the handedness of the polarization. Finally, integrating across the beam we can find the ratio of total angular momentum to the energy per unit length,

$$\frac{J_z}{W} = \frac{\int\int r dr d\phi(\vec{r} \times (\vec{E} \times \vec{B})_z}{c\int\int r dr d\phi(\vec{E} \times \vec{B})} = \frac{\sigma}{\omega}. \tag{1.40}$$

In a semi-classical approximation, $W = N\hbar\omega$, where N is the total number of photons. Therefore the angular momentum per photon associated with a circularly polarized electromagnetic wave is then,

$$\frac{J_z}{N} = \sigma\hbar, \tag{1.41}$$

where again $\sigma = (\alpha\beta^* - \alpha^*\beta) \propto \{\pm 1, 0\}$ is the total spin angular momentum, depending on the polarization state, $\hat{n} = \alpha\hat{x} + \beta\hat{y}$ with α and β being allowed to be complex. Therefore, the angular momentum due to the polarization of light is either $+\hbar$ or $-\hbar$ for left and right handed circular polarization, respectively.

Why Call it Spin?

Saying that light, or photon's, have a quantum mechanical spin may seem a bit presumptuous. Why call it spin? Is the spin we are talking about the spin we deal with in quantum mechanics? M.V. Berry [14] gives a nice mathematical overview of the angular momentum of light and begins to answer these questions. If we consider the wave function of a photon in the basis of circular polarization we would have,

$$|\psi\rangle = \frac{1}{\sqrt{2}} \begin{pmatrix} \psi_R \\ \psi_L \end{pmatrix} = \begin{pmatrix} E_x - \imath E_y \\ E_x + \imath E_y \end{pmatrix}, \tag{1.42}$$

where $|\psi\rangle$ is normalized and our left- or right-circular polarization state is either $\begin{pmatrix} 1 \\ 0 \end{pmatrix}$ or $\begin{pmatrix} 0 \\ 1 \end{pmatrix}$. If we choose to measure the expectation value of the spin in the z-direction using this state then we would have,

$$S_z = \langle\psi|s_z|\psi\rangle, \tag{1.43}$$

where $s_z = \hbar\sigma_z$ and σ_z is the z- component of the Pauli matrix. So calculating Eq. 1.43,

$$S_z = \hbar\langle\psi| \begin{pmatrix} 1 & 0 \\ 0 & -1 \end{pmatrix} |\psi\rangle = \hbar\Big(|\psi_+|^2 - |\psi_-|^2\Big). \tag{1.44}$$

So if we start with an initial polarization of ψ_+, or right circular polarization, then $S_z = +\hbar$ and if we start with ψ_-, or left circular polarization, then $S_z = -\hbar$. Since these are the exact values of the spin per photon in Eq. 1.41 this angular momentum can indeed be called what we refer to in quantum mechanics as spin.

1.3.2 Orbital angular momentum

The amount of orbital angular momentum (OAM) associated with a given *wavefront* profile of a light beam will be discussed and shown to be reducible to the amount of OAM per photon. Orbital angular momentum is shown here to come from the

azimuthally varying phase of the wavefront. Experiments involving the use of beams of light with OAM and ways of measuring the amount of angular momentum per photon will be discussed.

In the derivation of spin angular momentum of light we used the vector potential $\vec{A} = (\alpha\hat{x} + \beta\hat{y})u(x, y, z)\exp(ikz)$, where the form of $u(x, y, z)$ was that of a Gaussian in rectangular coordinates, i.e. $\exp[-(x^2 + y^2)]$, to derive the amount of angular momentum. Suppose instead that $u(x, y, z)$ is of a Laguerre-Gaussian nature with $p = 0$, i.e. LG_0^l,

$$u(r, \phi, z) = \exp(-r^2)\exp(il\phi), \tag{1.45}$$

where l can be any integer and is also known as the charge or winding number of the Laguerre-Gaussian mode.

Using Eq. (1.35 - 1.38) we can derive a value of the total angular momentum for a Laguerre-Gaussian mode. The ϕ- and z-components of the linear momentum density of a Laguerre-Gaussian vector potential are,

$$p_\phi = \frac{\omega\epsilon_0 l}{r}|u|^2 + 2i\omega\epsilon_0\sigma|u|^2 \tag{1.46}$$

$$p_z = ck^2\epsilon_0|u|^2. \tag{1.47}$$

Again using $\vec{j} = \vec{r} \times \vec{p}$, leads to an angular momentum density about the z-axis,

$$j_z = \epsilon_0\omega l|u|^2 + 2i\epsilon_0\omega\sigma r|u|^2. \tag{1.48}$$

Integrating across the beam we can find the ratio of total angular momentum to the energy per unit length,

$$\frac{J_z}{W} = \frac{\int\int rdrd\phi(\vec{r} \times (\vec{E} \times \vec{B})_z}{c\int\int rdrd\phi(\vec{E} \times \vec{B})} = \frac{\sigma + l}{\omega}. \tag{1.49}$$

And since $W = N\hbar\omega$, the total angular momentum per photon is

$$\frac{J_z}{N} = (\sigma + l)\hbar \tag{1.50}$$

where σ is the spin angular momentum and l is the orbital angular momentum. So a LG_0^lbeam indeed has *orbital angular momentum*. With an angular momentum of this form we are not limited to just $J_z/N = \pm\hbar$. Instead, with the addition of the orbital term, l, we can have any integer value of total angular momentum as $l = \{0, \pm1, \pm2, \pm3, \ldots\}$. This equations shows that the total angular momentum is

dependent on the polarization state, however the orbital angular momentum is only dependent on the value of l.

Earlier we saw that the spin angular momentum came from the polarization nature of the light, i.e. circularly polarized light had $j_z = \pm l\hbar$. Now we are seeing a total angular momentum that is dependent not only on the polarization, but the phase structure of the beam profile as well. The extra term in the electric field, $\exp[il\phi]$, corresponds to a different phase at each azimuthal angle of the beam giving rise to this orbital angular momentum.

Fig. 1.6(a) shows a LG_0^1 beam and the wavefronts relative phase at different angles around the beam. The top, $\phi = 0$, has a phase of zero; $\phi = 90^0$ has a phase of $\pi/2$; $\phi = 180^0$ has a phase of π; $\phi = 270^0$ has a phase of $3\pi/2$; and $\phi = 360^0$ has a phase of 0 again. So the phase goes through a 2π cycle once every time around the beam when $l = 1$.

A beam with $l = 2$ has a phase that goes from 0 to 2π twice as you go around the beam once, and so on, as shown in Fig. 1.4. When $l = 0$, we have a fundamental mode, and the phase would be constant everywhere on the wavefront so it is a plane wave.

This apparently leads to the notion that we are dealing with helical wavefronts now rather than just plane waves. An analogy is that if you were looking at the electric field structure of a LG beam it would look like a corkscrew traveling in the direction of propagation, shown in Fig. 1.6(b). In this figure, we are observing a plane of constant phase traveling in the z-direction. This is actually an $l = 2$ wavefront as there are two angles of the same phase at any z-location. It is this changing phase along the azimuthal direction that results in the orbital angular momentum.

1.4 Generating beams of light with orbital angular momentum

There are several methods to generate Laguerre-Gaussian beams of light that carry OAM. They can be generated directly form a laser cavity given the right conditions [16], by an astigmatic mode converter that converts HG modes to LG modes [17, 15], or by spiral phase plates [18, 19]. A fairly simple method to generate a LG_p^l from a Gaussian, TEM_{00}, beam is to use a diffraction grating with a phase singularity

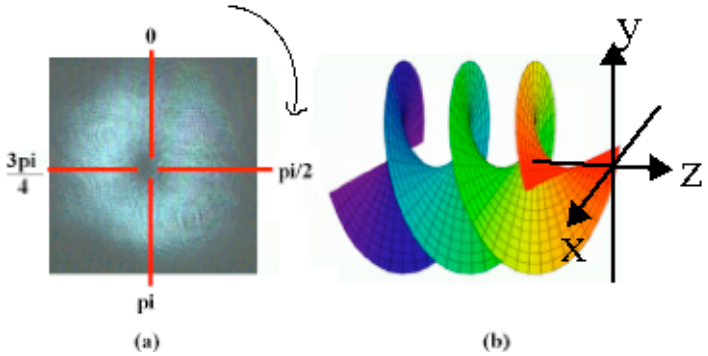

Figure 1.6: (a) An image of a LG_0^1 beam and its associated phase structure and (b) the wavefronts helical nature of the LG beam.[15]

[40, 20, 21]. One way of thinking of a diffraction grating is as the interference pattern that you would get from two beams, in this case a TEM_{00} and LG_0^1 beam. If the beam passing through this diffraction grating is a TEM_{00} beam then your diffraction has a zero-order mode of the incident beam, first-order modes of $l = \pm 1$, second-order modes of $l = \pm 2$, etc.

1.4.1 Forked diffraction gratings

The form of the diffraction grating is calculated from the interference between the TEM_{00} and the LG_0^l beams. If the TEM_{00} mode is taken as $\vec{E}_1$ and the LG_0^l mode is $\vec{E}_2$, then the intensity of the two fields added is,

$$\begin{aligned} I &= \vec{I_1}^* \vec{I_2} && (1.51)\\ &= (\vec{E_1}^* + \vec{E_2}^*)(\vec{E_1} + \vec{E_2}) && (1.52)\\ &= |\vec{E_1}|^2 + |\vec{E_2}|^2 + (\vec{E_1}^* \vec{E_2} + \vec{E_1}\vec{E_2}^*) && (1.53) \end{aligned}$$

where the last term above is the interference term of interest. Taking

$$\vec{E_1} = \vec{E}_{00} \exp[i(\omega t + \delta)] \qquad \vec{E_2} = \vec{E}_{0l} \exp[i(\omega t + \theta)] \tag{1.54}$$

where $\delta = \delta(x, y)$ and $\theta = \theta(x, y)$, $\vec{E}_{00}$ is the field associated with the TEM_{00} mode and $\vec{E}_{01}$ is the field associated with the LG_0^l mode. For the LG_0^l mode, $\theta(x, y) = l\phi$, and for the TEM_{00} mode, $\delta(x, y) = kx$ where $k = 2\pi/\lambda$ determines the fringe spacing

of the grating. The interference comes from the difference between phases between the two electric fields,

$$\theta - \delta = l\phi - kx$$

or,

$$\frac{\theta - \delta}{2} = l\phi - \pi x/\lambda \tag{1.55}$$

The condition for a binary grating is that $(\theta - \delta)/2 = n\pi$, so the expression for our diffraction pattern is,

$$n\pi = \frac{l \tan^{-1}(y/x)}{2} - \frac{\pi x}{\lambda}. \tag{1.56}$$

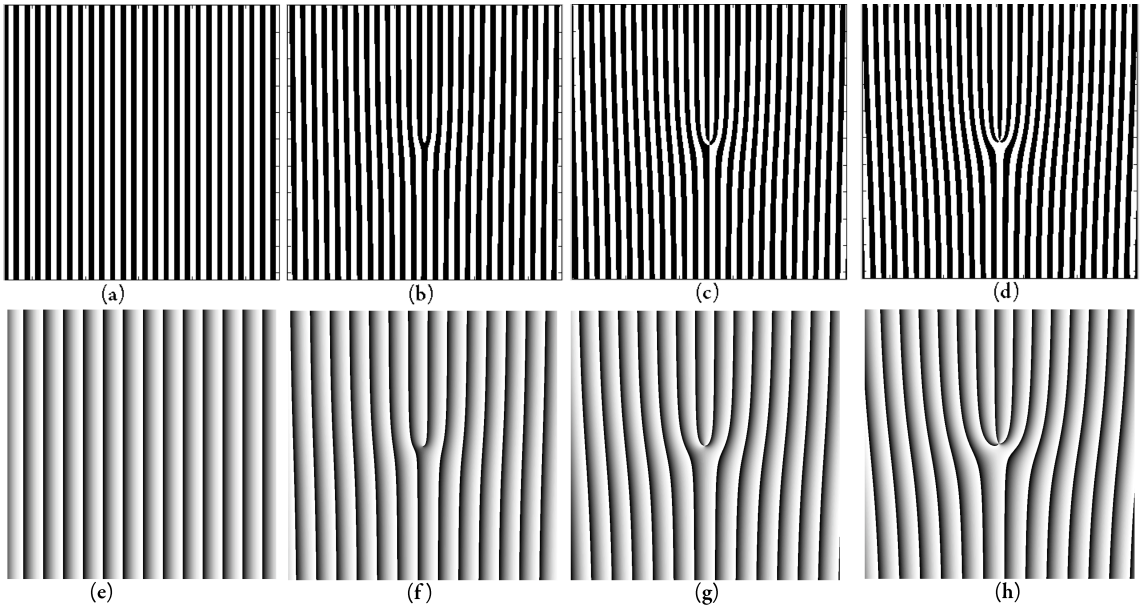

Figure 1.7: Binary diffraction gratings generated from Eq. (1.56) for (a) $l = 0$, (b) $l = 1$, (c) $l = 2$, (d) $l = 3$. (e-h) The equivalent blazed diffraction gratings.

The computer generated holograms (CGH) for (a) $l = 0$, (b) $l = 1$, (c) $l = 2$, (d) $l = 3$ are shown in Fig. (1.7). The $MATLAB$ code used to generate this grating is given in Appendix A. To generate a LG_0^l beam, a TEM_{00} beam is passed through a reduced image of Fig. (1.7) on high quality film or a spatial light modulator (SLM) which is discussed in more detail below.

Figure 1.8 shows how a zero-order Gaussian beam is passed through a forked diffraction grating, with $l = 1$, to generate higher-order LG modes. The negative

aspect of this type mode conversion is the decreasing intensity of higher order modes due to the diffraction. Conversion efficiency of the first-order mode is on the order of 15%, falling off rapidly in the even higher order modes. This relatively low efficiency can be increased by using a blazed diffraction grating.

A blazed forked diffraction grating is used to direct more energy into the first order diffracted beam. To obtain the "blaze" in the computer generated hologram the grating equation in eq. (1.56) is modified to introduce a phase change from 0 to 2π along each dark (or bright) fringe. If the expression for the binary grating is

$$H(x,y) = \frac{l\tan^{-1}(y/x)}{2} - \frac{\pi x}{\lambda} \tag{1.57}$$

then the expression for the blazed grating becomes,

$$T(x,y) = \exp\Big[-imod(H(x,y),2\pi)\Big] \tag{1.58}$$

where $mod()$ is the modulo function. Figure 1.7 (e-h) show the blazed gratings for $l = 0, 1, 2, 3$, respectively. The blaze on the these gratings comes from a variation in the grayscale from white to black rather then a physical path length difference on a traditional blazed grating.

1.4.2 Using a spatial light modulator

In this thesis a reflective type spatial light modulator (SLM) is used to generate LG laser beams. A SLM is a re-programable liquid crystal micro-display that can modulate the phase and amplitude of light waves. Information is passed via a DVI output of a PC to the SLM that displays the information. The *HoloEye Corp. LC-720* high speed spatial light modulator was used in this work.

A custom *MATLAB* graphical user interface (GUI), *GratingUI*, was designed by me, to allow easy manipulation of the several key factors involved in generating these gratings, including: the grating type, i.e. binary or blazed, the grating period, the blaze angle, the l-value, the resolution of the grating on the screen, and the orientation of the grating, i.e. vertical or horizontal. The *GratingUI* uses Eqs. (1.56) and (1.58) to generate the binary and blazed gratings, respectively, and is shown in Fig. 1.9. The software code is given in Appendix A. The CGH in the *GratingUI* window is maximized on the computer screen (which is also the image sent to the SLM display), so that it fills the entire SLM. Using this method approximately 45% of the light

incident on the SLM is converted to the LG_0^l beam, where the l is given by the charge of the forked grating. The benefit of using the *GratingUI* program to display gratings on the SLM is that it is a fast, reprogrammable interface that allows the grating period, l-value, etc. to be easily manipulated in a multitude of experimental situations.

When the "Generate Grating " button is clicked in the software, shown in Figure 1.9, the grating with the selected parameters appears in the central region of the figure. Figure 1.10 shows the typical experimental arraignment to create a LG beam using the SLM and *GratingUI* program.

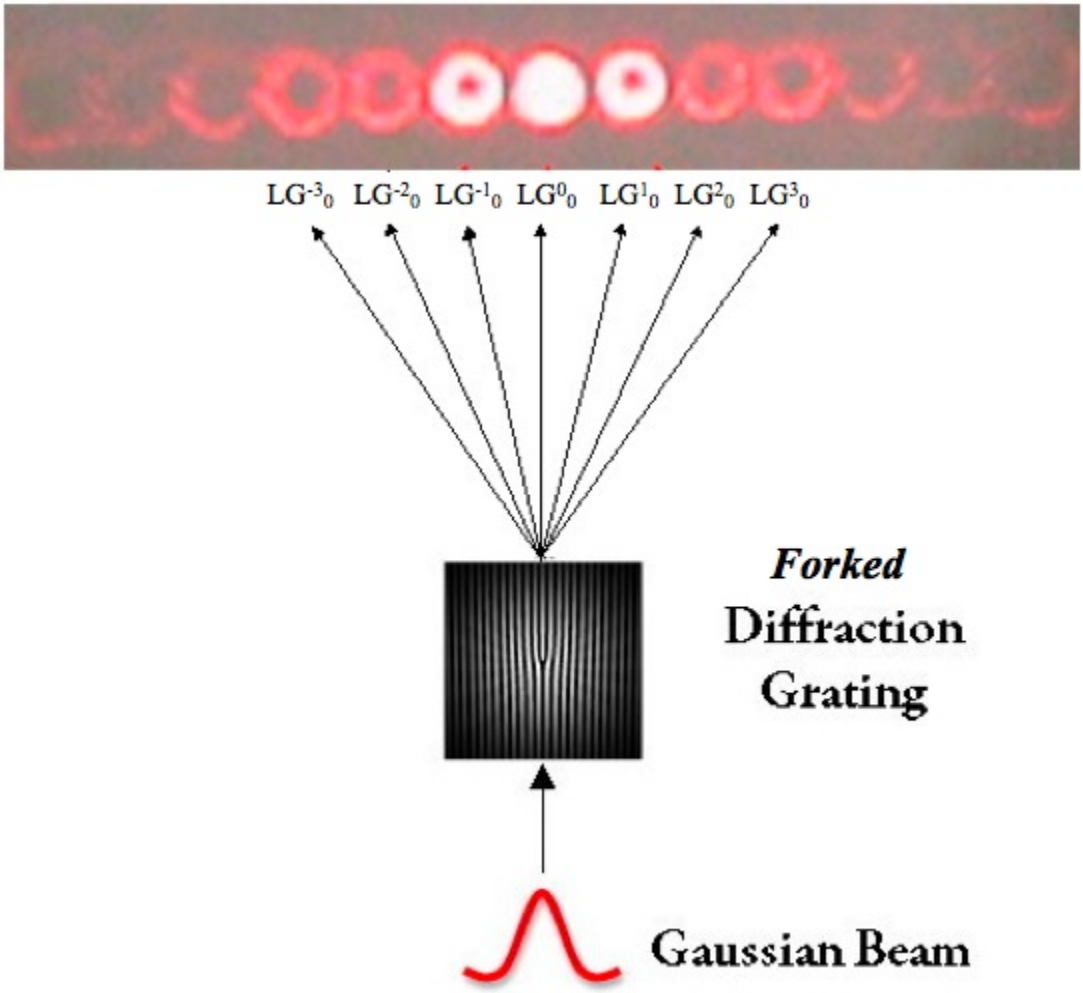

Figure 1.8: Diffraction pattern when passing a TEM_{00} beam through Fig. (1.7). The center beam is the TEM_{00} mode and each next beam moving outward is mode $l = \pm 1, \pm 2, \ldots$

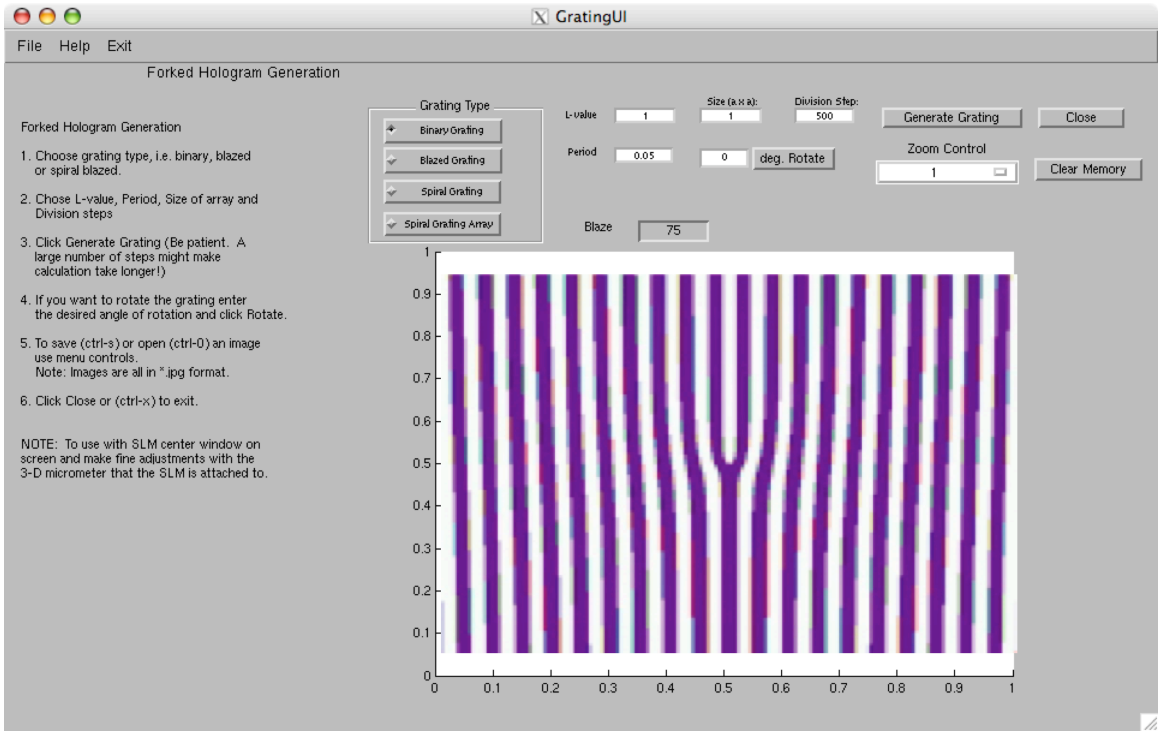

Figure 1.9: The *GratingUI* program used to generate binary and blazed diffraction gratings is shown.

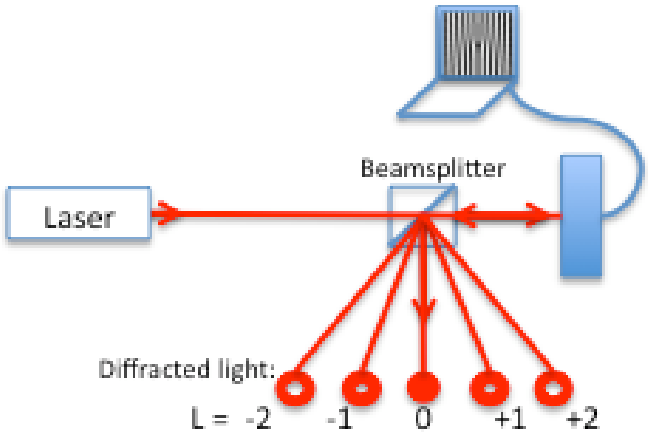

Figure 1.10: Setup to use the SLM. The light that is diffracted form the SLM is shown below assuming an $l = 1$ grating (shown in the computer display).

Chapter 2

Diffraction of Laguerre-Gaussian Beams

2.1 Introduction

One of the salient features of light is coherence which is revealed by interference in the form of fringes. This interference is a key aspect of the wave-nature of light. Young's double slit experiment[22] shows interference phenomena and has resulted in a multitude of experiments showing the wave nature of light, electrons,[23, 24] neutrons[25], and most recently atoms[26]. It is our understanding that optical beams that posses orbital angular momentum have not been used in Young's double slit experiment. It is well known that beams of light can carry both spin- and orbital-angular momentum.[40, 43] The spin angular momentum has been shown to arise from the vectorial, or polarization nature of light while the orbital angular momentum has been shown to arise form the spatial distribution of an electromagnetic wave-front[29]. Laguerre-Gaussian (LG) beams of light carry a well defined amount of orbital angular momentum proportional to the variation of the phase structure of the beam. This orbital angular momentum is *in addition to* the spin angular momentum associated with the polarization state of the light.

This chapter demonstrates a double slit interference experiment using optical LG beams [30]. This new slant on double-slit interference leads to a better understanding and interpretation of the nature of the optical orbital angular momentum (OAM) in interference phenomena.

2.2 Double slit diffraction

A Laguerre-Gaussian beam has a complex field amplitude proportional to

$$u(r,\phi,z)_{p,l} \propto r^l L_p^l\Big(\frac{2r^2}{w^2}\Big)\exp\Big(-\frac{r^2}{w^2}\Big)\exp\Big(-il\phi\Big), \tag{2.1}$$

where w is the waist size of the beam, $L_p^l(\frac{2r^2}{w^2})$ is the associated Laguerre polynomial, l is the azimuthal mode, and p is the radial mode. The amount of orbital angular momentum that a LG beam with $p = 0$ bears is $l\hbar$ per photon, where $l = 0, \pm1, \pm2, \ldots$ LG beams posses a phase singularity, also called an optical vortex, due to the azimuthal phase dependence. As a LG beam propagates there is a phase variation around a wave-front which is why people now call these helical waves.[49] The vortex and phase dependence are what will provide an interesting result in these interference experiments.

The experimental setup to investigate the interference of LG beams by slits is shown in Fig. 2.1. A computer generated hologram is used to introduce the azimuthal phase variation that is inherit to a LG beam.[50, 51] A He-Ne laser beam (632.8 nm) is passed through a charge-1 forked diffraction grating shown in Fig. 2.1(a) to produce the LG beams with charge $l = \pm 1, \pm 2 \ldots$

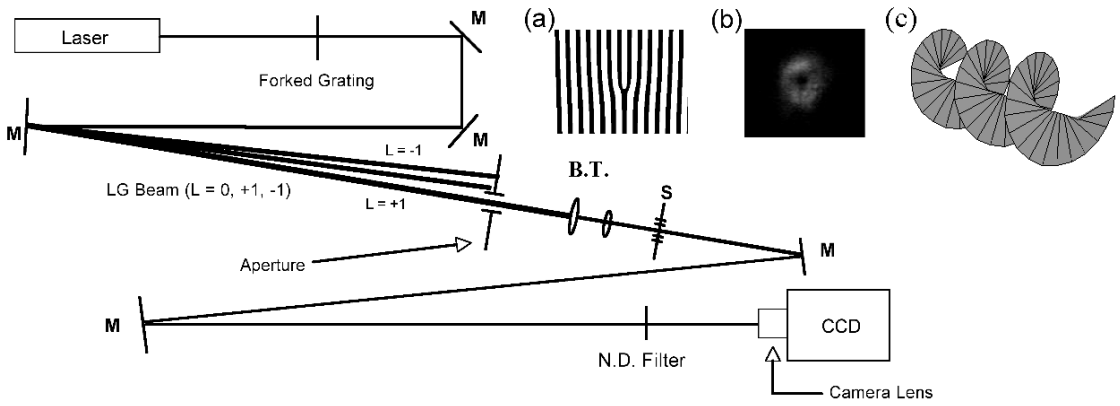

Figure 2.1: Experimental diffraction setup (M- Mirror, S- Slits, B.T.- Beam Telescope, N.D.- Neutral Density Filters). Inset: (a) The forked diffraction grating used to create LG beams of charge $l = 0, \pm 1, \pm 2, \ldots$, (b) LG mode selected with $l = +1$, and (c) Helical wave-front of LG beam.

One mode is selected for each double-slit experiment by placing a circular aperture in front of the beam, allowing only one mode to pass through the slits (S). For the double-slit experiment the singularity is positioned between the two slits. To position the singularity between the two slits a beam telescope (B.T.) is used to de-magnify the LG beam. The two slits have a width of approximately $200\mu m$ with a spacing between slits of approximately $900\mu m$. The LG modes selected are either the $l = +1$ or $l = -1$ mode, one of which is shown in Fig. 2.1 (b). Part (c) of the same figure shows the helical nature of this beam as a plane of constant phase is shown traveling in the direction of propagation.

In a standard double-slit experiment, with plane-waves, the interference pattern on a screen results from the optical phase difference, δ, of the incident light field from each slit to the observation point due to the optical path length difference, Δ. When a plane wave passes through two slits there is no relative phase difference across a

wave-front of the light *at* the two slits. The fringes in the far-field will therefore be spaced equally along the long axis of the slits. Common derivations[34] of the intensity distribution of the interference between two parts of a plane wave-front on a screen gives

$$I(x) \propto cos^2\Big(\frac{\delta}{2}\Big) \tag{2.2}$$

$$\propto cos^2\Big(\frac{\pi a x}{\lambda d}\Big), \tag{2.3}$$

where λ is the wavelength of the incident light, a is the slit width, and d is the distance from the slits to the observation screen. The argument of the cosine, $\pi ax/\lambda d$, is derived from the optical phase difference between the two slits.

In contrast, a double-slit experiment using LG helical wave-fronts will exhibit interference due to the path difference of the incident light from the slits to the observation point *in addition to* the contribution from the twisting phase structure of the wave-front. When a LG beam with $l = \pm 1$ passes through two slits and the singularity falls between the two slits there is a rich relationship between the relative phase on the wave-front at the slits. In fact, the interference will have some correlation to the width of the slits because the wider the slits are the more the phase varies across the slits. This effect can be seen in Fig. 2.2 where the relative phase of the beam-front is shown by shade (black is 0, white is 2π). In (a) of this figure equal lines of shade represent equal lines of phase on the wave-front. Note, for the $l = \pm 1$ wave-front the phase varies by one cycle as the azimuthal angle goes from 0 to 2π. Fig. 2.2 (b) shows what the phase variation across the wave-front is within the two slits. If we call the phase along the left slit $\phi_1(y)$ and the phase along the right slit $\phi_2(y)$ then Fig. 2.2 (c) shows the additional phase difference between the two slits along the vertical direction given by

$$\Delta\phi(y) = \phi_2(y) - \phi_1(y). \tag{2.4}$$

While the optical path length difference between the wavefront at the two slits to the screen remains the same when we use a LG beam incident on the slits, the optical phase does not. There is an additional phase now due to the azimuthal phase variance along the LG wave-front. A term $\Delta\phi$ is added to the interference intensity distribution at the screen so that:

$$I(x,y) \propto cos^2\Big(\frac{\delta}{2} + \frac{\Delta\phi(y)}{2}\Big) \tag{2.5}$$

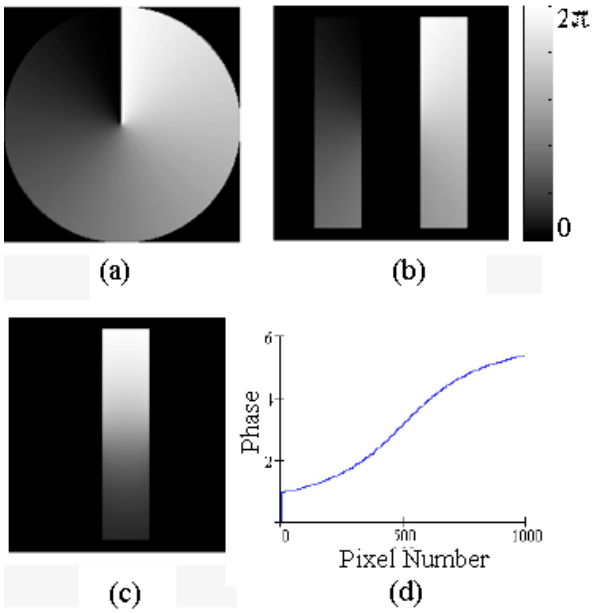

Figure 2.2: (a) The phase structure of a Laguerre-Gaussian wave-front where equal lines of shade represent equal lines of phase (black is 0 and white is 2π) (b) The same wave-front lies on two slits with its singularity in between the slits. (c) The phase difference between the left and right slit. (d) The pixel values along the y-direction at the center of the slit in (c). These values are $\Delta\phi(y)$.

$$\propto \quad cos^2\Big(\frac{\pi a x}{\lambda d} + \frac{\Delta\phi(y)}{2}\Big). \tag{2.6}$$

Eq.'s 2.3 and 2.6 can be seen graphically in Fig. 2.3 (a)-(c), where (c) uses $-\Delta\phi(y) = \phi_1(y) - \phi_2(y)$ modeling a LG incident beam with opposite helicity. The function $\Delta\phi(y)$ is taken numerically from Fig. 2.2 (d).

The relative phase difference between the two slits along the horizontal diameter of the LG beam is π while the phase difference at a point closer to the top or bottom of the slits is some non-integer value of π as shown by the values of phase in Fig. 2.2 (d). The change in the relative phase of the light at the slits should therefore shift the interference fringes in the x-direction as we look from the top of the interference to the bottom. The phase difference between the top and bottom of the slits is close to π which should place constructive interference, or a bright fringe, on top lining up with a dark fringe on the bottom of the interference pattern. This feature is seen in the computer generated plot in Fig. 2.3 (a) and (c). The phase variation in the

y-direction along the slit is what affects the interference pattern. Note, this effect is not manifested by either a dynamic or geometric phase as discussed by E. Galvez *et. al.* [35]

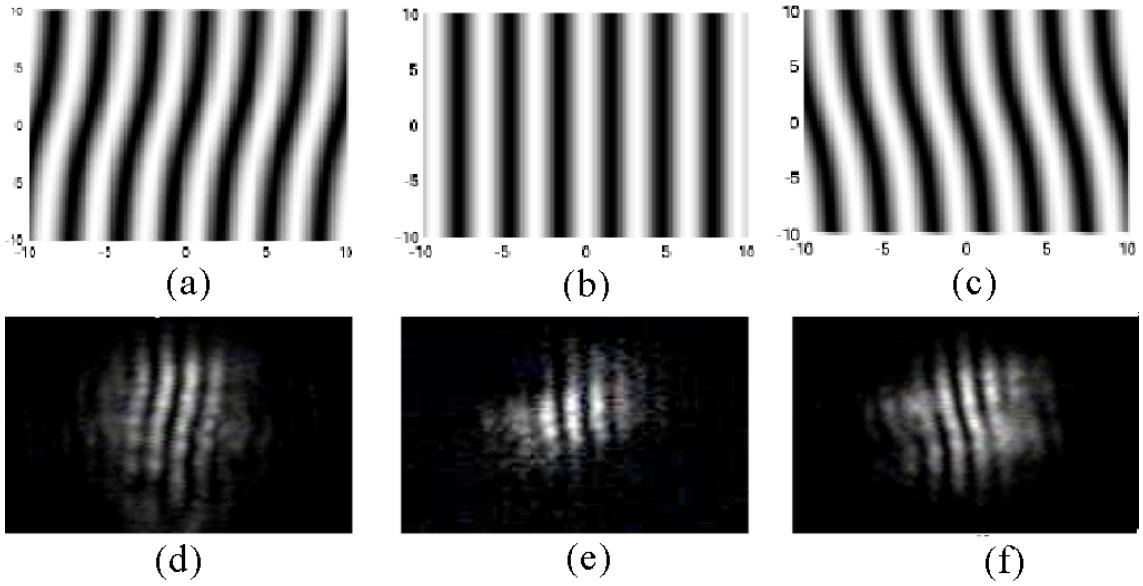

Figure 2.3: (a) Interference pattern from a LG wave-front incident on two slits calculated from Eq. 5.4. (b) Interference pattern from a plain-wave incident on two slits calculated from Eq. 2.3. (c) Interference pattern from a LG wave-front incident on two slits calculated with $-\Delta\phi(y)$. Experimental Far field interference pattern obtained from the $l = +1$ beam (d), $l = 0$ beam (e), and $l = -1$ beam passing through two slits (f).

Fig. 2.3 (d) - (f) shows interference fringes experimentally for $l = +1, 0$, and -1 respectively. The fringes in Fig. 2.3 (d) are shifted in the x-direction as we look from the middle of pattern up or down. The fringes are shifted from the left to the right as we look from the bottom to the top of the interference pattern. Fig. 2.3(f) shows the pattern with a LG beam with opposite helicity, i.e. $l = -1$. This fringe pattern has an opposite shift in its' fringes as the fringes are shifted in the x-direction from right to left as we look from the bottom to the top which is opposite the the shift when $l = +1$. This makes sense as the phase is varying in the opposite azimuthal direction. Fig. 2.3(e) shows shows the vertical fringes of this double slit experiment with a $l = 0$, i.e. TEM_{00}, beam. This diffraction pattern shows no shift in the fringes

as we look from the top to the bottom verifying the constant phase front of this beam. These fringes with no x-direction variation are in agreement with Fig. 2.3 (b).

Along the fringes of Fig. 2.3(d) and (f) lies an apparent interference along the length of the fringes. This interference along the fringes is not seen as much in the (e) of the figure which leads us to believe that this effect is related to the phase variation of the $l = \pm 1$ beams. The apparent interference along the vertically twisted fringes is shown in Fig. 2.4.

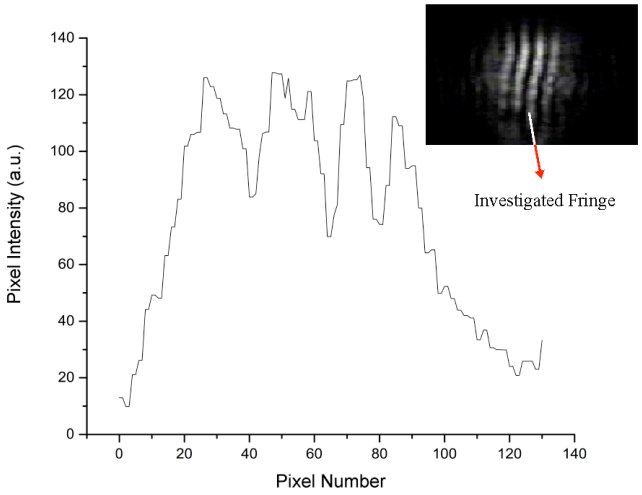

Figure 2.4: Observed interference along one fixed vertical interference fringe of Fig. 2.3(d).

2.3 Conclusions

A Laguerre-Gaussian beam is said to be twisted light because of the helical-wave fronts arising from the azimuthal phase variation. The nature of these twisting light waves can be difficult to understand. This demonstration of the classic double slit interference experiment shows this *twist* in the far-field diffraction pattern. When the phase variation changes handedness from $l = +1$ to $l = -1$ the twist in the diffraction pattern also changes direction. Using a double slit can therefore be used to determine the phase structure of a given wavefront. This is the first known demonstration of Young's double-slit experiment with optical Laguerre-Gaussian beams.

Chapter 3

Ultrafast Laguerre-Gaussian Beams

3.1 Introduction

Most work that has been done to date involving optical vortices has dealt with monochromatic, continuous wave light in the form of Laguerre-Gauss (LG) or Bessel-Gauss waves. Recently there has been development of ultrashort pulses that exhibit a phase singularity. For short pulses with broad spectral bandwiths the desired phase dislocation should be imposed on all spectral components while keeping the pulse width and shape undistorted.

A picosecond LG beam generated inside a laser cavity was recently demonstrated by Jung *et. al.* in 2006 [36]. A femtosecond LG beam generated outside the laser cavity with a computer-generated hologram (CGH) in a $4f$ system was shown by Mariyenko *et. al.* and Bezuhanov *et. al.* [37, 38]. In each of these demonstrations the phase of the LG beam was shown to exhibit the azimuthal phase variation proportional to the charge, or winding number l, unique to the optical vortex. The resulting pulse width was only estimated by Mariyenko *et. al.* who used a starting pulse width of $\sim 25fs$. Their estimation was calculated by inserting a glass coverslip into the path of the vortex beam that was interfered with a plane wave. A pulse width of $\sim 66fs$ was estimated by observing the interference fringes of the $l = 1$ beam and the plane wave disappearing. A more accurate pulse duration measurement was not achieved because of the low conversion efficiency due to using two diffraction gratings in the mode conversion process.

The difficulty in using a CGH, as shown in Figure 1.7, is that when a polychromatic beam of light is passed through a diffraction grating each spectral component diffracts at a different angle. This is known as angular dispersion. The angular dispersion introduced by the forked-grating used to generate the LG beam effectively destroys the incident pulse. Figure 3.1 shows how a broadband source passing through a forked diffraction grating diffracts optical vortices of different wavelengths at different angles.

This chapter discusses the angular dispersion compensation technique and demonstrates the generation and characterization of femtosecond LG beams with angular dispersion compensation.

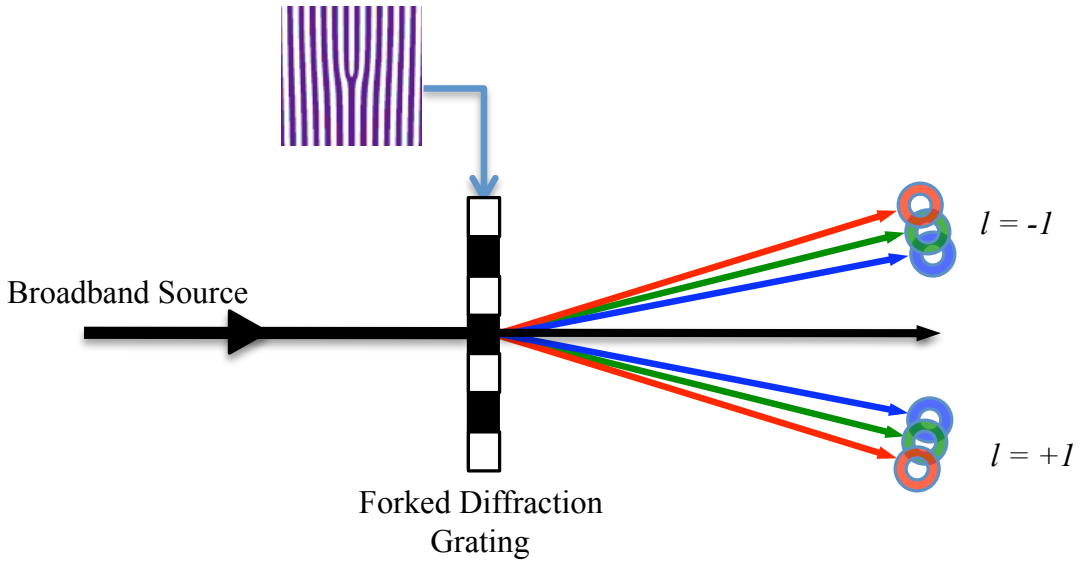

Figure 3.1: A broadband source passing through a forked diffraction grating diffracts optical vortices of different wavelengths at different angles. Only the $\pm 1^{st}$ diffracted orders are shown.

3.2 Dispersion compensation

The following section discusses the method used to compensate for the angular dispersion imparted on a short optical pulse after passing through a diffraction grating.

A schematic diagram showing the $4f$ systems used in this work, also described by Mariyenko *et. al.* [37], to compensate angular dispersion is shown in Figure 3.2. The transverse electric field amplitude from the laser has the form,

$$E(x,y) \propto \exp\Big[-\frac{(x^2+y^2)}{w^2}\Big], \tag{3.1}$$

where w is the beams waist. After propagation through the first diffraction grating with $l = 0$ the field amplitude of the first diffracted order is,

$$E(x,y) \propto \exp\left[-x^2/w^2 + iKx\right] \exp\left[-y^2/w^2\right], \tag{3.2}$$

where $2\pi/K$ is the period of the $l = 0$ grating. Note the grating is a linear ruled grating with its lines along the y-direction thus only the x-dependent factors are affected. After propagating a distance $2f$ away from the first grating, the field right

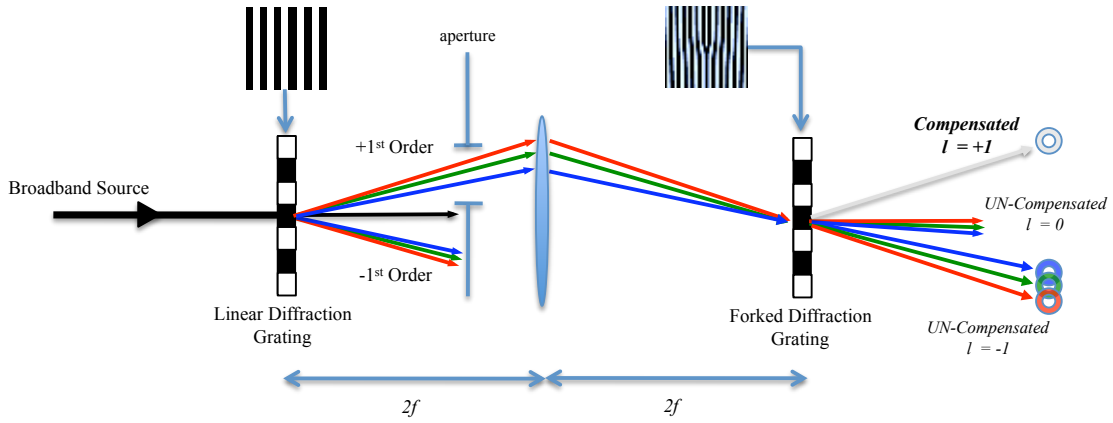

Figure 3.2: $4f$ system used to compensate for angular dispersion due to use of diffraction gratings [37].

before the lens is,

$$E(x,y) \propto \exp\Big[\frac{(x-2Kf/k)^2}{w_c^2} + \frac{ik}{2R}\Big(x^2 + \frac{Kx}{kf}L_r^2 + \frac{K}{k}L_r^2\Big)\Big] \exp\left[-y^2/w^2\right], \tag{3.3}$$

where w_c is the current waist of the beam, k is the wavenumber, R is the radius of curvature of the beam, and L_r is the Rayleigh length. Then, after passing through the lens, which adds a quadratic phase, $\exp\left[-ikx^2\right]$, the electric field just before the second, forked, grating is,

$$E(x,y) \propto \exp\Big[-\frac{(x^2+y^2)}{w^2}\Big] \exp\Big[\frac{ikx^2}{2f}\Big] \exp\left[-iKx\right], \tag{3.4}$$

since the size of the beam is back to the value w. Notice the phase factor $\exp\left[-iKx\right]$ which is the angular dispersion and is opposite to the phase of the beam just after the first diffraction grating. Since the transmission function of the forked diffraction grating is $\exp\left[i(Kx + l\phi)\right]$, the field of the $+1^{st}$-order diffracted order after the second, forked diffraction grating is

$$E(x,y) \propto \exp\Big[-\frac{(x^2+y^2)}{w^2}\Big] \exp\left[il\phi\right], \tag{3.5}$$

which is a Laguerre-Gaussian beam free of any angular dispersion or chirp.

The following sections describe efficient experimental implementation of this technique.

3.3 100 fs LG Beams

To generate a $100fs$ LG pulse a chirped-pulse amplified Coherent Ti:sapphire regenerative amplifier system with up to $4\mu J$ pulse energy at $800nm$ and a 250 kHz repetition rate was used. The pulse duration at the output of this laser was measured to be $80fs$ and the spectral bandwidth was measured to be $\sim 20nm$.

The setup to generate LG beams from this source and compensate for the angular dispersion is shown in Figure 3.3. The *Holoeye Corp.* reflective type spatial light modulator (SLM) is used as the diffractive element. Figure 3.3 shows the $4f$ system used which is slightly different form that described in Figure 3.2 as we make use of the reflective SLM to impliment a *folded* $4f$ dispersion compensation system.

Angular dispersion is compensated by sending the first order diffracted beam (2 in the figure) through a lens, L, and back (3,4) to the top half of the forked diffraction grating where the grating is just a normal ruled grating (5), to give an equal amount of opposite dispersion in the compensated beam. This setup has the advantage of compensating both the (+) and (−) first order diffracted beams and also permits us to see the interference of the two first order modes to verify phase structure without adding any extra optical elements into the setup.

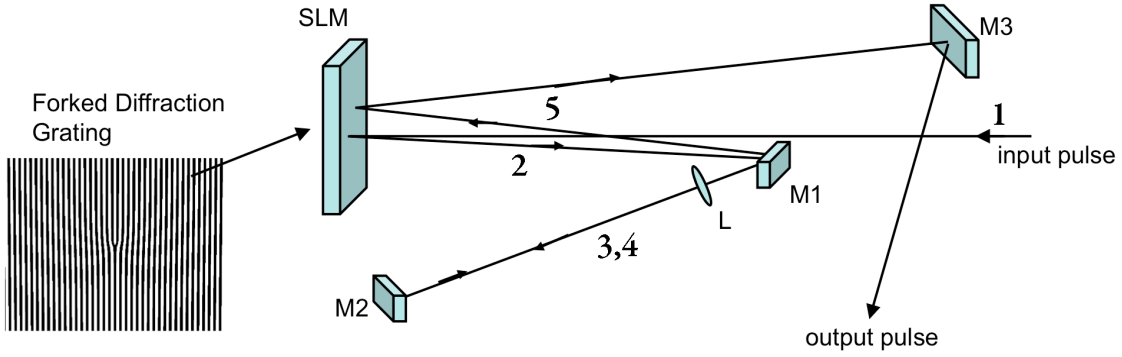

Figure 3.3: The experimental arrangement used to compensate for the angular dispersion introduced by the forked diffraction grating (L- Lens, M- Mirror).

First, because only the +1st-order beam is of interest we can replace the binary diffraction gratings in Figure 3.2 with a blazed grating as shown in Figure 1.7 (e-h) so that the diffractive efficiency can be increased. Figure 3.4 shows the CCD images of the intensity structure of beams that pass through the folded $4f$-dispersion

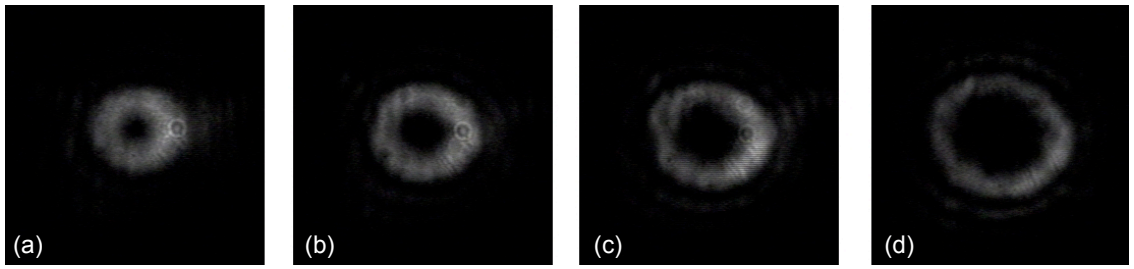

Figure 3.4: The CCD images of the intensity structure of beams that pass through the $4f$-dispersion compensations system for (a) $l = +1$, (b) $l = +2$, (c) $l = +3$, and (d) $l = +5$.

compensations system for (a) $l = +1$, (b) $l = +2$, (c) $l = +3$, and (d) $l = +5$.

Using blazed diffraction gratings allows diffraction efficiencies of approximately $\sim 30\%$ per grating. After the beam reflects off of the grating (on the SLM) the second time the efficiency of the first diffracted order is $\sim 9\%$. So starting with a mean power of ~ 150 mW yields a compensated LG beam with an mean power of $\sim 10 - 13$ mW.

The pulse durations in this work were measure with a second-harmonic generated interferometric autocorrelator. The approximately 10 mW compensated LG beam is passed into the *Femtometer* from *FemtoLasers* autocorrelator which is the lower limit of the mean power necessary to get a signal. Figure 3.5(a) shows the autocorrelation signal when the $4f$-system is properly aligned. The pulse duration is estimated to be $\sim 105 \pm 20$ fs. The accuracy of this measurement is based on the mean power of the LG beam and the modulation frequency of the SLM which can cause fluctuations in the autocorrelation signal.

If mirror $M3$ in Figure 3.3 is moved, forward or backward, chirp is introduced and the resulting pulse duration can be altered because the position of the focal point at the grating changes. The estimated pulse duration when the mirror was moved backward is shown in Figure 3.5(b). The autocorrelation signal, especially, for (b) of this figure is rather noisy due to the rather low intensity of the LG beam despite the use of blazed diffraction gratings. The ultimate goal in the future would be to amplify this low intensity dispersion compensated optical vortex.

What is important to note is that without this dispersion compensation method, the intensity at the center of the optical vortex would not reach zero due to the dispersion introduced and the autocorrelation signal is lost because the pulse is essentially

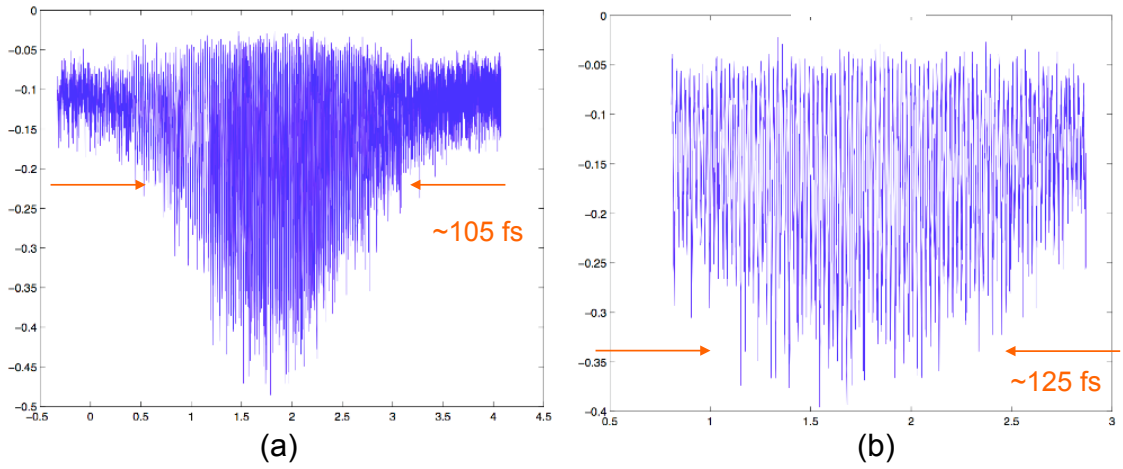

Figure 3.5: Autocorrelation traces measuring the pulse duration of the dispersion compensated LG beams (a) without and (b) with chirp.

destroyed.

Next, the −1st diffracted order can be used in addition to the +1st diffracted order so the resulting interference between the (+) and (−) first diffracted LG orders, i.e. between $+l$ and $-l$, can be used to investigate the phase structure of the dispersion compensated beams. Figure 3.6 shows the setup that allows the interference of the (+) and (−) first order LG beams. When beams with $+l$ and $-l$ are interfered the resulting interference pattern is found to theoretically take the form:

$$\begin{aligned} E_{int} &\propto \left|\exp\left[il\phi\right] + \exp\left[-il\phi\right]\right|^2 \\ &\propto \exp\left[2il\phi\right] + \exp\left[-2il\phi\right] \\ &\propto 2\cos\left(2l\phi\right). \end{aligned} \tag{3.6}$$

Figure 3.7 shows the experimental (a-d) and theoretically calculated (e-h) interference patterns for (a,e) $l = \pm 1$, (b,f) $l = \pm 2$, (c,g) $l = \pm 3$, and (d,h) $l = \pm 4$. Because the interference is proportional to the double angle, 2ϕ, the interference for $l = \pm 1$ has two bright fringes around the beams, $l = \pm 2$ has four bright fringes around the beams, and so forth. The rotational difference between the the experimental and theoretical images are just an overall, constant, phase difference introduced by a difference in path lengths between the two arms of the setup.

This section shows the intensity and azimuthally varying phase profiles for various

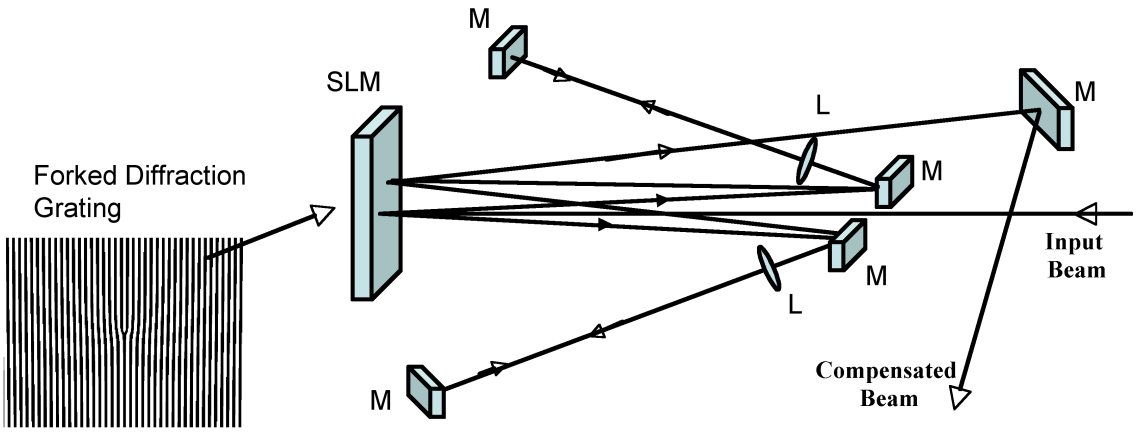

Figure 3.6: The experimental arrangement used to compensate for the angular dispersion introduced by the forked diffraction grating and view the interference between the positive and negative diffractive orders after the gratings (L- Lens, M- Mirror).

LG modes consistent with theory. The temporal profile is also shown to be ~ 105 fs.

3.4 13 fs LG beams

Group velocity dispersion (GVD) can be introduced into an ultrashort, 6.4fs pulse, after passing through the lens in Figure 3.3. GVD increases the pulse width and must also be compensated for if a sub-10fs LG beam is to be created. The GVD accumulated by a pulse passing through a focussing lens and a grating is given by

$$\frac{\partial^2\phi}{\partial\omega^2} = \frac{2L\lambda^2}{\omega c}\Big(\frac{\partial^2 n}{\partial\lambda^2}\Big) - \frac{2fa\lambda^2}{c\omega d^2\cos^2(\theta)}, [39] \tag{3.7}$$

where λ and ω are the wavelength and frequency of the light, L is the lens thickness, n is the index of refraction, d is the period of the grating, θ is the emergence angle, c is the speed of light, and a is a constant ($a << 1$). The first term is the dispersion introduced by a lens that can be removed if the lens is replaced by a concave mirror.

A $6.4fs$ LG pulse was produced from a Ti:sapphire Kerr-lens mode-locked oscillator (Rainbow-DFG from FemtoLasers). This laser emits $6.4fs$ pulses at a 78 MHz repetition rate with a mean power of 150 mW and a 200 nm spectral bandwidth centered at 797 nm. The $4f$ dispersion compensation system that uses a concave mirror rather than a lens is shown in Figure 3.8. The intensity of the LG beam generated was

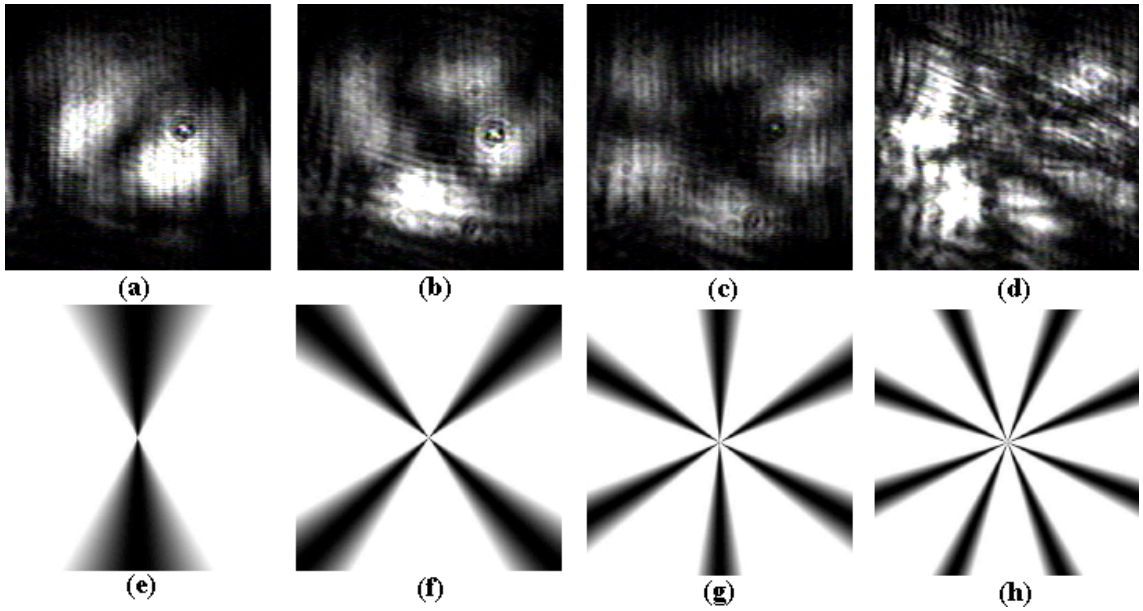

Figure 3.7: Experimental and theoretically calculated interference patterns for (a,e) $l = 1$, (b,f) $l = 2$, (c,g) $l = 3$, and (d,h) $l = 4$, respectively.

again approximately $6 - 10$ mW, the lower limit of the intensity required to achieve an autocorrelation signal from the *Femtometer* from *FemtoLasers*.

Figure 3.9 shows the autocorrelation signal (a) of the beam directly from the laser and (b) of the dispersion compensated LG pulse with $l = +1$ using a concave mirror rather than a glass lens. The pulse duration directly from the laser is estimated to be ~ 8 fs while the LG beam with $l = 1$ is ~ 13 fs after compensation.. The spectra of both of these beams are shown in Figure 3.9 (c) and (d), respectively. While the peaks of the spectra are slightly different, the bandwidth after conversion to a LG beam remains the same.

3.5 Conclusions

This chapter demonstrates the creation and characterization of ultrashort optical vortices from a 100fs and 6.4-fs laser source. A folded $4f$ system is used to compensate for the angular dispersion introduced by the computer generated hologram used to generate the LG beam. For the case of the 13 fs pulse, a concave mirror is used to minimized the group velocity dispersion introduced by a lens used in the system

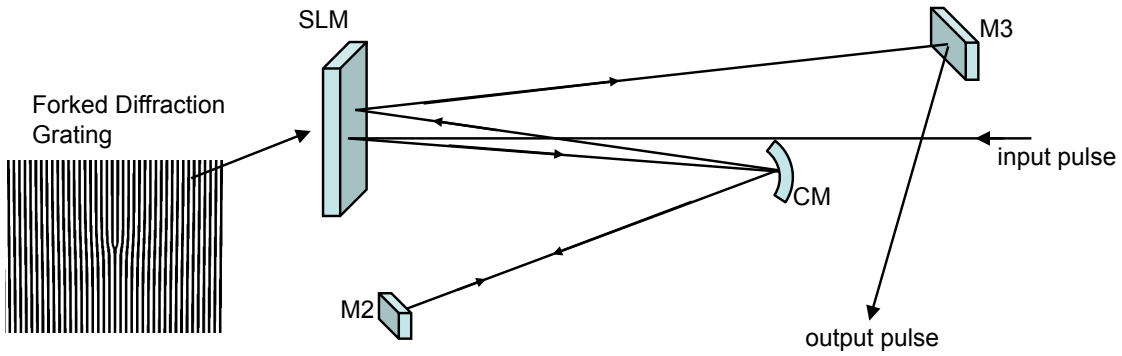

Figure 3.8: The experimental arrangement used to compensate for the angular dispersion introduced by the forked diffraction grating and with the lens from Fig. 3.3 replaced by a concave mirror (CM- Concave Mirror, M- Mirror).

shown and described in Figure 3.3.

The ultrashort LG pulses generated have the intensity and azimuthal phase profiles characteristic of LG beams. The intensity of the LG beam with $l = 1$ was maximized so that the pulse width could be measured with an interferometric autocorrelator. This is the first time such an autocorrelation measurement has been performed on an LG beam.

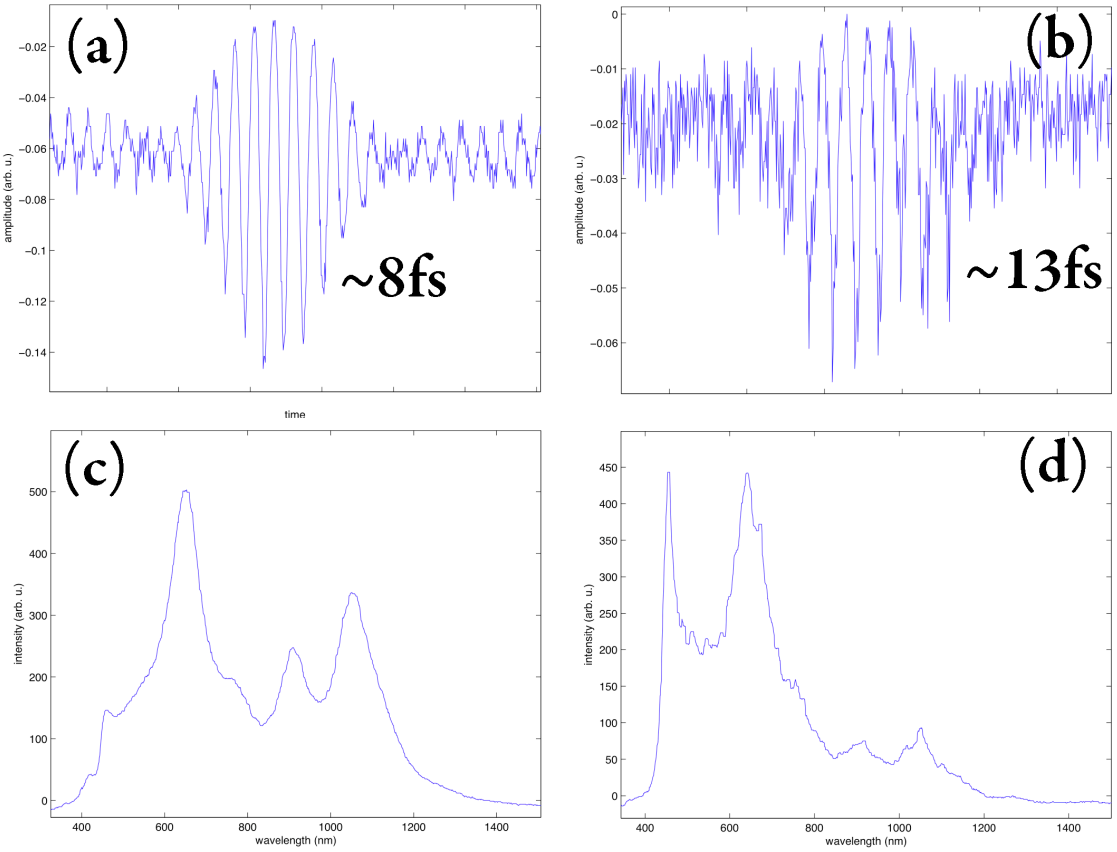

Figure 3.9: Autocorrelation traces of (a) the beam directly from the laser cavity and (b) after the dispersion compensation of the LG beam with $l = 1$. (c) and (d) show the respective spectra of the beam from the laser and the LG beam with $l = 1$.

Chapter 4

Laguerre-Gaussian Supercontinuum: White Vortices

4.1 Introduction

Beams of light that have optical vortices, or phase singularities, have been used to study various optical phenomena in classical and quantum optics including uses in optical tweezing, quantum communication protocols, and telecommunications to name just a few[40, 41, 42, 43, 44]. Most of this work has been performed with monochromatic Laguerre-Gaussian (LG) beams. More recently, white-light optical vortices have been studied and shown to be more versatile in these applications due to the wide spectral bandwidth, azimuthally varying phase structure, and unique quantum number associated with such beams [45]. White-light optical vortices have thus far been demonstrated using partially coherent and incoherent lamp light sources which limit their uses [45, 46]. Coherent white-light supercontinuum generated from ultrashort pulses has been investigated since its discovery by Alfano and Shapiro in 1970 [47] and has shown applications in a wide variety of disciplines from remote sensing to metrology and more [48]. Supercontinuum has thus far not been shown to propagate as an optical vortex.

In this chapter the first coherent Laguerre-Gaussian white-light beam generated from a femtosecond supercontinuum light source with zero angular dispersion is demonstrated.

A monochromatic Laguerre-Gaussian beam has a complex field amplitude proportional to

$$u(r,\phi,z,t)_{p,l} \propto r^{|l|} L_p^l\Big(\frac{2r^2}{w^2}\Big) \exp\Big(\frac{-r^2}{w^2}\Big) \exp\Big(-il\phi\Big) \exp\Big(i\omega t\Big), \tag{4.1}$$

where w is the waist size of the beam, $L_p^l(\frac{2r^2}{w^2})$ is the associated Laguerre polynomial, l is the azimuthal mode, and p is the radial mode. LG beams (with $p = 0$) have orbital angular momentum of $l\hbar$ per photon associated with them where $l = 0, \pm1, \pm2, \ldots$. As a LG beam propagates there is a phase variation around a wave-front which is why these beams are referred to as helical waves[49]. The azimuthal phase variation is also what gives rise to the optical vortex, or phase singularity. LG beams can be generated in several ways [40, 50, 51]. In this chapter optical vortices are generated using an on-axis computer-generated hologram (CGH) on a spatial light modulator.

4.2 Experimental Arrangements

There are two approaches to generating LG white-light supercontinuum:
Method 1: 100 fs Gaussian beam → fs Supercontinuum beam → fs LG Supercontinuum
Method 2: 100 fs Gaussian beam → fs LG beam → fs LG Supercontinuum

4.2.1 Method 1: A Laguerre-Gaussian beam from supercontinuum

The first method of LG supercontinuum generation begins with the self-focusing of the original TEM_{00} femtosecond pulse to generate supercontinuum, then converting the Gaussian supercontinuum to a LG distribution. Supercontinuum Bessel-type Gaussian beams have been formed in a way similar to this[77] and this is the method reported here. This method has an additional advantage that allows the creation of white-light LG superposition states by moving our CGH off-axis.[41] This could not be achieved without very high peak powers using method two described the the next section due to the asymmetric intensity distribution of LG superposition states.

The experimental setup to generate Laguerre-Gaussian supercontinuum beam in this method is shown in Figure 4.1. A 100 fs Ti:Sapphire laser with a central wavelength at 800 nm is focussed by a 5 cm focal length lens (labeled L1) into a 1.5 cm thick piece of BK7 glass. This generates the supercontinuum light source. The white-light then passes through a 10 cm focal length lens (labeled L2) to create a collimated Gaussian beam. To generate a LG field distribution with this source, we project a computer generated hologram onto a spatial light modulator (Holoeye Corp. model: LC-R 720). The CGH used is a forked, blazed diffraction grating designed to put much of the power into the first order diffracted beam and is shown in the figure. We block out all of the reflected beam except the +1st order diffracted beam with an aperture (labeled A) which leaves only beam with the $\exp(il\phi)$ phase structure desired. This beam appears fuzzy as there has been angular dispersion introduced due to the diffraction grating used. The LG supercontinuum beam is then manipulated further by using a folded $4f$-diffraction setup similar to Bezuhanov *et. al.* [53] and described in the preceding chapter to compensate for the angular dispersion introduced by using diffraction gratings. The white-light LG beam is passed through a

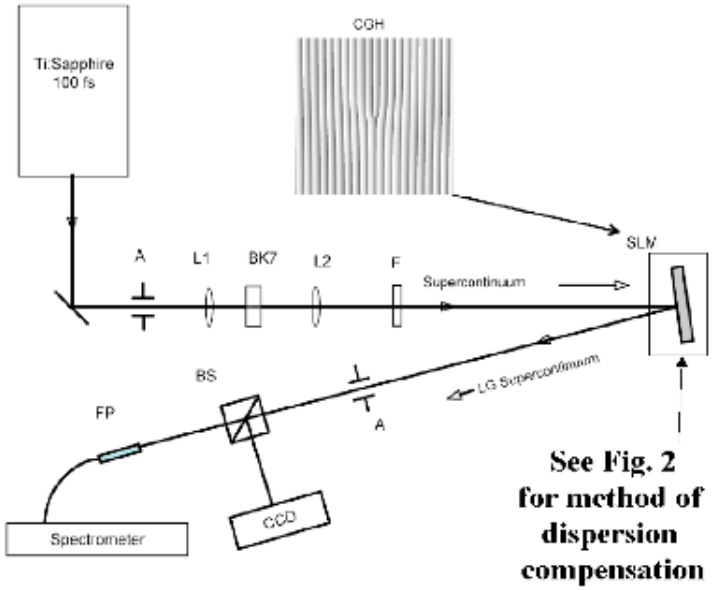

Figure 4.1: The experimental arrangements to generate LG supercontinuum as described by method one. (A- Aperture, L1- 5 cm lens, L2- 10 cm lens, F- short-pass filter with edge at 700nm, BS- beam splitter, FP- fiber probe, SLM- spatial light modulator). An example of a computer generated hologram used is shown.

short-pass filter to block most of the pump beam. This allows us so to better see our Anti-Stokes supercontinuum spectrum. The beams' intensity distribution is recorded on a black and white CCD camera.

Figure 4.2 shows how angular dispersion is compensated, as in the previous chapter, by sending the first order diffracted beams (2) beam through a lens, L, and back (3,4) to the top half of the forked diffraction grating (5), where the grating is just a normal ruled grating, to give an equal amount of opposite dispersion in the compensated beam. This setup has the advantage of compensating both the +1st and the -1st order diffracted beams and also permits us to see the interference of the two first order modes to verify phase structure. Figure 4.3 shows the black and white CCD images of collimated LG white-light beams with $l = \{0, +1, +2\}$ in (a), (b) and (c) of the figure, respectively. The distinct zero intensity regions near the center of (b) and (c) of the figure show that the angular dispersion in the plane of the camera is indeed negligible. Figure 4.4 shows a color photograph of a dispersion compensated

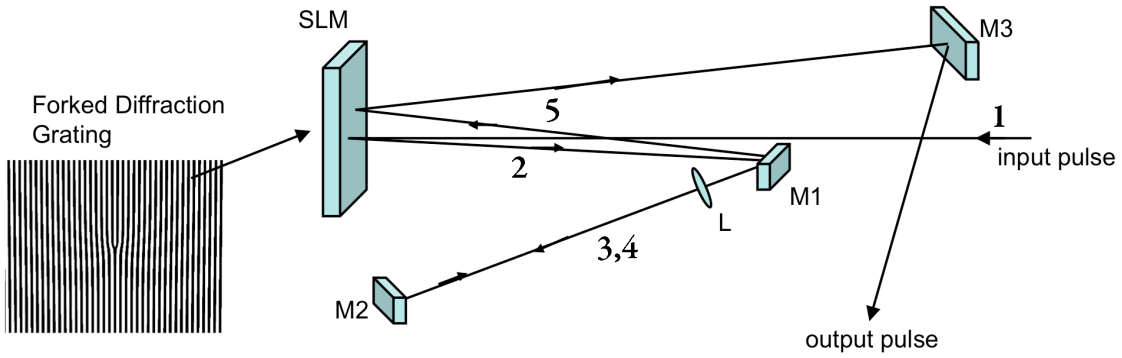

Figure 4.2: The experimental arrangement used to compensate for the angular dispersion introduced by the forked diffraction grating (L- Lens, M- Mirror).

$l = 1$ and $l = 3$ supercontinuum vortex.

The azimuthal phase structure of this beam is verified by looking at the interference pattern a hard-edge creates when placed across the beams diameter. This is similar to methods already reported to measure the varying phase structure of white-light vortices[45]. The hard-edge razor is placed just before the CCD camera blocking just less than half of the LG white-light beam. The resulting interference pattern is shown in Figure 4.3 (d) and shows the π-phase shift across the diameter of the beam. The left side has one more bright fringe than the right side and they meet at the center at the phase singularity (white arrow). This π-phase shift across the diameter of the beam is a distinct feature of all LG beams and shows that we do indeed have a collimated supercontinuum beam with orbital angular momentum proportional to $+\hbar$ per photon.

The LG white-light beam is coupled into a fiber connected to a spectrometer that collects the spectral information. Figure 4.5 shows the spectra of the TEM_{00} supercontinuum (black solid line) and the LG beams (red dotted line). The spectrum has a peak at 780 nm that is due to the pump beam. This plot shows that the pump gaussian beam generates supercontinuum white-light that has a bandwidth of approximately 500 nm. After the supercontinuum is collimated, reflected off of the SLM, and the appropriate LG beam is selected, Figure 4.5 shows the spectrum of this white-light optical vortex (red dotted line). Again, we see the peak near 800 nm shows the spectral position of the pump beam. This plot shows that the LG beam now also

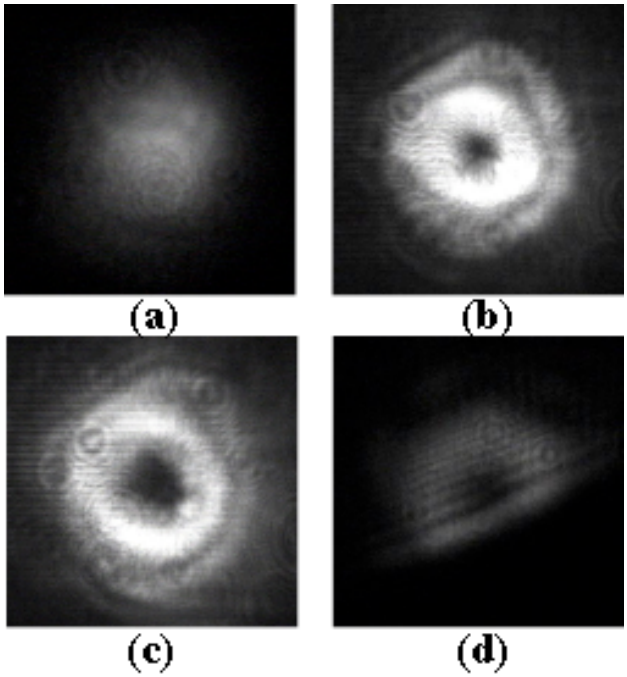

Figure 4.3: Black and white CCD image of the intensity structure of (a) $l = 0$, (b) $l = +1$, (c) $l = +2$ Laguerre-Gaussian Beams and (d) the interference that shows the azimuthal phase structure of the beam shown in (b).

has a bandwidth of approximately 450 nm. The intensities of these two beams are significantly different so the intensities of the spectra should not be compared. They are used, however, to show our LG beam does indeed have an increased bandwidth and we are looking at a LG supercontinuum beam. The LG bandwidth is reduced slightly due to the wavelength efficiency of the SLM used.

Figure 4.6 shows the CCD images of both an $l = 3$ beam that is uncompensated, (a) of the figure, and compensated for angular dispersion, (b) of the figure. Below the images intensity cross sections are shown. The intensity cross section of the uncompensated beam in (a) does not have a clear region of zero intensity in the center. The compensated beam in (b) clearly has a clear vortex region of zero intensity.

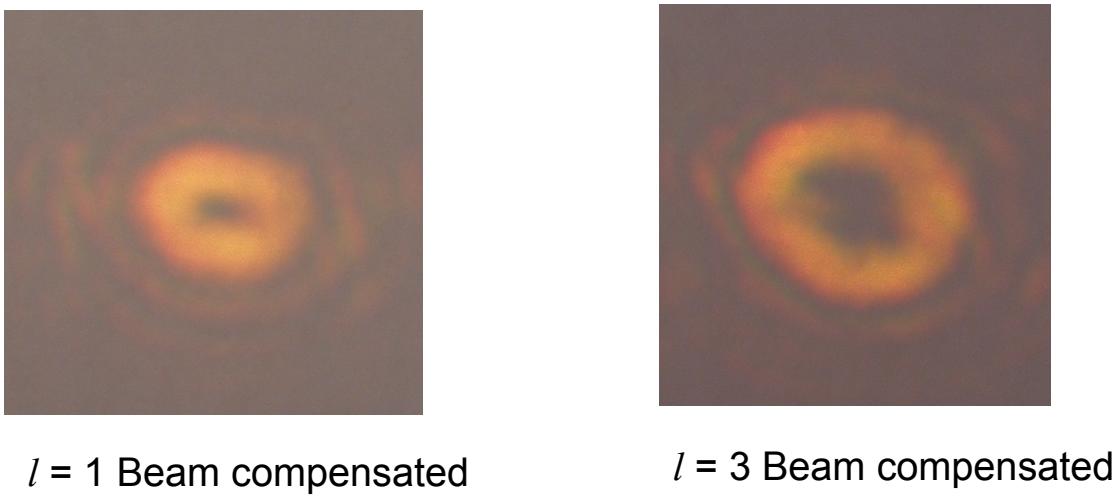

Figure 4.4: A color photograph of a $l = 1$ and a $l = 3$ dispersion compensated supercontinuum optical vortex.

4.2.2 Method 2: Supercontinuum from a Laguerre-Gaussian beam

The second method to generate Laguerre-Gaussian Supercontinuum starts by generating femtosecond LG pulses and then focusing the resulting beam into a medium where self-focusing and four-wave mixing induce spectral broadening giving a supercontinuum vortex [47]. The experimental setup to generate Laguerre-Gaussian supercontinuum beam in this method is shown in Figure 4.7. The difficulty of creating LG white-light in this way is that energies on the order of $10 - 20\ \mu J$ are necessary to create the filamentation that facilitates supercontinuum generation[52]. This becomes difficult to realize using a CGH approach to generating optical vortices because of damage to the spatial light modulator (SLM) that we use to project the CGH at high energies and the relatively low diffraction efficiencies. Vuong et. al. in Ref. [13] show that multiple filaments are formed when a LG beam is focused in a water cell, the total number is dependent on the peak power of the pulsed light. The phase structure of the filaments formed and the resulting structure of supercontinuum is not known or discussed in previous literature and should be investigated further in future work.

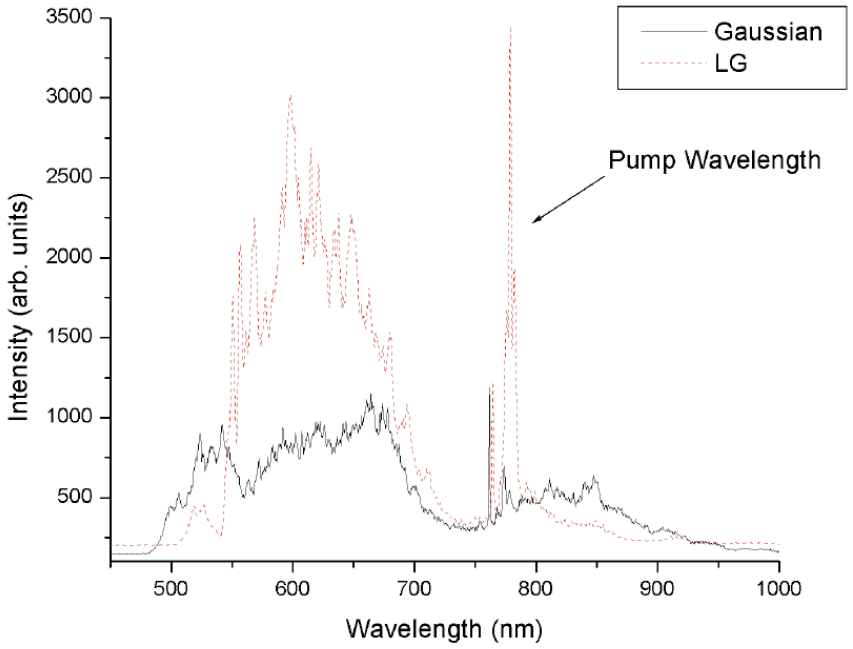

Figure 4.5: The spectra of gaussian supercontinuum (black solid line) and Laguerre-Gaussian supercontinuum beams (red dotted line).

4.3 Conclusions

In conclusion, this chapter demonstrates the first coherent Laguerre-Gaussian white-light beam generated from a femtosecond supercontinuum light source. The spectrum of the white-light LG beam covers a similar spectral range as the Gaussian beam, which using BK7 as the material to generate supercontinuum, was found to be approximately 500 nm. A new variation on angular dispersion compensation is also shown that allows simple interferometric verification of phase structure of vortices. In this case we show angular dispersion compensation of a LG supercontinuum beam for the first time. Polychromatic Laguerre-Gaussian beams have promise in experiments where two-photon interactions must be avoided such as in optical trapping of biological materials. These beams are also of interest in telecommunications applications where information can now be manipulated by wavelength and orbital angular momentum state. Superposition states described by Vazir et. al. in Ref. [2] can now

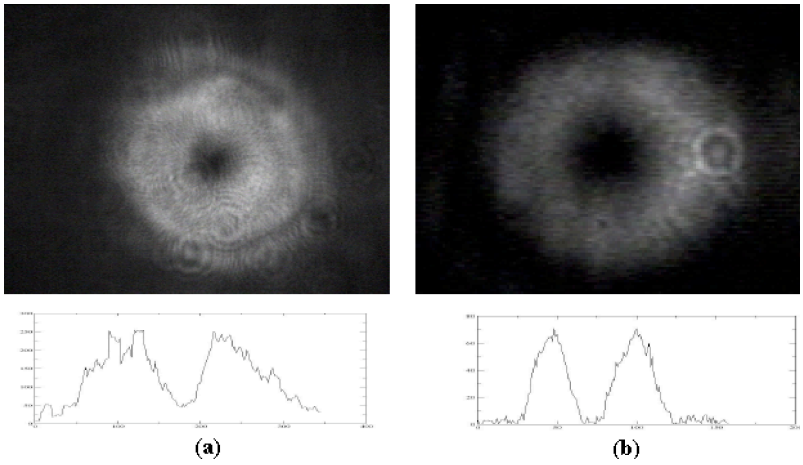

Figure 4.6: CCD images of (a) an uncompensated beam and (b) a compensated beam. The intensity cross section of each beam is shown under the respective image.

be realized in a white-light source and can be used for such applications. Supercontinuum *plus* this extra degree of freedom from the orbital angular momentum can lead to development towards 100's of terabit data transmission rates.

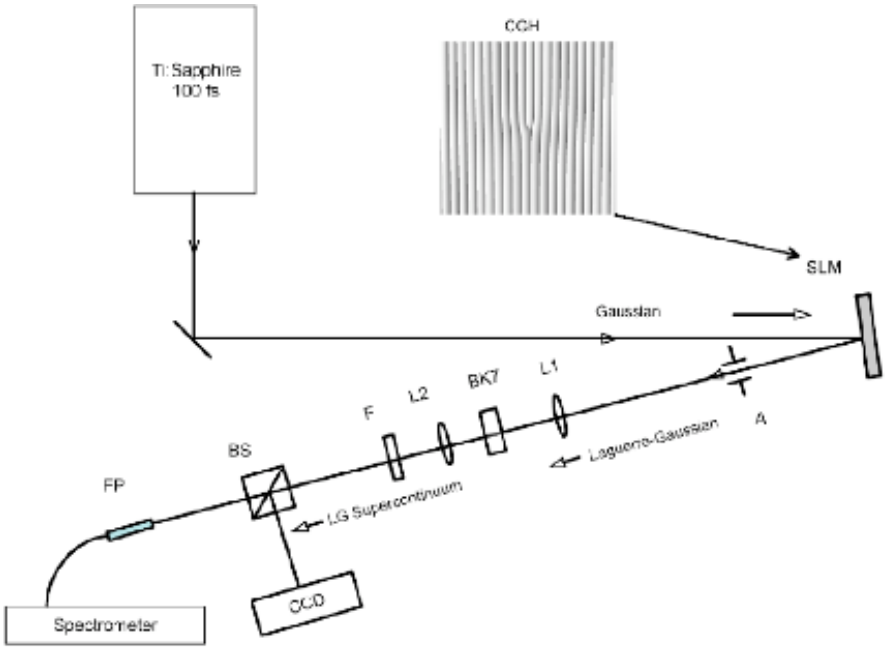

Figure 4.7: The experimental arrangements to generate LG supercontinuum as described by method two. (A- Aperture, L1- 5 cm lens, L2- 10 cm lens, F- short-pass filter with edge at 700nm, BS- beam splitter, FP- fiber probe, SLM- spatial light modulator). An example of a computer generated hologram used is shown.

Chapter 5

Optical Vortex Imaging

5.1 Introduction

Over the past decades, many techniques have been devised to improve optical imaging through turbid media. The general problem is how to detect and image objects buried or camouflaged inside a region where scattering significantly degrades imaging contrast and resolution. Light propagating through a turbid medium undergoes multiple scattering that randomizes the polarization, phase, and direction of propagation. To overcome these obstacles, various techniques have been introduced to extract image information from the scattering background without altering the scattering medium properties, such as time-resolved techniques [55, 56, 57], frequency-domain techniques [58], nonlinear optical techniques [59], optical low-coherence [60], Fourier space gate techniques [61], and polarimetric imaging [62, 63]. The important limitation of these post-scattering methods is their inability to image through highly scattering medium effectively. A new, innovative approach is necessary to circumvent some of these limitations.

The new optical imaging technique that is presented in this chapter relies on the optical forces associated with the intensity gradient in a beam of light to look inside the vortex of a Laguerre-Gaussian beam, shown pictorially in Figure 5.1. Beams of light were first used to manipulate micron sized particles by Ashkin [64]. He showed that a tightly focussed beam of light had a force associated with it in the region of the beam with a high intensity gradient. This optical force, that points in the direction of the gradient and is proportional to the gradient of the intensity, can move micron-sized particles. If the micron-sized particles, that make up a scattering medium, can be moved such that a region of "fewer" scattering particles exist, then an image with increased contrast and resolution can be achieved.

The optical force on a sphere due to a beam of light is given by [64, 65],

$$\begin{aligned} F_{gradient} &= \frac{1}{2}\alpha\nabla I \\ &= \frac{1}{2}\alpha\nabla|u|^2 \\ &= \frac{1}{2}n_b^2\left(\frac{n^2-1}{n^2+2}\right)a^3\nabla|u|^2 \end{aligned} \tag{5.1}$$

where u is the field amplitude of the beam and α is the polarizability of a sphere suspended in a surrounding medium, $n(=n_a/n_b)$ is the ratio of the index of refraction of the sphere (n_a) to the surrounding medium, and a is the radius of the sphere.

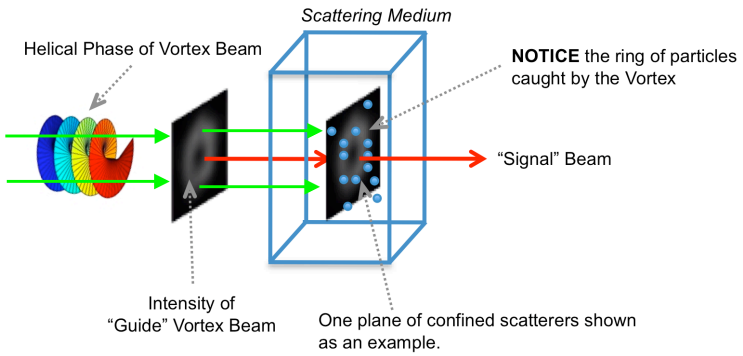

Figure 5.1: A depiction of the optical vortex imaging scheme to move scattering particles into the ring of the vortex. The reduced particle concentration inside the vortex allows better imaging or signal transmission in that region.

The optical force acts as an optical potential well that draws particles in its path into the bottom of the potential well. Figure 5.2 shows the optical potential for (a) a Gaussian wave and (b) a LG wave. With a Gaussian wave particles settle into the the bottom of the potential well in the center. With a LG wave particles settle into the double wells, leaving the central region free of particles.

In this chapter the optical gradient force is investigated for both Gaussian and Laguerre-Gaussian fields and the application of this imaging technique is shown and discussed. Traditionally, the optical gradient force is used to trap particles in two- or three-dimensions. This method of imaging relies on using two beams of light. One is used to guide scattering particles out of the way (using the optical force) of a second, low intensity imaging "signal" beam.

The second section of this chapter shows that the optical force associated with a Gaussian beam can weakly confine scattering particles, showing that beams of light can move scatterers out of the way of a second beam of light like a tornado. The third section of this chapter shows the use of an optical vortex used as a "guide" beam to increase imaging contrast in a scattering medium.

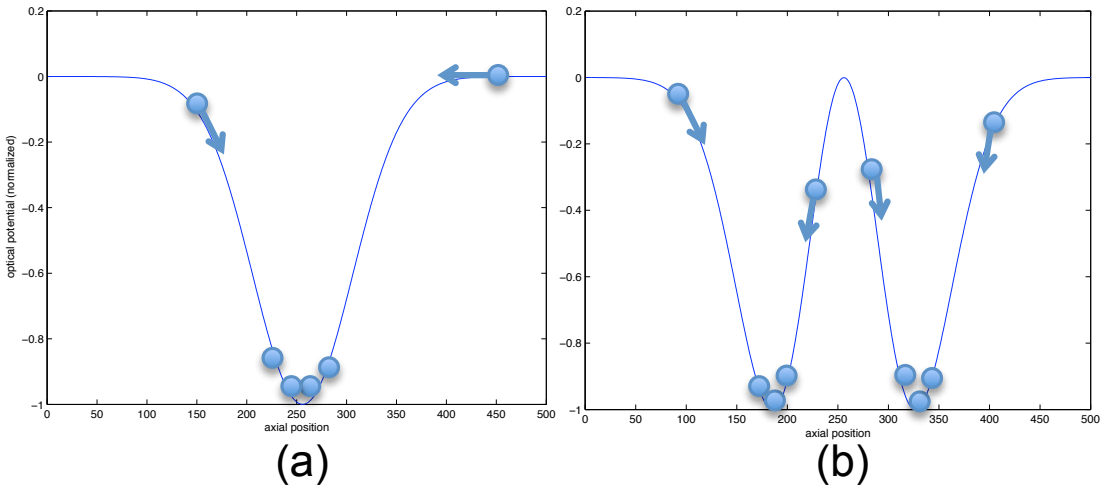

Figure 5.2: The optical potential due to (a) a Gaussian optical wave and (b) a LG optical wave. Particles are depicted as dots. The arrows indicate the direction the particles would travel in such a potential.

5.2 Gaussian source to increase light scattering

A Gaussian beam has a field amplitude proportional to

$$u(r) = u_o \exp\left(-\frac{r^2}{w^2}\right), \tag{5.2}$$

where w is the waist size of the beam and u_o is the electric field constant. The optical force on a dielectric particle associated with a Gaussian optical field described in Eq. 5.2 is

$$F_{Gaussian} \propto -u_o^2 \left(\frac{4r}{w^2}\right) \exp\left(-2r^2/w^2\right) \hat{r}. \tag{5.3}$$

The gradient force for the field given in Eq. 5.3 is shown in Figure 5.3 (a). The direction and magnitude of the arrows in this figure represent the direction and magnitude of the force on a dielectric sphere while the intensity of the Gaussian beam is shown in the background.

Figure 5.3 (b) shows pictorially, a random distribution of scatterers (blue circles) distributed in some medium. Part (c) of this figure shows that when a Gaussian beam is turned *on* because the force pointing towards the center of the beam, the scatterers are more likely to be in the central region of the beam.

The experimental arraignment to investigate the affect of a "guide" beam "pulling" scattering particles into its' path is shown in Figure 5.4. A green ($\lambda = 532nm$)

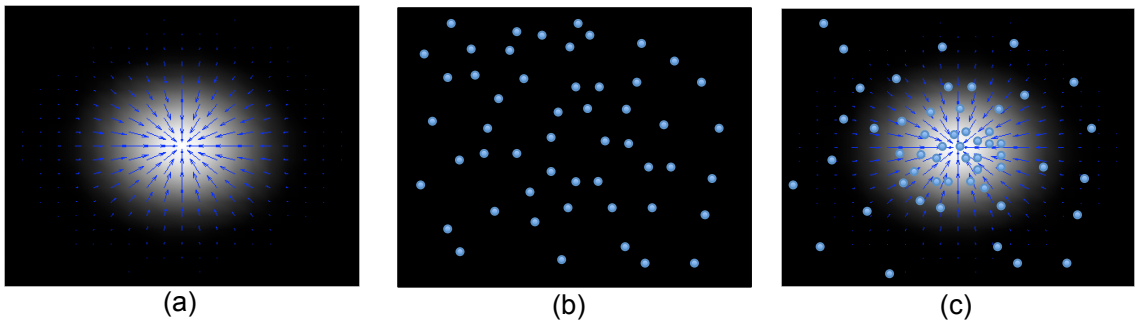

Figure 5.3: (a) The direction and magnitude of the arrows represent the direction and magnitude of the force on a dielectric sphere. The intensity of the Gaussian beam is shown in the background. (b) A pictorial representation of scatterers (blue circles) randomly distributed without the presence of a Gaussian optical field. (c) The Gaussian beam turned on, the optical force shown as vector arrows, and the scatterers "settling" in the region of the smallest optical gradient.

Gaussian, "guide" beam is directed through a glass cell containing a turbid medium made of polystyrene spheres suspended in distilled water. A red He-Ne laser ($\lambda = 633nm$), "signal" beam, is made to travel co-linear with the guide beam by using a dichroic mirror designed to transmit the green light and reflect the red light. The light scattered at 90^0 is collected with a set of lenses so an image of the scattered light is recorded on a color CCD camera. A filter is used that block almost all of the green light before the camera. In addition, because the green, "guiding" light has a high intensity (because the trapping force is proportional to the beam intensity), only the data from red channel of the CCD camera is used. After this process is used to filter out all of the green light from the CCD images, approximately $1-4$ counts of green light are detected per frame (out of a maximum 255) which are later subtracted from the images of the red "signal" beam as background.

Images from the red channel of the color CCD camera are recorded at one frame per second. To demonstrate the trapping properties of the Gaussian beam images were recorded with the red beam alone, with the red beam *and* the green beam on together and again the red beam on alone. At time $t = 0$ the "guide" beam starts *off*. At approximately $t = 5 - 8s$ the "guide" beam is turned *on* until it is again turned off at $t = 50 - 55s$. Figure 5.5 shows the red scattered light from polystyrene spheres (d $= 0.05\mu m$) at 90^0 imaged on the CCD camera at one instance of time. The images

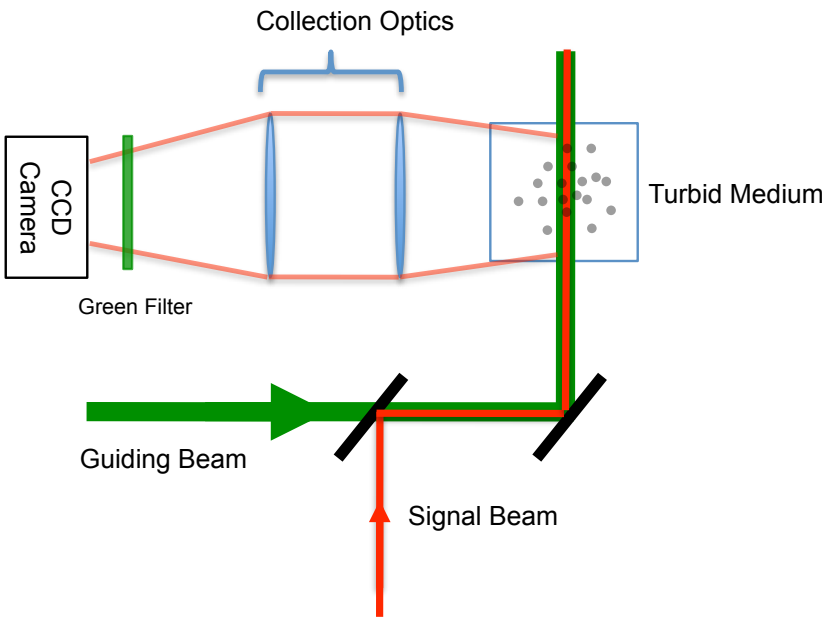

Figure 5.4: The experimental arrangement to investigate the particle confining effect a Gaussian beam will have on Rayleigh scatterers.

from the CCD camera are processed by selecting a region in the center of the cell, i.e. the area between the vertical white lines in Fig. 5.5, obtaining a cross section of the beam and averaging the intensity of each cross section, at each time in that region of the beam.

Figure 5.6 (a) shows the averaged Rayleigh scattering intensity over time with a small concentration of $0.05\mu m$ sized particles. The "guide" beam is turned *on* at $t = 5s$ and left on until approximately $t = 49s$. When the "guide" beam is turned on the intensity of the red scattered light, from the "signal" beam increases from approximately 3700 to 3850 when the green beam intensity is $1.1W$ (green line), from 3750 to 4000 when the green beam intensity is $1.6W$ (blue line), and from 3650 to 4050 when the green beam intensity is $2.1W$ (black line). This corresponds to approximately a 5.5%, 7.4%, and a 10.2% increase, respectively which is shown in Figure 5.7. The increase in the scattering intensity around $t = 40s$, especially for the blue and black curves, corresponds to "large" particles, possibly dirt or residual particles from previous experiments floating around and increasing the scattering intensity. The image in Figure 5.5 shows such large particles yielding bright red spots near the center of the cell. The red line in Figure 5.7 is the best fit to the data points

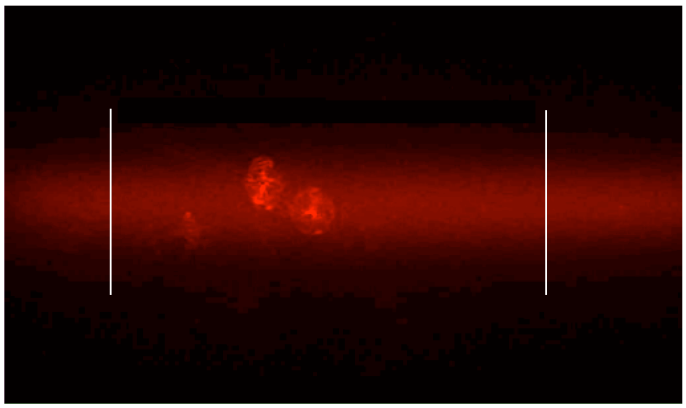

Figure 5.5: One frame of the video obtained by the color CCD camera of the red light scattered from the polystyrene spheres in water solution. The area within the vertical white lines is the region of each frame that is processed computationally.

plotted as blue dots. The red line has a slope of ~ 4.7 and $r^2 = 0.99$. This highlights the dependence of the optical force on the "guide" beam intensity.

When the particle concentration is doubled, the percent increase when the "guide" beam is turned *on* decreases to approximately 2.7%, 3.4%, and 5.7% for $1.1W$, $1.6W$, and $2.1W$ respectively. The concentration doubles, the trapping efficiency decreases by almost a half. This data is shown plotted in Figure 5.8 as blue dots. This figure also shows the linear best fit line in red that has a slope of ~ 3.0 and $r^2 = 0.90$. The value of the slope is less than that of the scattering medium with a weaker concentration. This shows that the confining efficiency of the Gaussian "guide" beam decreases for higher concentrations of particles.

These results demonstrate that a high intensity Gaussian beam can be used to confine scattering particles in turbid media. In fact, you can see this confining effect by eye when you look at a laser beam traveling in air. When a laser is turned on, dust particles in the air or in liquid becomes visible and seem to congregate in the region of the Gaussian beam. The limiting factor in this work is the sensitivity to alignment in the experimental arraignment and the purity, or homogeneity, of the scattering medium to understand the phenomena at hand. It was found that if the beams were not made *exactly* collinear traveling through the cell, the confining effect of the high intensity Gaussian "guide" beam was significantly diminished. This experiment is a proof of principle of this new two-beam approach for imaging through turbid media.

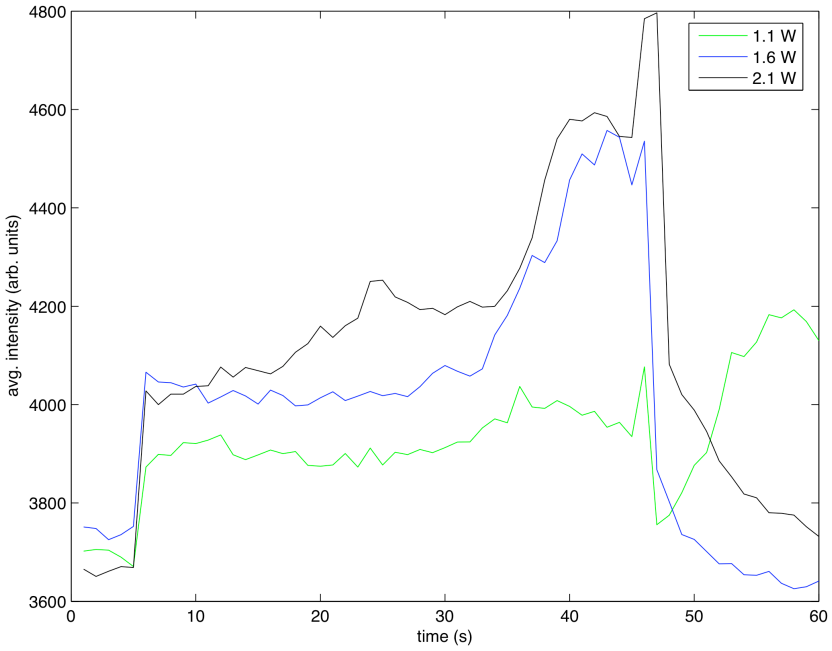

Figure 5.6: The averaged scattering intensity for $0.05\mu m$ particles in distilled water when the "guide" beam intensity is $1.1W$ (green), $1.6W$ (blue), $2.1W$ (black).

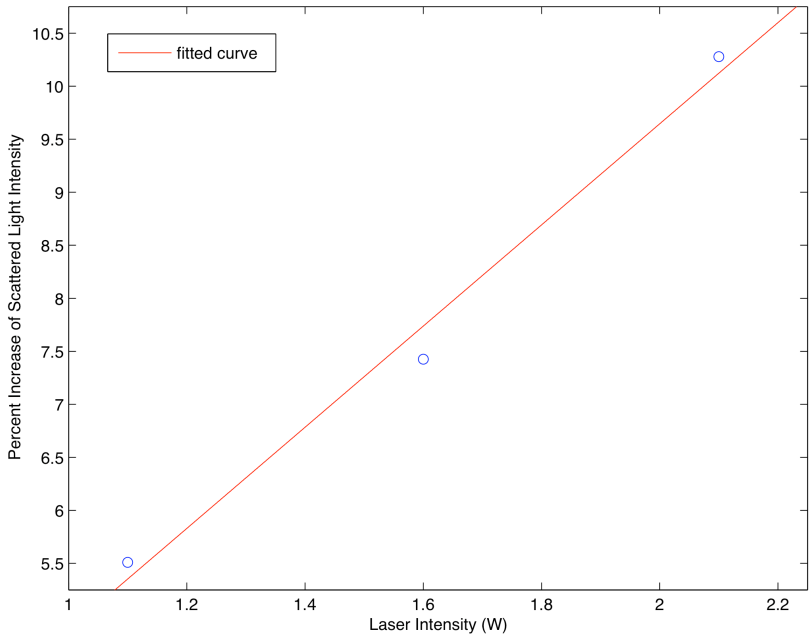

Figure 5.7: The percent change when the green beam is turned *on* as a function of guide beam intensity. The red line is the linear best fit with a slope of ~ 4.7.

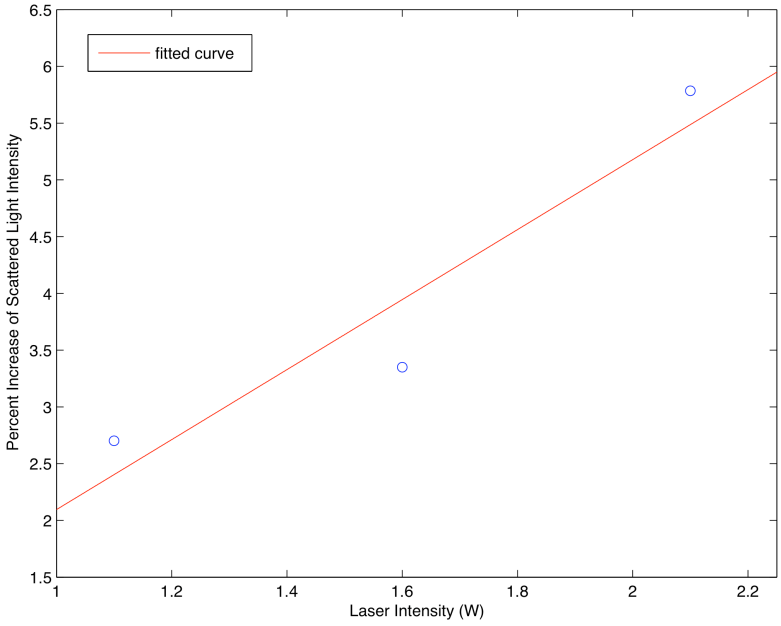

Figure 5.8: The percent change when the green beam is turned *on* as a function of guide beam intensity for an increased particle concentration. The red line is the linear best fit with a slope of ~ 3.0.

5.3 LG source to increase image contrast in a scattering medium

A Laguerre-Gaussian beam with $p = 0$ has a field amplitude proportional to

$$u(r,\phi)_l = u_o \left(\frac{r}{w}\right)^{|l|} \exp\left(-\frac{r^2}{w^2}\right) \exp\left(-il\phi\right), \tag{5.4}$$

where w is the waist size of the beam and l is the charge of the LG beam.

The optical force associated with an optical field described in Eq. 5.4 is

$$\begin{aligned} F_{LG} &= u_0^2 \left[2|l| \left(\frac{r}{w}\right)^{2|l|-1} - \frac{4r^2}{w^2}\left(\frac{r}{w}\right)^{2|l|}\right] \exp\left(\frac{-2r^2}{w^2}\right)\hat{r} \\ &= 2u_0^2 \left(\frac{r}{w}\right)^{2|l|} \left[|l| \left(\frac{r}{w}\right)^{-1} - 2\right] \exp\left(\frac{-2r^2}{w^2}\right)\hat{r} \end{aligned} \tag{5.5}$$

The gradient force in the $\hat{r}$-direction for the field given in Eq. 5.5 is shown in Figure 5.9. The direction and magnitude of the arrows in this figure represent the direction and magnitude of the force on a dielectric sphere while the intensity of the Gaussian beam is shown in the background.

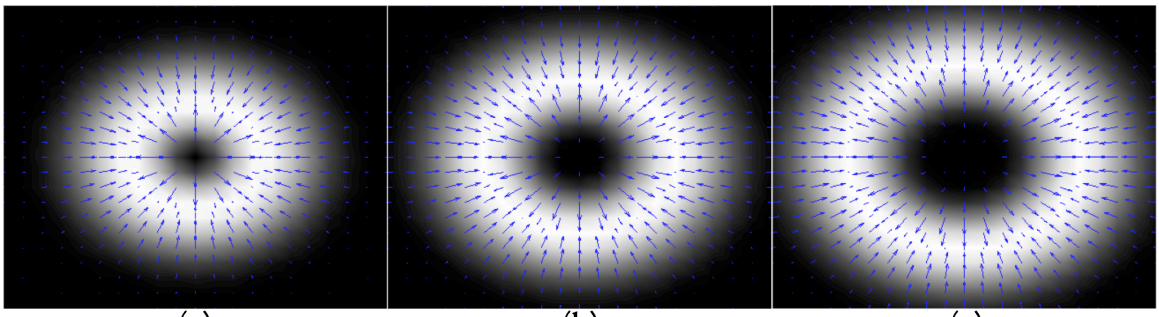

Figure 5.9: The direction and magnitude of the arrows represent the direction and magnitude of the force on a dielectric spheres for (a) $l = 1$, (b) $l = 2$, and (c) $l = 3$. The intensity of the Gaussian beam is shown in the background.

Figure 5.9 shows that a particle placed in the path of a Laguerre-Gaussian beam of light will feel a force pointing towards the region where the gradient of the intensity is zero, i.e. the center of the *ring* of the LG beam, for (a) $l = 1$, (b) $l = 2$, and (c) $l = 3$. This force field will attract particles to the region of highest intensity until

that region is filled with particles. This leaves a region of fewer scatterers inside the vortex that is cleaner for a second beam to image through.

The experimental arraignment to investigate the affect of a "guide" beam "pulling" scattering particles away from the center of the vortex is shown in Figure 5.10. A high intensity green Laguerre-Gaussian "guide" beam is made to travel collinear with a low intensity red Gaussian signal beam by using a dichroic mirror (DM) that transmits green light and reflects red light.

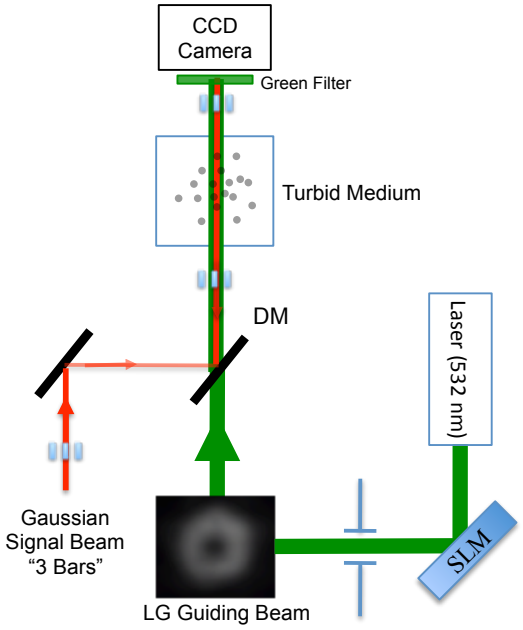

Figure 5.10: The experimental arrangement to investigate the confining effect a Laguerre-Gaussian beam will have on Rayleigh scatterers (DM: dichroic mirror).

The LG beam is generated with a computer generated hologram projected on a spatial light modular as described in previous chapters. The manufacturers stated upper limit of the intensity that can be reflected off of the SLM before damage to the liquid crystal display is $5W$. With the setup used, this leads to a maximum intensity of the LG beam being approximately $500mW$. Figure 5.11 shows the laser power of the vortex beam in relation to the laser power directly from the laser head. A conversion efficiency of approximately 10% is achieved in this setup.

Figure 5.12 (a) shows a color CCD image of three bars of a red "signal" beam aligned so that it travels inside the green, "guide" vortex of the LG beam with $l = 1$. The three vertical red bars are created by passing the He-Ne beam through a bar

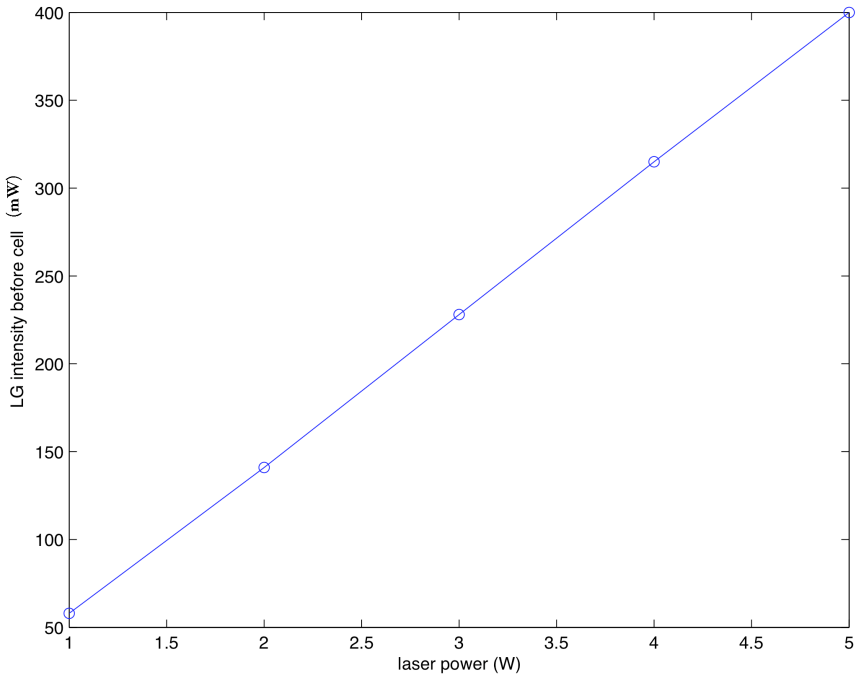

Figure 5.11: The laser intensity of the LG beam with $l = 1$ as a function of the laser intensity directly from the laser head. The conversion efficiency is about 10%

chart. The full color image is filtered and only the red channel of the CCD camera is analyzed. The image of the three bars alone is shown in Figure 5.12 (b) in grayscale while (c) of this figure shows the vortex alone in grayscale. Notice in the image of the vortex alone in part (c) that the vortex is not totally symmetric as there is a brighter area directly to the right of the vortex followed by a darker region just to the right of the the brighter region. While this is not ideal it will present interesting results upon analysis of signal transmission through a scattering medium.

A cross section that is 10 pixels high and runs across all three bars is chosen to be analyzed. Figure 5.13 shows the intensity of the cross sections of the three bars shown in Figure 5.12 (b) transmitted through a glass cell filled with distilled water and a low concentration of $0.05\mu m$ diameter polystyrene spheres for $90s$ of data collection. There are 90 cross sections plotted in this figure. The green, "guide" beam is turned *on* at approximately $t = 8s$ and turned *off* at $t = 50s$. Looking at the region of the peaks of the three bars shows that there is some change taking place during the 90 seconds the CCD camera is recording images.

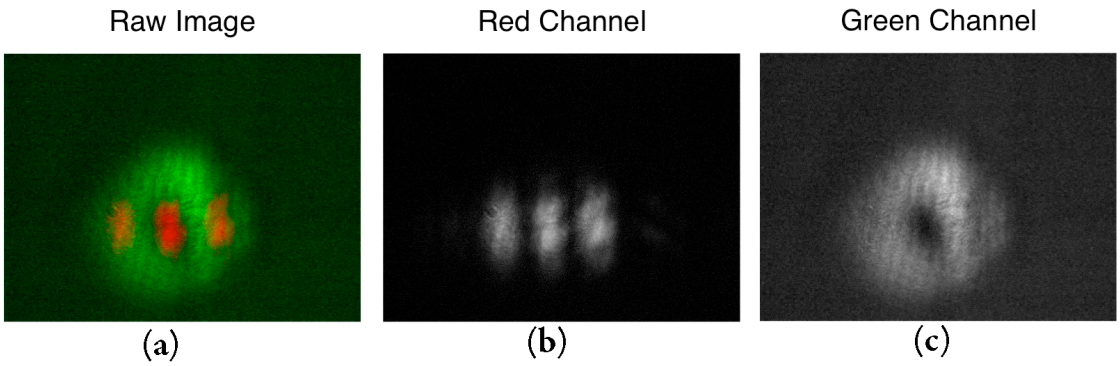

Figure 5.12: (a) A color CCD image of the the image of three bars of a red, "signal" beam traveling inside the vortex of the green, "guide" beam with $l = 1$. (b) Grayscale image of the three bars taken from the image in (a). (c) Grayscale image of the LG beam taken from the image in (a).

Figure 5.14 shows the average intensity surrounding each peak. The average intensity of the left and right peaks (left and right bars) are the bottom two, blue and red curves, respectively. The top, green curve is the average intensity of the center peak (center bar). The intensity changes abruptly at $t = 8s$ and $t = 50s$ for each plot representing when the "guide" beam is turned on and off.

Based on the theory and discussion earlier in this chapter what is expected to occur when the green, "guide" beam is turned on is the intensity of the red, "signal" should increase inside the hole of the vortex while the signal of the bars in the ring of the vortex should decrease. Scattering particles are expected to move away from the hole of the vortex and towards the ring. What appears to be happening in Figure 5.14 is that for the center bar (top, green curve) the intensity goes down slightly at first then up and again back down when the "guide" beam is turned off. The intensity of the right bar (center, red curve) on the other hand, goes *up* when the "guide" beam is turned on and *down* when it is turned off. These two results are contrary to what is expected.

This contrary result can be explained by looking back at Figure 5.12 (c) which shows the intensity profile of the LG "guide" beam. Earlier the asymmetric intensity profile of this optical vortex was pointed out. It turns out that the right red bar which is plotted in Figure 5.14 (red, middle curve) is directly in the region of the darker region towards the right side of the optical vortex. For clarity, the vortex is

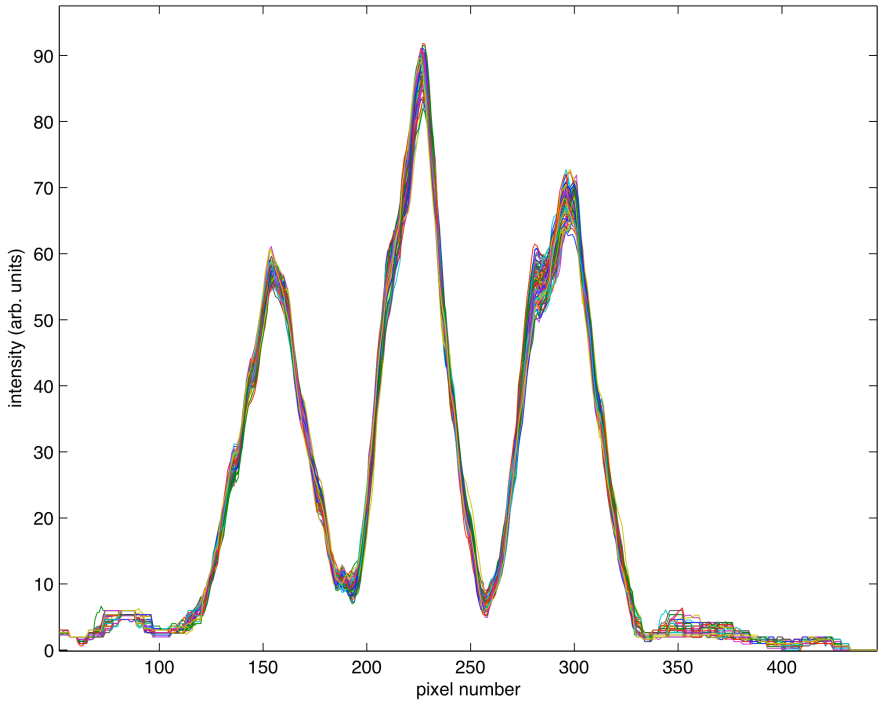

Figure 5.13: A cross section of the image in Figure 5.12 (b) showing the intensity of the 3 bars plotted as a function of pixel number.

shown on its own in Figure 5.15. The region where the right red bar signal is being improved is highlighted by the white box.

Another feature of Figure 5.14 worth discussing is the short lived nature of the improvement in the signal of the right red bar. The signal increases at $t = 8s$ until about $t = 11s$ by about 10% then decreases to a level very close its original value. This can lead to two conclusions, both based on the fact that the confining effect that can manipulate scatterers is based on the intensity *gradient* of a light beam. First, when the $500mW$ vortex beam is turned on, the gradient in space *and* time is very large. The overall change in intensity is very high at first. After this first perturbation to the system, the intensity gradient is solely in the transverse plane in space and not very great which leads to a very little, if any, confinement of scatterers.

The second conclusion that can be drawn from this experiment is that the $500mW$ right before the scattering medium is an estimate of the minimum intensity needed to see an improvement using this imaging technique. This is verified by the results of the last section which demonstrate that for $500mW$ almost no change due to a

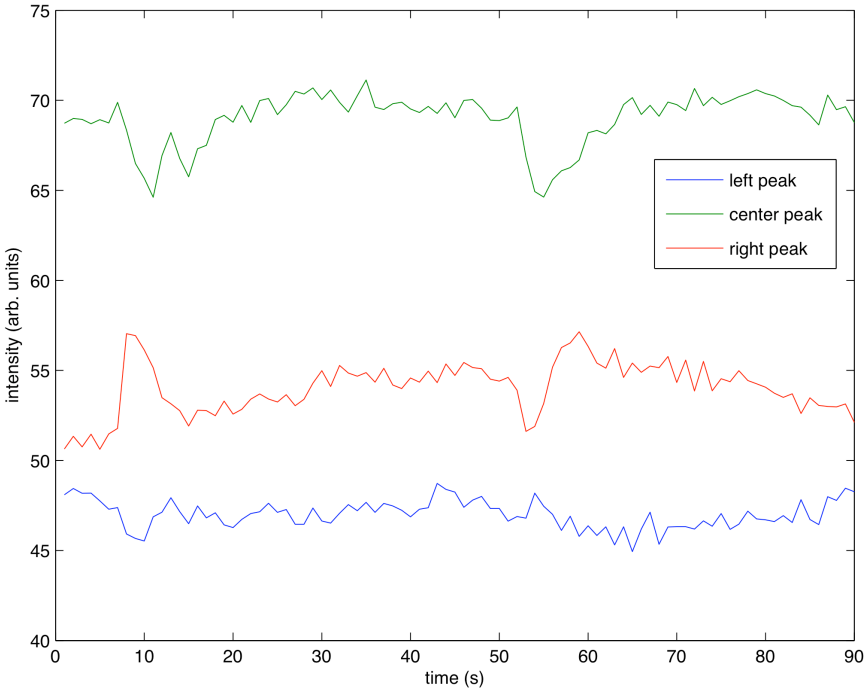

Figure 5.14: Cross sections of the image in Figure 5.12 (b) showing the intensity of the three bars plotted as a function of pixel number. There are 90 cross sections in total shown. Each cross section is from an image taken every second.

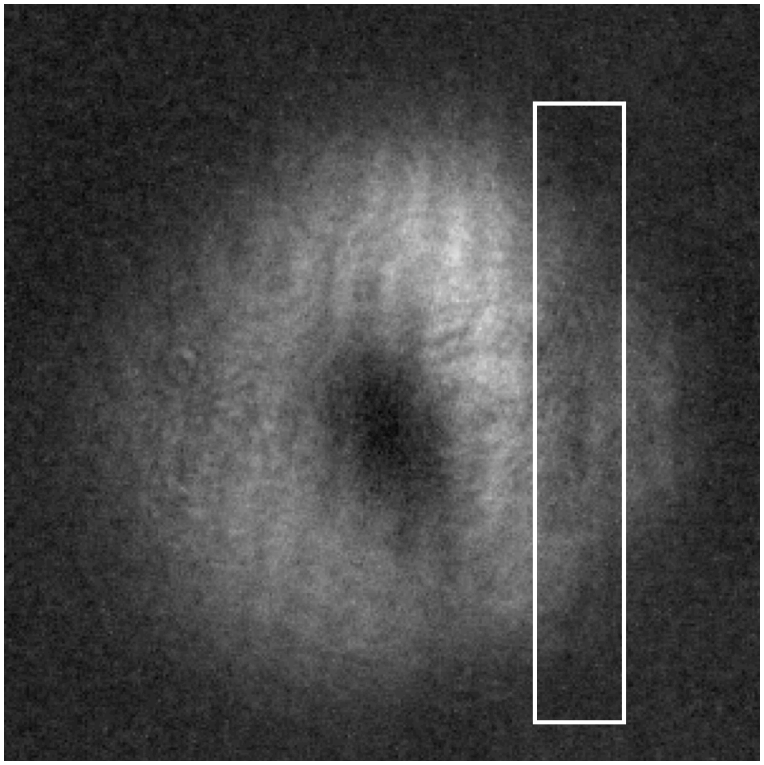

Figure 5.15: An image of the optical vortex shown alone, taken from Figure 5.12. The white box shows a region where the signal of the bars is improved due to the local intensity gradient.

"guide" beam should be present.

5.4 Conclusions

Optical imaging through turbid media can be a difficult task no matter how one looks at it. This optical vortex imaging technique, that relies on the optical force associated with an intensity gradient, holds tremendous promise in its ability to clear away scattering particles for a clear image to be obtained. This chapter has, unfortunately, not found the ideal conditions or arraignment to carry out this technique. This chapter has, however, shown that there is promise in using a pump-probe or guide-signal approach to imaging through turbid media using the optical forces of light.

The first section of this chapter demonstrated theoretically how the optical vortex imaging method should work. The second section of this chapter demonstrated that

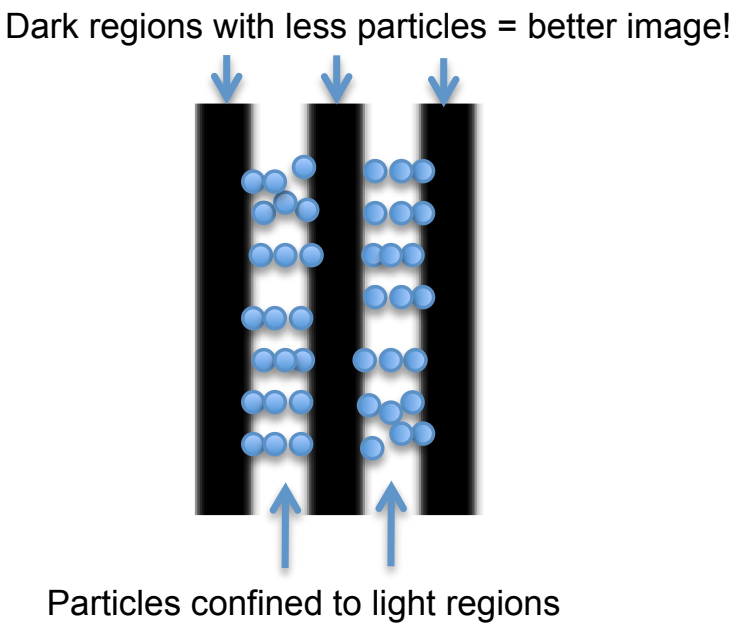

Figure 5.16: An optical field that has a spatially varying intensity similar to the boxcar function. Particles would be confined to "light" regions leaving the "dark" regions free to image through.

scattering particles can be confined to near the center of a path of a Gaussian beam of light traveling through a scattering medium. There is dependence to the intensity of the guide beam and the concentration of scattering particles in the medium. The third section of this chapter aimed to show that an optical vortex could be used to draw scattering particles out of the path of an imaging beam traveling inside the optical vortex core.

One limiting factor that hampered the total proof of concept of this technique is the incident intensity of the optical vortex, guide beam. Due to the limitations on the generation method of the LG beams (intensity limitations imposed by the spatial light modulator), the total maximum power available before entering the scattering medium was $400 - 500mW$. One way to circumvent this problem is to use another, non-diffractive, method of generating the LG beams, perhaps intra-cavity.

An interesting feature to come out of this work is the realization that an optical vortex is not necessary to accomplish this guide-signal imaging technique. The boxed in region of the vortex in Figure 5.15 shows all that is necessary to confine particles

is a region that has a high intensity gradient. This could be accomplished with some sort of boxcar light field as shown in Figure 5.16 as the light would be in the bright regions and not in the dark regions. This could also possibly be achieved by using a guide beam that is pulsed in time that would create the temporally varying intensity gradient that could possibly more particles more efficiently. Both methods are worth investigating in future works.

Chapter 6

Cylidrical Vector Beams

6.1 Introduction

Recently, beams of light that have optical vortices have gained much attention as shown in the preceding chapters. The Laguerre-Gaussian wave is a class of optical vortex that arise from an azimuthally varying phase. Optical vortices can also arise from polarization singularities, manifesting types of radial or azimuthal "vector" polarization states. Most recently, there has been considerable interest in the generation of so called "cylindrical vector beams" (CVB) for numerous possible applications in optical imaging [66], particle acceleration [67], and efficient laser cutting and welding [68] among others. Further, radially and azimuthally polarized light enables the focusing of beams beyond the diffraction limit while generating stationary longitudinal electric and magnetic fields [69]. These CVBs are generated through several different methods including: intra-cavity polarization manipulation [70], computer generated holograms [71], offset input to few-mode optical fibers [72], and excitation of optical fibers with higher order modes [73]. While these methods have been devised to generate vector-beams, simple beam generation with a single optical element from a fundamental TEM_{00} mode does not exist.

This chapter discusses superpositions of polarization states and the generation of cylindrical vector optical vortex beams by directly propagating a fundamental laser mode through a spun optical fiber.

6.2 Hybrid-azimuthal polarization imaginary (HAPi) states

The general expression for the polarization state of a radially or azimuthally polarized beam is given by:

$$\hat{\epsilon} = \begin{cases} a\cos\phi\hat{x} + b\sin\phi\hat{y} \\ -a\sin\phi\hat{x} + b\cos\phi\hat{y} \end{cases}, \tag{6.1}$$

respectively, where ϕ represents the angular position around the beam and a, b are coefficients allowing for circular or elliptical polarization states at some angles.

With $a = b = 1$ these two polarization states are shown in Figure 6.1 (a) and (b), respectively. Figure 6.1 (c) shows the polarization state for $\hat{\epsilon} = -a\sin\phi\hat{x} + b\cos\phi\hat{y}$ with $a = 1$ and $b = i$. This is a *new* polarization state that I am defining to be a **hybrid-azimuthal polarization imaginary (HAPi) state**. It has a polarization

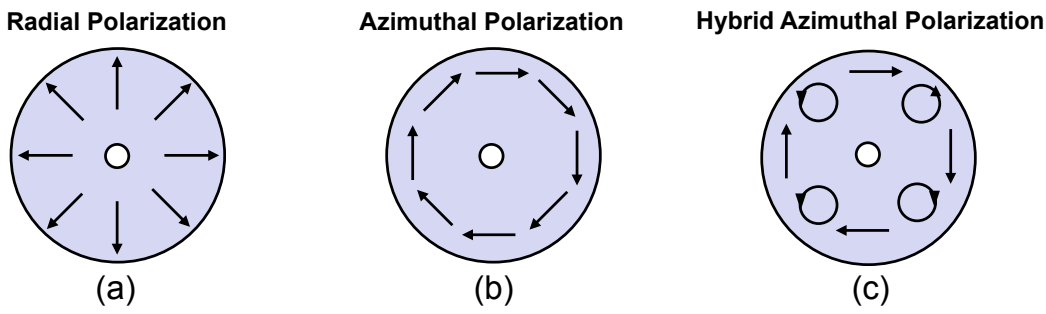

Figure 6.1: Depiction of (a) radial and (b) azimuthal polarization states given by Eq. 6.1 for $a = b = 1$. (c) A hybrid azimuthal polarization state (HAPi) when $a = 1$ and $b = i$

similar to azimuthal polarization at $\phi = 0, \pi/2, \pi$, and $3\pi/2$ and circular polarization at $\phi = \pi/4, 3\pi/4, 5\pi/4$, and $7\pi/4$.

This hybrid-azimuthal polarization can be written as a superposition of the transverse electric, $TE_{0,1}$, and the hybrid electric, $HE_{2,1}$ modes. The $TE_{0,1}$ mode is the same mode as the azimuthal polarization shown in Figure 6.1 (b) while the $HE_{2,1}$ mode is itself a hybrid mode and shown in Figure 6.2. Figure 6.2 shows that $TE_{0,1} + iHE_{2,1}$ gives rise to the HAPi state. The factor of i before the $HE_{2,1}$ mode represents a π-phase difference between the two polarization states which is what is responsible for the circular polarization components in the final polarization. This is very similar to the π-phase difference between vertical and horizontal polarization which gives rise to circular polarization and spin angular momentum. It is also similar to a π-phase difference between two orthogonal Hermite-Gaussian modes that gives rise to a Laguerre-Gaussian mode and orbital angular momentum, i.e. $HG_{1,0} + iHG_{0,1} = LG_0^1$.

6.3 Angular momentum of hybrid-azimuthal polarized light

Following the methods of Section 1.3 the linear and angular momentum of the HAPi mode can be calculated. Note, the polarization state in Eq. 6.1, $\hat{\epsilon}$, is a function of ϕ yet is shown with unit vectors $\hat{x}$ and $\hat{y}$. These could just be written as $\hat{r}$ and $\hat{\phi}$ but

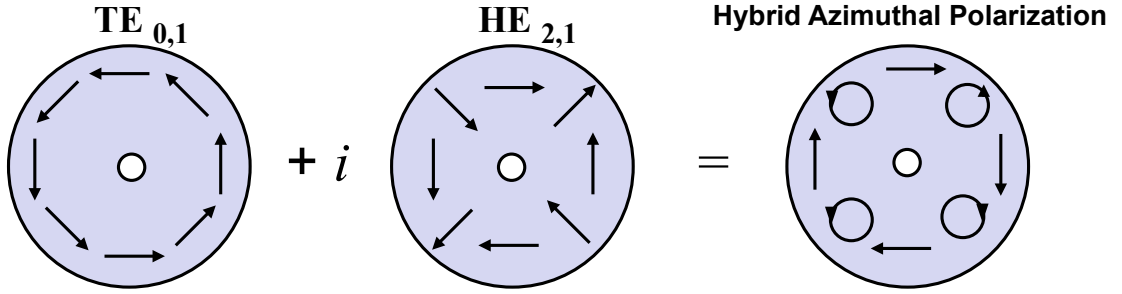

Figure 6.2: Superposition of the $TE_{0,1}$ and the $HE_{2,1}$ yielding the hybrid-azimuthal state. The factor of i before the $HE_{2,1}$ mode represents a π-phase difference between the two states.

this would not allow for the constants a and b which are the terms responsible for the manifestation of the HAPi state. Assuming the vector potential takes the form,

$$\vec{A}(\vec{r}) \propto (-\sin\phi\hat{x} + i\cos\phi\hat{y})u(r)\exp[ikz], \tag{6.2}$$

where $u(r) = r\exp[-r^2]$, $\phi = arctan(y/x)$ is the azimuthal position around the beam and $r = \sqrt{x^2+y^2}$, the electric and magnetic fields calculated from Eq. 1.30 and 1.29, respectively are:

$$\vec{B}(x,y,z) = -ik\Big[(\sin\phi\hat{y} + i\cos\phi\hat{x})u(r) + (i/k)(\sin\phi\frac{\partial}{\partial y} + i\cos\phi\frac{\partial}{\partial x})u(r)\hat{z}\Big] \tag{6.3}$$

and

$$\vec{E}(x,y,z) = i\omega\Big[(-\sin\phi\hat{x} + i\cos\phi\hat{y})u(r) + (i/k)(-\sin\phi\frac{\partial}{\partial x} + i\cos\phi\frac{\partial}{\partial y})u(r)\hat{z}\Big]. \tag{6.4}$$

Calculating the time averaged linear momentum, $\vec{p}$, using these fields gives

$$\begin{aligned}\vec{p} &= \frac{\epsilon_0}{2}\left[(\vec{E}^* \times \vec{B}) + (\vec{E} \times \vec{B}^*)\right] \\ &= -\omega\epsilon_0 \sin\phi\cos\phi\left(\frac{\partial}{\partial x} + \frac{\partial}{\partial y}\right)|u(r)|^2(-\hat{x}+\hat{y}) + \omega\epsilon_0 k|u(r)|^2\hat{z}. \end{aligned}\tag{6.5}$$

From Eq. 6.5, the angular momentum density of the HAPi state is calculated as,

$$\begin{aligned} j_z &= \left[\vec{r}\times\left(\epsilon_0\vec{E}\times\vec{B}\right)\right]_z \\ &\propto \frac{1}{2}\epsilon_0\omega r\sin 2\phi\left(x\frac{\partial}{\partial x} + y\frac{\partial}{\partial x}\right)|u|^2 \\ &\propto \frac{1}{2}\epsilon_0\omega r\sin 2\phi\,(\vec{r}\cdot\nabla_\tau)\,|u|^2, \end{aligned}\tag{6.6}$$

where $\nabla_\tau = (d/dx + d/dy)$ and using the double angle identity, $\sin\phi\cos\phi = (1/2)\sin 2\phi$. Comparing this to the angular momentum calculated for a circularly polarized beam of light, as in Section 1.3, we see that the "σ" from Eq. 1.40, that had a value of ± 1 depending on the handedness of the circularly polarized light and 0 for linearly polarized light, now takes the spatially varying value of $\sin 2\phi$. This ϕ-dependence implies that *locally*, the angular momentum varies from 0 at $\phi = 0$ to $+\hbar$ at $\phi = \pi/4$ to 0 at $\phi = \pi/2$ to $-\hbar$ at $\phi = 3\pi/2$ and so on. Wherever there is a circular polarization in Figure 6.1 (c), the angular momentum is $\pm\hbar$. The word, *locally*, is stressed above because calculating the *total* angular momentum by integrating across the beam finds,

$$J_z = \int\int r dr d\phi j_z = 0, \tag{6.7}$$

as the integral over ϕ of j_z in Eq. 6.7 from 0 to 2π is zero. So, while the spatial variation in the angular momentum density for the hybrid polarization is non-zero, the total angular momentum is in fact, zero. This differs from the angular momentum from the cases of pure radial or azimuthally polarized light as the angular momentum density for both of these modes is zero, i.e. $j_z^{radial} = 0$ and $j_z^{azimuthal} = 0$.

6.4 Hybrid-azimuthal polarization from spun fiber

The experimental setup to generate a vortex beam with the HAPi state is shown in Figure 6.3. A vertically polarized He-Ne laser with a wavelength of 632.8 nm passes through a half-wave plate and is coupled into a spun, or "twisted", fiber provided by *Corning Inc.* with a 20x microscope objective. The output from the fiber is decoupled through a second 20x microscope objective and passed through a linear polarizer that acts as an analyzer to characterize the output polarization state. The intensity distribution is recorded on a black and white CCD camera.

The fiber provided by *Corning* is spun at a rate of 20 turns per meter as it is made, the piece used is approximately ten meters long, and has a cutoff wavelength of 740nm. Because the laser propagating in the fiber is below the cutoff wavelength multiple modes can propagate, notably the $TE_{0,1}$ and the $HE_{2,1}$ modes. The spin creates an azimuthal variation of the index of refraction creating some spatially varying birefringence along the fiber. This adds the π-phase difference necessary to generate the hybrid-azimuthal mode depicted in Figure 6.2.

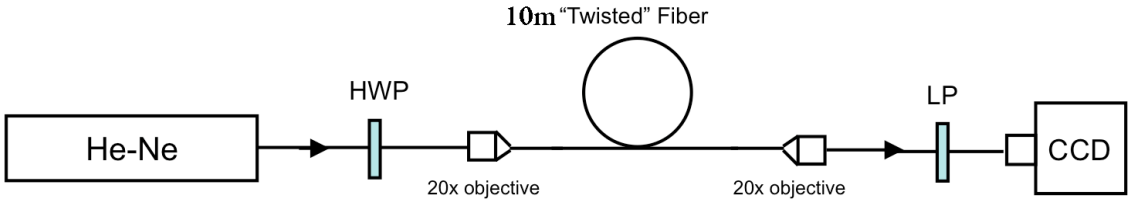

Figure 6.3: Experimental arrangement to generate and analyze cylindrical vector beams with a spun fiber. (HWP: half-wave plate, LP: linear polarizer)

An example of typical output from the twisted fiber with an input polarization of 45^o is shown in Fig. 6.4(a). This figure shows the black and white CCD images of the collimated output from the twisted fiber when the analyzer polarization is set at (b) 0^o, (c) 45^o, and (d) 90^o. When the analyzer is set to 0^o or 90^o the intensity pattern resembles a first-order Hermite-Gaussian mode and when the analyzer is set to 45^o the intensity distribution resembles a first-order Laguerre-Gaussian mode. This twisted fiber is effectively acting as a mode converter transforming a zero-order mode into a first-order mode. The orientation of the incident polarization does not destroy the HAPi output form the twisted fiber.

Table 6.1: Dependence of spin rate of fiber on the output intensity and polarization

Spin Rate	Output Intensity	Output Polarization
0 turns / m	$HG_{1,0}$ or $HG_{0,1}$	Linear
10 turns / m	Almost Vortex	Slight Superposition
20 turns / m	Vortex	Hybrid-Azimuthal

The dependence of the spin rate on the output state of the fiber is shown in Table 6.1. When light is coupled into a fiber with the same cutoff wavelength and indices of refraction is *not* spin, i.e. a spin rate of 0 turns per meter, no vortex is seen. Rather, a Hermite-Gaussian mode is seen that is linearly polarized. Depending on the alignment of the coupling into the fiber, the output is is either a $HG_{1,0}$ or a $HG_{0,1}$ mode. If light is coupled into a fiber with a spin rate of 10 turns per meter, the output looks like a blend between a vortex and a HG mode and the polarization is not quite linear and not quite the hybrid-azimuthal polarization. When light is

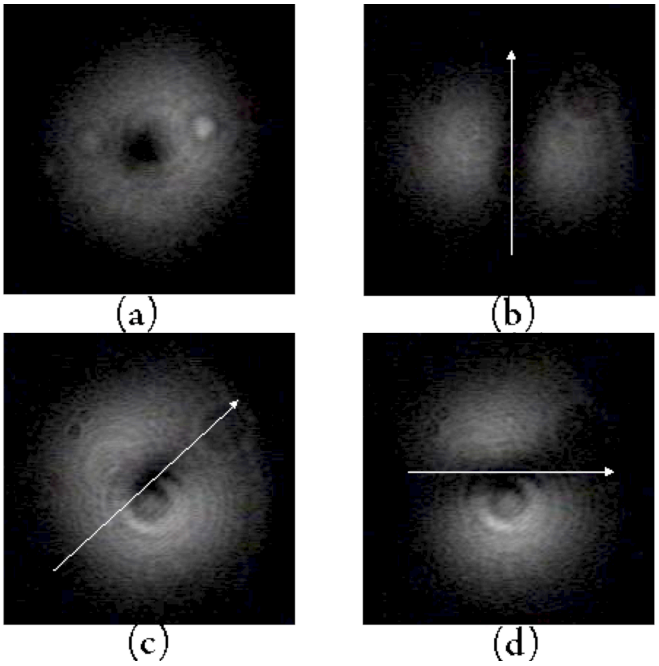

Figure 6.4: Black and white CCD image of the intensity structure of (a) the hybrid-azimuthal polarization beam with an input polarization of 45^o and analyzer at (b) 0^o, (c) 45^o, and (d) 90^o. The white arrow shows the direction of the linear polarizer.

coupled into the fiber with a spin rate of 20 turns per meter, the clear optical vortex with the HAPi state is seen.

This particular HAPi state is shown pictorially in Fig. 6.5(a). Parts (b) - (d) of this figure show the effect a linear polarizer oriented at 0^o, 45^o, and 90^o has on the polarization state shown. The shaded area in parts (a) - (d) represent the intensity distribution, while the arrows denote the polarization state in that region.

The cylindrical vector beam shown and described in Figs. 6.4 and 6.5 is the experimental observation of the hybrid-azimuthal polarization with circular polarization states every 90^o around the beam profile. This beam can be transformed into a pure azimuthal polarization state by inserting a quarter-wave plate oriented at 0^o or 90^o. This will transform the regions of circular polarization into linear polarization states oriented at 45^o or 135^o depending on the handedness of the circular polarization and not affect the linear polarization states. This beam can be converted further to a pure radially polarized mode by inserting a half-wave plate oriented at 45^o. An example of this conversion process is shown in Fig. 6.6.

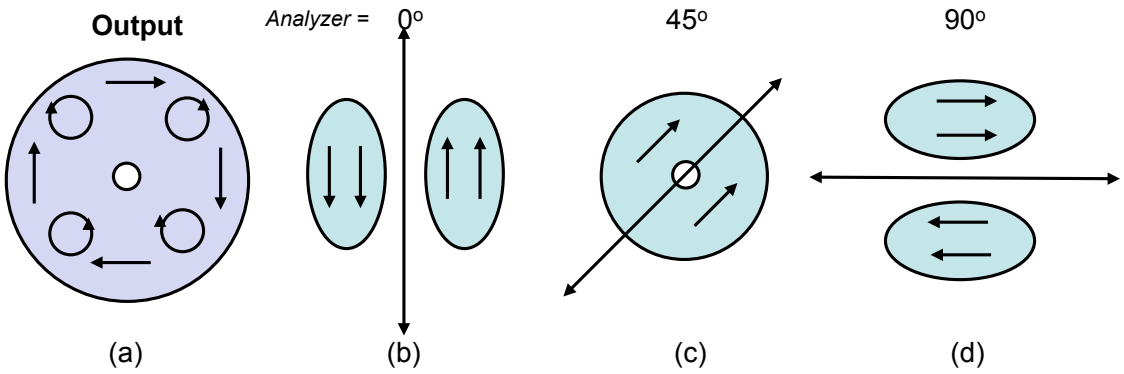

Figure 6.5: (a) Pictorial representation of the output polarization state from twisted fiber and spatial profile after analyzer for (b) 0^o, (c) 45^o, and (d) 90^o.

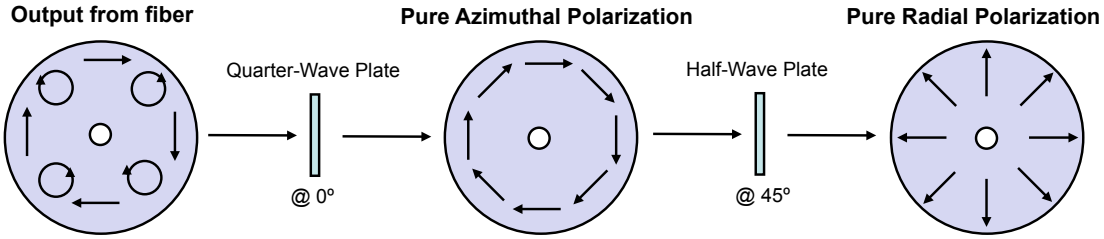

Figure 6.6: Pictorial representation of converting the output polarization state from twisted fiber into a pure azimuthally polarized beam then into a pure radially polarized beam.

Figure 6.7 shows the experimental CCD images of the hybrid-azimuthal polarized beam converted to a pure azimuthally polarized beam. A linear polarizer oriented at (a) 0^o, (b) 45^o, (c) 90^o, (d) 135^o, and (e) 180^o is used as an analyzer and the white arrow in the figure represents the direction of the polarization. When the analyzer is not used an optical vortex is seen identical to Figure 6.4 (a) with a polarization identical to the azimuthal polarization shown in Figure 6.1 (b).

6.5 Conclusions

In conclusion, this chapter discusses a new hybrid-azimuthal polarization and its' associated angular momentum. The angular momentum density is spatially varying

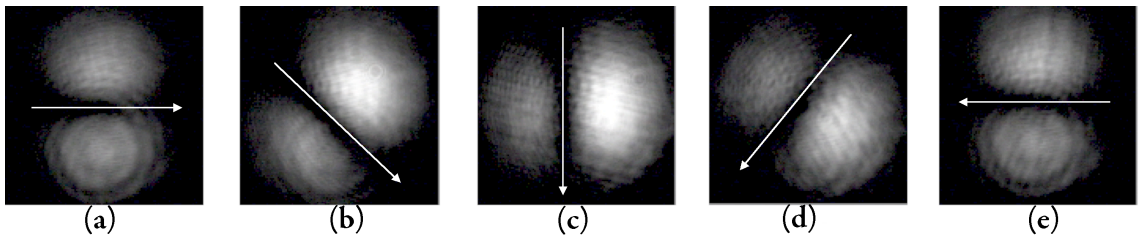

Figure 6.7: Hybrid-azimuthal polarization converted to a pure azimuthal polarization after passed through a linear polarizer oriented at (a) 0^o, (b) 45^o, (c) 90^o, (d) 135^o, and (e) 180^o. The white arrows represent the direction of polarization.

around the beam which is believed to be a *new* phenomenon. The first generation of this new class of vortex beam is demonstrated by propagating a fundamental laser mode through a spun optical fiber. A dependence on the spin rate shows that the conversion to the hybrid-azimuthal polarization is facilitated by a spatially varying index of refraction in the fiber. We characterized the polarization state of the output from the fiber and discussed the process of this mode conversion.

The HAPi state has many potential applications due to the fact that in one beam of light there exists every polarization state: vertical, horizontal, left-circular, and right-circular polarizations. This spatially varying polarization could be useful for imaging, optical trapping, and optical communications.

Chapter 7

Optical Airy Beams

7.1 Introduction

There has been a lot of attention paid to various interesting, non-trivial solutions to the paraxial wave equation. Some of these beams exhibit interesting features such as spin or orbital angular momentum[76], diffraction-free propagation [77], self reconstruction [78], or acceleration. Depending on the coordinate system there are Hermite, Laguerre, Bessel, and Ince-Gaussian solutions to name just a few. Most recently there has been increasing attention paid to the Airy solution of the paraxial wave equation first described by Berry and Balazs in 1979 [79]. The observation of this solution was first in the context of the Schrödinger equation describing a free particle. The 1-D and 2-D Airy solution was most recently shown experimentally by Siviloglou et. al. in optical beams of light [80]. The Airy beam is said to be free of diffractive spreading and freely accelerating in the absence of any external potential [82].

In this chapter the Poynting vector and angular momentum of the Airy beam as it propagates through space is investigated. First, classical electrodynamics will be used to numerically calculate the Poynting vector of the airy wave packet. Next, two methods are employed to analyze the angular momentum of the Airy beam. The first is calculating $\vec{j} = \vec{r} \times \vec{p}$ while the second is calculating the angular momentum spectrum of this beam of light [83]. These methods provide complimentary information and insight as to how this beam travels through space.

7.2 Airy solution to the wave equation

The (2 + 1)D paraxial wave equation describes the wave propagation of the electric field ϕ as,

$$2i\frac{\partial u(s_x, s_y, \xi)}{\partial \xi} + \nabla_\tau^2 u(s_x, s_y, \xi) = 0 \tag{7.1}$$

where $s_x = x/x_0$ and $s_y = y/y_0$ are normalized transverse coordinates, $\xi = z/k(x_0 + y_0)$ is a normalized propagation distance, x_0 and y_0 are normalization constants, $k = 2\pi n/\lambda_0$ and ∇_τ^2 is the second partial derivative in the transverse direction.

The non-dispersive solution to this (2+1)D equation is,

$$u(s_x, s_y, \xi) = Ai\left(s_x - (\xi/2)^2\right) Ai\left(s_y - (\xi/2)^2\right) \exp\left[i(s_x\xi/2 + s_y\xi/2) - i(\xi^3/12)\right], \tag{7.2}$$

where $Ai(x)$ is the Airy function and is shown in the inset at the center of Fig. 7.1. This type of beam can be produced experimentally with a specially designed diffraction grating [80].

In theory a non-dispersive beam of this sort would have infinite power. However in practice, this can not be the case because a beam can not propagate infinite power. As discussed in Refs. [80, 81], to experimentally realize the Airy beam an initial condition must be employed to act as an exponential aperture function. Taking this initial condition as, $u(s_x, s_y, 0) = Ai(s_x)Ai(s_y)\exp\Big[a(s_x + s_y)\Big]$, where $a << 1$ and is a positive parameter that limits the infinite energy in the Airy tail, the electric field amplitude becomes

$$\begin{aligned} u(s_x, s_y, \xi) &= Ai\left(s_x - (\xi/2)^2 + ia\xi\right) Ai\left(s_y - (\xi/2)^2 + ia\xi\right) \exp\left[as_x + as_y\right] \times \\ &\quad \exp\Big[-(a\xi^2/2) - i(\xi^3/12) - i(a^2\xi/2) + i\xi(s_x + s_y)/2\Big]. \end{aligned} \tag{7.3}$$

Figure 7.1(a-d) shows the intensity in the transverse plane at various ξ-positions when $a = 0.15$ and $x_o = y_o = 0.1$. All of the intensity peaks are changing position as ξ increases. The main intensity peak in the $s_x - s_y$ plane of the Airy beam travels at 45^o, along the line $s_x = s_y$, following the trajectories,

$$x_m = \frac{\lambda_o^2 \xi^2}{16\pi^2 x_o^2} \quad and \quad y_m = \frac{\lambda_o^2 \xi^2}{16\pi^2 y_o^2}. \tag{7.4}$$

7.3 Airy's Poynting Vector

The rate of electromagnetic energy flow per unit area, or the Poynting vector, is a commonly known quantity in electrodynamics [84, 85]. This vector is routinely examined for plane waves but has received considerable attention in the literature with regard to Laguerre-Gaussian beams of light that have helical wavefronts [76, 86, 87].

The Poynting vector is defined as [85]:

$$\vec{S} = (c/4\pi)\vec{E} \times \vec{B}, \tag{7.5}$$

where c is the speed of light. Given a vector potential $\vec{A} = \hat{\epsilon}u(s_x, s_y, \xi)\exp\left[ik^2\xi(x_0 + y_0)\right]$, where $\hat{\epsilon}$ is an arbitrary polarization and $u(s_x, s_y, \xi)$ is the Airy field amplitude given by Eq. (7.3), we can use the $\vec{E}$ and $\vec{B}$-fields in the Lorenz gauge, as given by Ref. [76] and shown in Eqs. 1.29 and 1.30, to calculate the time-averaged Poynting vector,

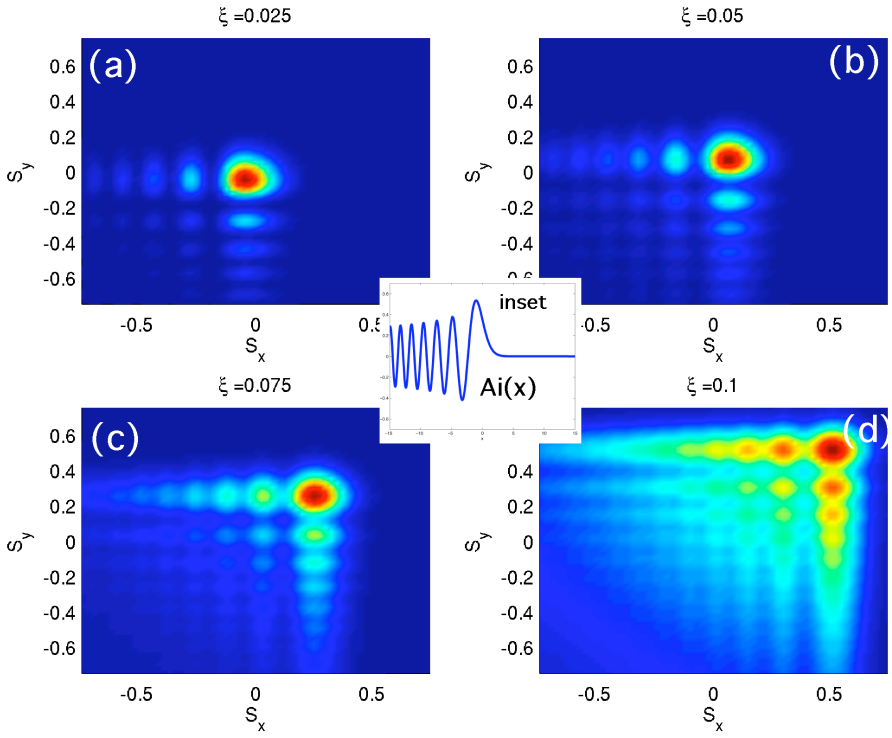

Figure 7.1: The intensity of the finite-energy Airy wave in the $s_x - s_y$ plane, given by eq. (7.3) with $a = 0.15$ at $\xi = 0.025$ (a), $\xi = 0.05$ (b), $\xi = 0.075$ (c), $\xi = 0.1$ (d). The inset shows the behavior of Ai(x).

$< \vec{S} >$. Assuming an $\hat{x}$-polarized field (really $\hat{s_x}$-polarized in this new notation), $< \vec{S} >$ becomes [76]

$$\begin{aligned} \frac{c}{4\pi} < \vec{E} \times \vec{B} > &= \frac{c}{8\pi}\left(\vec{E} \times \vec{B}^* + \vec{E}^* \times \vec{B}\right) \\ &= \frac{c}{8\pi}\left[i\omega(u\nabla_\tau u^* - u^*\nabla_\tau u) + 2\omega k|u|^2\hat{\xi}\right]. \end{aligned} \tag{7.6}$$

The $\hat{\xi}$ term in the above equation is the energy flow in the $\hat{\xi}$-direction which is just proportional to the linear momentum density in that direction. This is typically the main contributing component of $\vec{S}$ in Gaussian optics. The first term is what we are really interested in here as it contributes a non-zero $\hat{s}_x$- and $\hat{s}_y$-component and an additional $\hat{\xi}$-term to the Poynting vector.

Figure 7.2 (a-d) shows the numerically computed $\hat{s}_x$- and $\hat{s}_y$-components of the Poynting vector for $a = 0.15$ at $\xi = 0.025$, 0.050, 0.075, and 0.1, respectively. The direction and magnitude of the arrows (shown in red) correspond to the direction and

magnitude of the energy flow in the transverse plane. The intensity of the Airy field is shown in the background of each frame to show the direction of the energy flow in relation to the peaks of the Airy beam. The flow of energy of the main peak at $\xi > 0$ is consistently pointed at 45^o relative to the $s_x - s_y$ plane at all ξ-locations. In contrast, the direction of the energy flow for the Airy tails, or the peaks oriented along the horizontal or vertical axis approaches a direction perpendicular to that axis. The **net** energy flow is measured, however, to be constant and pointed in the direction that the main peak moves, i.e 45^o or along the line $s_x = s_y$.

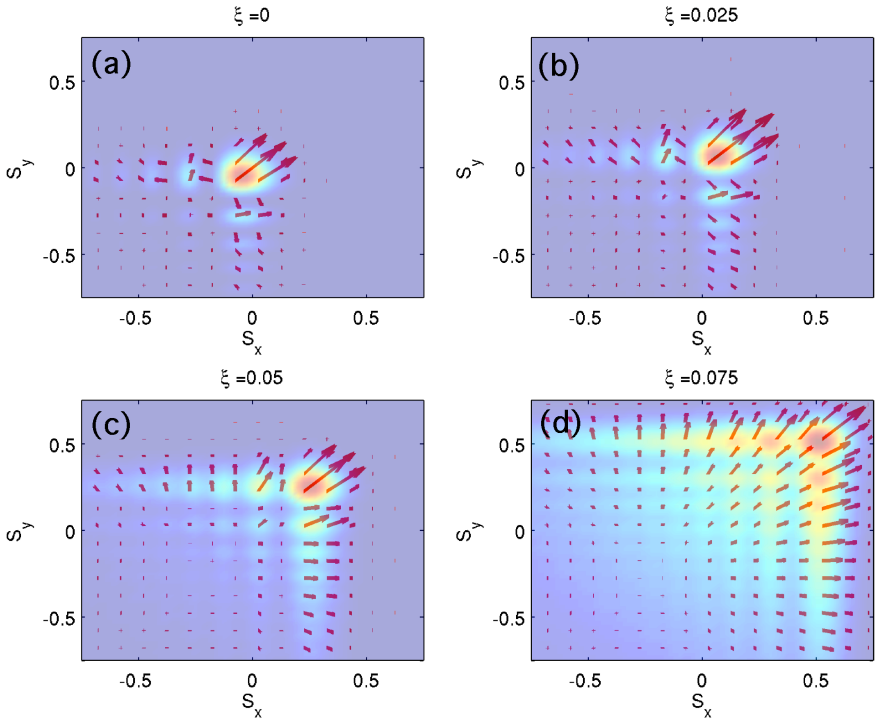

Figure 7.2: The numerically calculated Poynting vector in the $s_x - s_y$ plane, of the finite-energy Airy wave given by eq. (7.6) with a = 0.15 at $\xi = 0$ (a), $\xi = 0.025$ (b), $\xi = 0.050$ (c), $\xi = 0.075$ (d). The intensity of the Airy field is shown in the background of each frame.

It is interesting to note that in (a) of Fig. 7.2, the Poynting vector is initially pointing in the negative s_x or negative s_y-direction on each Airy tail; in (b) of the figure the direction starts to turn partially towards the direction of the energy flow of the main Airy peak (45^o); and in (c) and (d) as the beam propagates further, the

direction swings around even more towards 45^o. This change in the Poynting vector can be interpreted as explaining why the optical Airy beam is said to be accelerating since $\vec{S} \propto \vec{p}$ and a change in $\vec{p}$ would lead to a non-zero acceleration.

7.4 Angular Momentum of the Airy Beam

It is well known that as $\vec{p} \propto \vec{E} \times \vec{B}$ from which follows that angular momentum density about the $\hat{\xi}$-direction is

$$\begin{aligned} j_\xi(s_x, s_y, \xi) &= \vec{r} \times \left\langle \vec{E} \times \vec{B} \right\rangle_\xi \\ &= s_x \cdot S_{s_y} + s_y \cdot S_{s_x}. \end{aligned} \tag{7.7}$$

The numerically computed $< \vec{S} >$ taken from Eq. 7.6 and shown in Fig. 7.2 is used to calculate the angular momentum in the $\hat{\xi}$-direction. Figure 7.3 (a-d) shows the $\hat{\xi}$-component of the angular momentum density with $a = 0.15$ at $\xi = 0.025$, 0.050, 0.075, and 0.100, respectively. At $\xi = 0$ the computed angular momentum is zero so it is not shown. In Fig. 7.3 reds are positive values (clockwise), blues are negative values (counter-clockwise), and green is zero. The non-discrete nature of these values will be discussed in the next section.

As the beam propagates, the **net** angular momentum in the ξ-direction is always zero. The spatial distribution of the angular momentum is changing however, and locally has non-zero values of angular momentum. Not only is the angular momentum changing in the Airy tails, but there are also changes to the angular momentum in the main Airy peak. This change of angular momentum is a torque that corresponds to the force present due to the changing linear momentum.

7.5 Angular Momentum Spectrum of Airy Beams

Recently a new type of imaging was proposed that is based on the phase and spatial profile of the wavefront and is coined *spiral imaging*[83]. This spiral imaging is similar to what Ref. [88] refers to as the orbital angular momentum (OAM) spectrum of a beam of light that they show experimentally. One can use this technique to get a more complete picture of what the zero **net** angular momentum density with local non-discrete, non-zero values means.

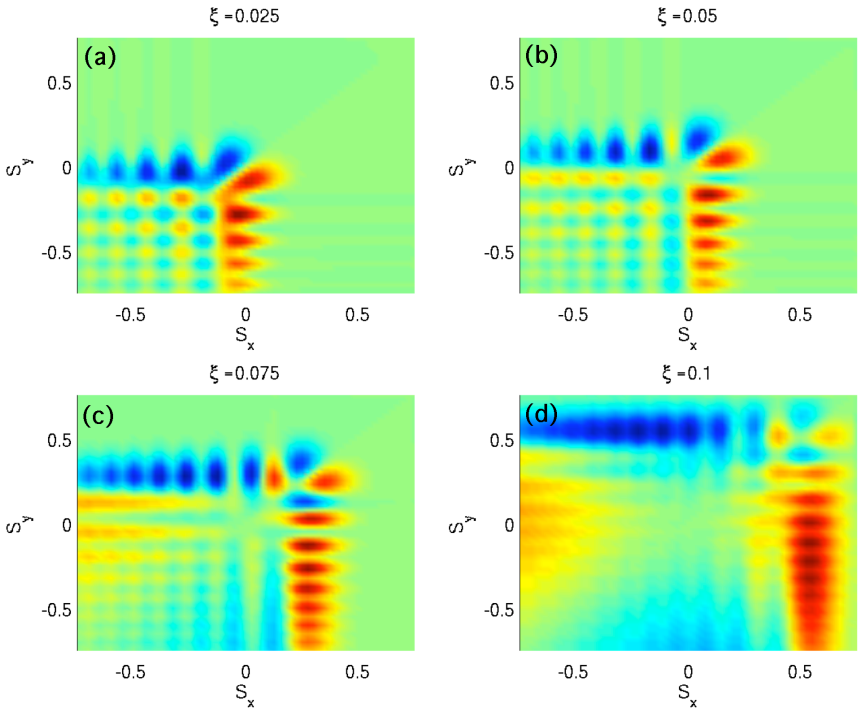

Figure 7.3: The numerically calculated angular momentum in the $\hat{\xi}$-direction of the finite-energy Airy wave given by eq. (7.7) with a = 0.15 at $\xi = 0.025$ (a), $\xi = 0.050$ (b), $\xi = 0.075$ (c), $\xi = 0.100$ (d). Reds are positive values, blues are negative values, and green is zero.

Any optical beam can be decomposed into a superposition of angular harmonics in cylindrical coordinates written as

$$u(r, \phi; z) = \frac{1}{\sqrt{2\pi}} \sum_m a_m(r, z) \exp(im\phi), \tag{7.8}$$

where $a_m(r, z) = 1/(2\pi)^{1/2} \int_0^{2\pi} u(r, \phi, z) \exp(-im\phi) d\phi$ and the energy of each mode, m, is described by $C_m = \int_0^\infty |a_m(r, \phi, z)|^2 r dr$. The power, or weight, of each angular momentum state for the arbitrary field u is given by[83]

$$P_m = \frac{C_m}{\sum_{-\infty}^{\infty} C_n}. \tag{7.9}$$

Figure 7.4(a-f) shows the angular momentum spectrum of the Airy beam where the field, u, is taken from Eq. 7.3, i.e. the weight of each spiral mode when the field

is decomposed in these spiral harmonics, for ξ ranging from 0 to 0.125. Note that the sum of all of the weights of the modes at each ξ location is one and the net angular momentum is zero.

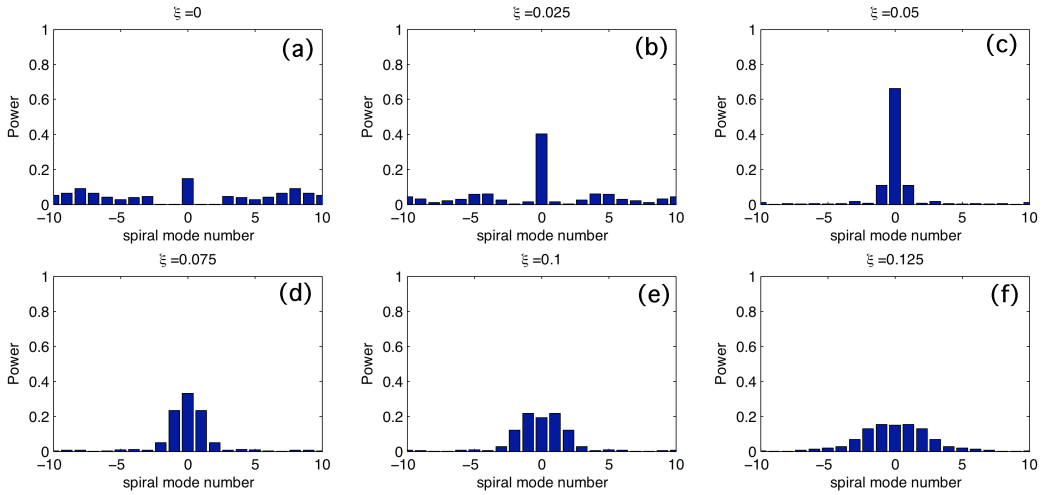

Figure 7.4: The angular momentum spectrum of the finite-energy Airy wave given by eqs. (7.8, 7.9) with a = 0.15 at $\xi = 0$ (a), $\xi = 0.025$ (b), $\xi = 0.05$ (c), $\xi = 0.075$ (d), $\xi = 0.100$ (e), and $\xi = 0.125$ (f).

The angular momentum, J_ξ, is shown to have non-discrete, non-integer values (positive and negative). Fig. 7.4 shows that this Airy field, *locally*, has an integer sum of discrete values of orbital angular momentum while the *total* angular momentum is in fact zero.

7.6 Conclusions

This chapter analyzes the spatial evolution of the Airy solution to the paraxial wave equation and shows that while momentum is changing, energy and momentum are conserved. The linear and angular momenta are shown to be changing as the Airy beam propagates in the ξ-direction which should have implications when analyzing the velocity of this field. Some form of the velocity, be it phase, energy, or signal velocity, should be changing as the beam propagates and should be investigated in future studies. These beams have promise for applications in optical trapping, imaging, and

spectroscopy where a sample might interact with a changing momentum and spatially varying angular momentum.

Chapter 8

Outlook, Conclusions, and Future Work

This thesis discusses the use and generation of optical vortices for applications in imaging and spectroscopy. The topics discussed here just touch the surface in these areas. This chapter focusses on directions for future research in relation to imaging and spectroscopy using optical vortices that can carry orbital angular momentum.

8.1 Optical vortices in light-matter interaction

8.1.1 Spectroscopy of quantum dots with light carrying orbital angular momentum

Chapter 4 discusses the generation of coherent white light optical vortices from supercontinuum. Each spectral component of this broadband light has a discrete amount of orbital angular momentum, $l\hbar$. Never before has this been available for use in spectroscopic applications. Figure 8.1 shows a white optical vortex, generated in the method shown in Chapter 4, and passed through a sample whose spectra is measured using a spectrometer. As an example, a white light LG supercontinuum beam is passed through a interference band-pass filter which is shown in Figure 8.1.

Spectra can be taken for beams of light with various l-values. Different l-values should have different transmission or absorption spectra because absorption line correspond to differences between energy levels and selection rules for S, L, and J. Absorption spectra has shown a dependence on the polarization state used, i.e. spin state, and should do the same with orbital angular momentum states of light.

Quantum dots seem particularly suitable for investigating light-matter interactions with beams of light with orbital angular momentum because of their well defined, discrete energy levels.

8.1.2 Raman spectroscopy with optical vortices

Raman spectroscopy is a technique used to study the vibrational, torsional, and rotational modes of molecules. When light is incident upon a molecule there can be a collision between the light and the molecule. If we observe an inelastic collision, where the vibrational energy of the molecule is changed, the scattered light has a slightly higher or lower in energy in order for the total energy of the collision to be conserved. This is the premise of the Raman effect and is the process involved in

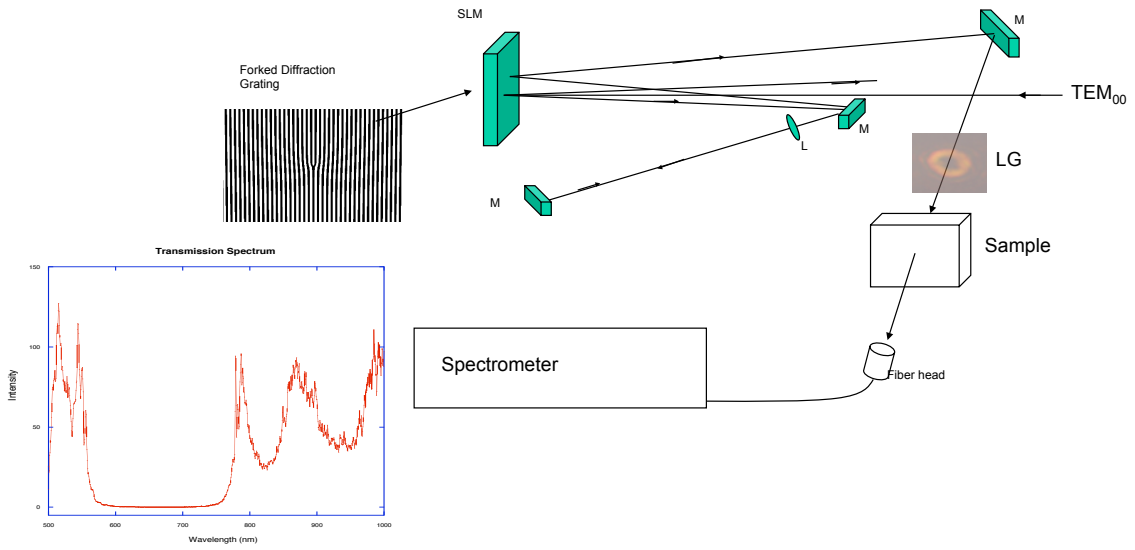

Figure 8.1: A white light optical vortex is generated and passed through a sample. The light transmitted through the sample is collected with a spectrometer and the spectrum is observed for different angular momentum states. The spectrum of an optical vortex that passes through an interference bandpass filter is shown as an example.

observing frequencies higher (anti-Stokes) or lower (Stokes) than the light incident on the molecule.

Traditionally, light incident on a sample comes in the form of either linearly or circularly polarized beams of light. These conventional fields are transverse modes with no longitudinal component. This section will examine what happens to the Raman spectrum if the incident light is a tightly focussed radially polarized beam of light that has a longitudinal component to the electric field.

For a fundamental vibrational frequency to appear in the Raman spectrum the amplitude of the dipole moment induced by the incident radiation must change during the vibration considered. The induced dipole moment is given by,

$$\vec{P} = \alpha \cdot \vec{E}, \tag{8.1}$$

where $\vec{E}$ is the incident electric field vector and α is the polarizability tensor of the molecule. The three components of the induced dipole moment are written explicitly as,

$$P_x = \alpha_{xx}E_x + \alpha_{xy}E_y + \alpha_{xz}E_z \tag{8.2}$$

$$P_y = \alpha_{yx}E_x + \alpha_{yy}E_y + \alpha_{yz}E_z \tag{8.3}$$

$$P_z = \alpha_{zx}E_x + \alpha_{zy}E_y + \alpha_{zz}E_z. \tag{8.4}$$

Every one of the nine components of the polarizability tensor change when the nuclei are displaced from their equilibrium positions. For small displacements the components can be expanded as,

$$\alpha_{xx} = \alpha^0_{xx} + \sum_k \Big[\Big(\frac{\partial\alpha_{xx}}{\partial x_k}\Big)_0 x_k + \Big(\frac{\partial\alpha_{xx}}{\partial y_k}\Big)_0 y_k + \Big(\frac{\partial\alpha_{xx}}{\partial z_k}\Big)_0 z_k\Big] + \cdots \tag{8.5}$$

where similar relations hold for the rest of the components. Upon changing to normal coordinates and inserting an electric field,

$$E_x = E^0_x \cos 2\pi\nu t \quad E_y = E^0_y \cos 2\pi\nu t \quad E_z = E^0_z \cos 2\pi\nu t, \tag{8.6}$$

we get the relation,

$$\begin{aligned} P_x = {} & \Big(\alpha^0_{xx}E^0_x + \alpha^0_{xy}E^0_y + \alpha^0_{xz}E^0_z\Big)\cos 2\pi\nu t \\ & + \sum_\imath \Big[\Big(\frac{\partial\alpha_{xx}}{\partial\xi_\imath}\Big)_0 E^0_x + \Big(\frac{\partial\alpha_{xy}}{\partial\xi_\imath}\Big)_0 E^0_y + \Big(\frac{\partial\alpha_{xz}}{\partial\xi_\imath}\Big)_0 E^0_z\Big]\xi^0_\imath \\ & \times[\cos 2\pi(\nu+\nu_i)t + \cos 2\pi(\nu-\nu_i)t] \end{aligned} \tag{8.7}$$

where similar relations hold for P_y and P_z. The first term in the above equation is the Rayleigh term as it is radiating the same frequency as the initial radiation. The second term is the Raman term with a Stokes $(\nu+\nu_i)$ and anti-Stoke $(\nu-\nu_i)$ frequency.

A normal mode of vibration will appear in the Raman spectrum if at least one of the components of the change of polarizability are non zero, i.e.

$$\Big(\frac{\partial\alpha_{xx}}{\partial\xi_\imath}\Big)_0, \Big(\frac{\partial\alpha_{xy}}{\partial\xi_\imath}\Big)_0, \Big(\frac{\partial\alpha_{xz}}{\partial\xi_\imath}\Big)_0, \cdots \neq 0. \tag{8.8}$$

This is the classical origin of the normal modes of vibration in the Raman spectra of molecules.

A conventional Raman spectroscopy system consists of a monochromatic light source, sample, collection optics, a monochromater, and a CCD or photo-multiplier tube. The typical light source for such a system is a Gaussian laser in its fundamental mode with an electric field given by,

$$\vec{E}(x,y,z) = \hat{e}E_0 \exp\Big[-(x^2+y^2)/w^2\Big] \times \exp\Big[-\imath(kz-\omega t)\Big]. \tag{8.9}$$

This field describes a Gaussian wavefront traveling in the z-direction, with a beam wast w, an amplitude of E_0, and a polarization vector $\hat{e}$. Light of this nature has either linear polarization, e.g. $\hat{e} = \hat{x}$, or circular polarization, $\hat{e} = x \hat{\pm} \imath y$. In either case the polarization is limited to the transverse direction and there is no component of the electric field in the z-direction. In light of the fact this is a transverse field, i.e. $E_z = 0$, we can therefore see that

$$\begin{aligned} P_x &= \left(\alpha^0_{xx} E^0_x + \alpha^0_{xy} E^0_y\right) \cos 2\pi\nu t \\ &\quad + \sum_\imath \left[\left(\frac{\partial \alpha_{xx}}{\partial \xi_\imath}\right)_0 E^0_x + \left(\frac{\partial \alpha_{xy}}{\partial \xi_\imath}\right)_0 E^0_y\right] \xi^0_\imath \\ &\quad \times [\cos 2\pi(\nu + \nu_i)t + \cos 2\pi(\nu - \nu_i)t], \end{aligned} \tag{8.10}$$

with similar expressions for $P_{y,z}$. Equation 8.10 shows there is no information obtained about $\alpha_{xz,yz,zz}$ due to the absence of a z-component to the electric field.

If the electric field incident upon a scattering molecule is a longitudinal mode, i.e. has a z-component, a complete picture of the polarizability and the molecules structure can be obtained. One type of electric field that has an x-, y-, and z-component is a tightly focussed radially polarized beam of light which has a polarization vector given by,

$$\hat{e} = x\hat{x} + y\hat{y} = \hat{r}. \tag{8.11}$$

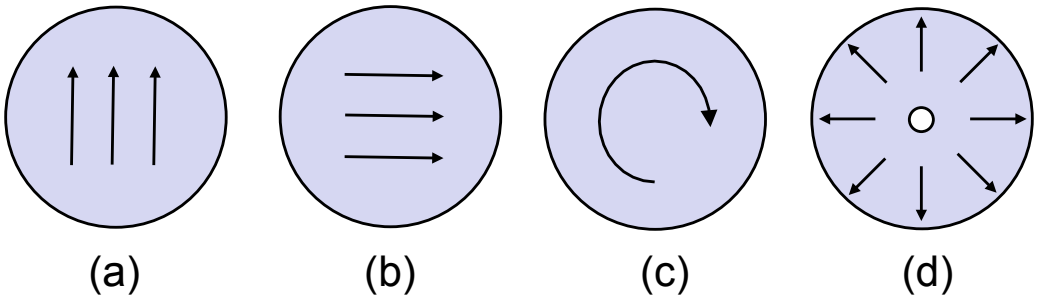

Figure 8.2: Examples of (a) vertical, (b) horizontal, (c) circular, and (d) radial polarization.

Fig. 8.2(d) shows vectorially what a radially polarized wave looks like compared to linear and circular polarization (a-c). There are several methods for generating radially polarized fields, that when tightly focussed have longitudinal components.

Regardless of the method the final induced dipole moment of the molecule in the presence of the electric field will include the z-component terms, which it does not with conventional linear or circular polarization.

With a tightly focussed radially polarized beam incident on a molecule, the Raman term of the induced dipole moment in the x-direction is given by,

$$\begin{aligned} P_x^{Raman} &= \sum_\imath \Big[\Big(\frac{\partial\alpha_{xx}}{\partial\xi_\imath}\Big)_0 E_x^0 + \Big(\frac{\partial\alpha_{xy}}{\partial\xi_\imath}\Big)_0 E_y^0 + \Big(\frac{\partial\alpha_{xz}}{\partial\xi_\imath}\Big)_0 E_z^0\Big]\xi_\imath^0 \\ &\quad \times[\cos 2\pi(\nu+\nu_i)t + \cos 2\pi(\nu-\nu_i)t], \end{aligned} \tag{8.12}$$

with similar expressions for $P_{y,z}^{Raman}$. The added E_z term when in the presence of a longitudinal field can increase the strength of vibrational modes as well as allow for the presence of previously unseen vibrational modes.

8.2 Optical imaging with Airy beams

Chapter 7 discussed the propagation dynamics and angular momentum of accelerating optical Airy beams. This new class of beam was shown to bend in the transverse plane is it propagates. The bend in the Airy beams propagation can be exploited for applications in imaging and signal propagation. Figure 8.3 shows how an object that is hidden behind a second object can not be seen by (a) a Gaussian beam while it can by (b) an Airy beam.

Most recently, the self-healing properties of Airy beams has been investigated [1]. Figure 8.4, reprinted from Broky *et. al.*, shows the self-healing property of an Airy beam. The main lobe of the Airy beam is blocked at $z = 0$ (a) and observed reforming at $z = 11cm$ (b) and by $z = 30cm$ (c) it has totally reformed. This self-healing is thought to occur due to the energy flowing from the tail of the Airy beam into the region blocked.

The self-healing property of the optical Airy beam can be used to image in adverse environments. Figure 8.5 (a) shows a scheme where an image is embedded in the main Airy lobe, an "H" in this case. This can be accomplished by using a beam with an image embedded in it to generate the Airy beam by using a spatial light modulator with a cubic phase profile. Figure 8.5 (b) shows the main lobe blocked

[1] J. Broky, G. A. Siviloglou, A. Dogariu, and D. N. Christodoulides, "Self-healing properties of optical Airy beams," Opt. Express 16, 12880-12891 (2008).

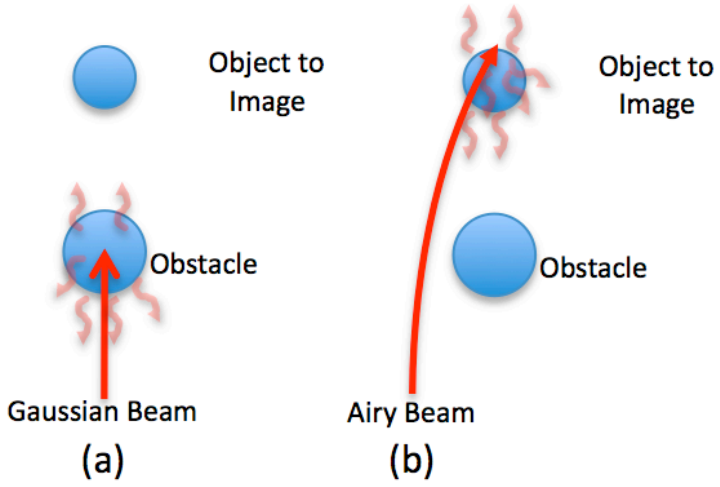

Figure 8.3: Attempting to image an object behind another with (a) a Gaussian beam is not possible. (b) If an Airy beam is used the object hidden behind another can be seen and detected.

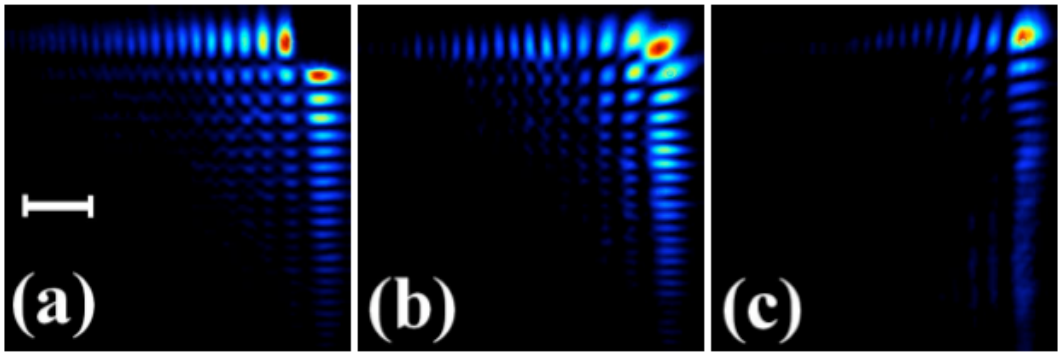

Figure 8.4: Self healing property of an Airy beam shown experimentally by blocking the main lobe of the Airy beam at $z = 0$ (a) and observing it reform at $z = 11cm$ (b) and $z = 30cm$ (c). Reprinted from (J. Broky, G. A. Siviloglou, A. Dogariu, and D. N. Christodoulides, "Self-healing properties of optical Airy beams," Opt. Express 16, 12880-12891 (2008))

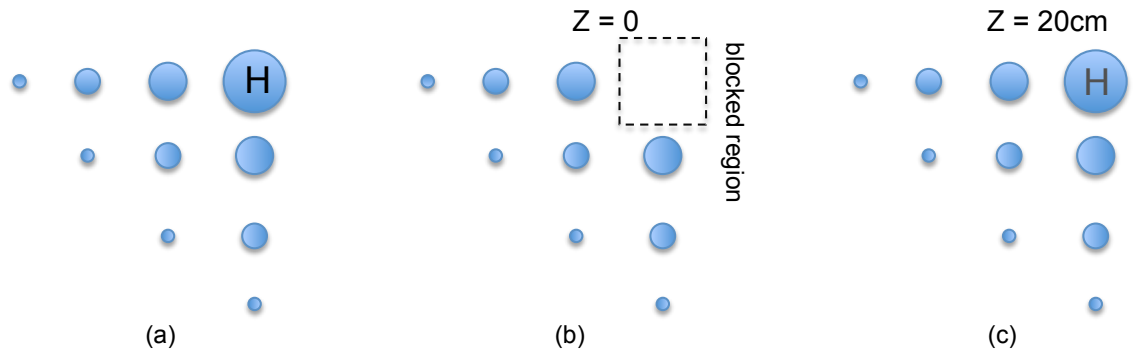

Figure 8.5: Scheme to use an Airy beam to pass information through a scattering medium even when the intensity maximum of the beam is blocked by an obstacle. The letter "H" is embedded in the main Airy lobe (a). The main lobe is blocked (b) but can recontruct itself and the image of the "H" at a further propagation distance (c).

by some obstacle in a medium corresponding to a propagation distance $z = 0$. Due to the energy flow in the Airy beam the main Airy lobe will reconstruct itself as in Figure 8.4 (c). Now, however, the image, the letter "H" is contained in the energy of the Airy tails and should reconstruct itself upon further travel, a distance $z = 20$ as an example, shown in Figure 8.5 (c). This image reconstruction would definitely not occur if a Gaussian beam were used because the self-healing is a property of so-called "diffractionless" beams. Another such beam that this might work is the Bessel beam.

Appendix A

Computer Program to Generate Binary Forked Diffraction Gratings

The following Matlab code generates a binary diffraction grating with charge L and displays it as a figure in a new window. The variable `n` determines the size of the array.

```
clear all;
n = 2^10;   % Size of the array
mask = zeros(n); % Sets the mask as an array of all zeros initially

I = 1:n; % Setup size of array
x = I-n/2;
y = n/2-I;
[X,Y] = meshgrid(x,y); % Initiate cartesian coordinates
theta = arctan2(X,Y); % Transforming to polar coordinates
r  = sqrt(x.^2 + y.^2);   %

D = 2*pi;
K = 0.11.*2*pi/D; % Grating Constant
L = 1;  % Sets the value of  'L'

% This is where the magic happens.  'A' is the grating function
A = (((L.*theta)./1) - K.*X) >= 0;
% If 'A' is greater than zero then it the (X,Y) location in the array is set to 1
mask(A) = 1;

figure % Initializes a figure
imagesc(real(mask)) % Displays the mask as an image in the figure
colormap(gray) % Sets the color to grayscale
axis off % Turns the axis display off
```

Computer Program to Generate Blazed Forked Diffraction Gratings

The following Matlab code generates a blazd diffraction grating with charge L and displays it as a figure in a new window. The variable `n` determines the size of the array.

```
clear all;
n = 2^10;   % Size of the array
mask = zeros(n); % Sets the mask as an array of all zeros initially

I = 1:n; % Setup size of array
x = I-n/2;
y = n/2-I;
[X,Y] = meshgrid(x,y); % Initiate cartesian coordinates
theta = arctan2(X,Y); % Transforming to polar coordinates
r  = sqrt(x.^2 + y.^2);   %

D = 2*pi;
K = 0.11.*2*pi/D; % Grating Constant
L = 1;  % Sets the value of  'L'

% This is where the magic happens.'A' is the grating function
A = (((L.*theta)./1) - K.*X);
% This gives the mask the blazed appearance due to the modulo function
mask = (1/sqrt(2)).*exp(-i.*0.3.*mod(A,2*pi));

figure
imagesc(real(mask))
colormap(gray)
axis off
```

GratingUI Program to Generate Diffraction Gratings

```
function varargout = GratingUI(varargin)
```

```
% GRATINGUI M-file for GratingUI.fig
%      GRATINGUI, by itself, creates a new GRATINGUI or raises the existing
%      singleton*.
%
%      H = GRATINGUI returns the handle to a new GRATINGUI or the handle to
%      the existing singleton*.
%
%      GRATINGUI('CALLBACK',hObject,eventData,handles,...) calls the local
%      function named CALLBACK in GRATINGUI.M with the given input arguments.
%
%      GRATINGUI('Property','Value',...) creates a new GRATINGUI or raises the
%      existing singleton*.  Starting from the left, property value pairs are
%      applied to the GUI before GratingUI_OpeningFunction gets called.  An
%      unrecognized property name or invalid value makes property application
%      stop.  All inputs are passed to GratingUI_OpeningFcn via varargin.
%
%      *See GUI Options on GUIDE's Tools file.  Choose "GUI allows only one
%      instance to run (singleton)".
%
% See also: GUIDE, GUIDATA, GUIHANDLES

% Edit the above text to modify the response to help GratingUI

% Last Modified by GUIDE v2.5 24-Apr-2006 14:43:24

% Begin initialization code - DO NOT EDIT
gui_Singleton = 1;
gui_State = struct('gui_Name',       mfilename, ...
                   'gui_Singleton',  gui_Singleton, ...
                   'gui_OpeningFcn', @GratingUI_OpeningFcn, ...
                   'gui_OutputFcn',  @GratingUI_OutputFcn, ...
                   'gui_LayoutFcn',  [] , ...
                   'gui_Callback',   []);
if nargin && ischar(varargin{1})
```

```
    gui_State.gui_Callback = str2func(varargin{1});
end

if nargout
    [varargout{1:nargout}] = gui_mainfcn(gui_State, varargin{:});
else
    gui_mainfcn(gui_State, varargin{:});
end
% End initialization code - DO NOT EDIT


% --- Executes just before GratingUI is made visible.
function GratingUI_OpeningFcn(hObject, eventdata, handles, varargin)
% This function has no output args, see OutputFcn.
% hObject    handle to figure
% eventdata  reserved - to be defined in a future version of MATLAB
% handles    structure with handles and user data (see GUIDATA)
% varargin   command line arguments to GratingUI (see VARARGIN)

% Choose default command line output for GratingUI
handles.output = hObject;

% Update handles structure
guidata(hObject, handles);

% UIWAIT makes GratingUI wait for user response (see UIRESUME)
% uiwait(handles.figure1);


% --- Outputs from this function are returned to the command line.
function varargout = GratingUI_OutputFcn(hObject, eventdata, handles)
% varargout  cell array for returning output args (see VARARGOUT);
% hObject    handle to figure
% eventdata  reserved - to be defined in a future version of MATLAB
```

```
% handles    structure with handles and user data (see GUIDATA)

% Get default command line output from handles structure
varargout{1} = handles.output;


% --- Executes on button press in radiobutton1.
function radiobutton1_Callback(hObject, eventdata, handles)
% hObject    handle to radiobutton1 (see GCBO)
% eventdata  reserved - to be defined in a future version of MATLAB
% handles    structure with handles and user data (see GUIDATA)

% Hint: get(hObject,'Value') returns toggle state of radiobutton1


% --- Executes on button press in radiobutton2.
function radiobutton2_Callback(hObject, eventdata, handles)
% hObject    handle to radiobutton2 (see GCBO)
% eventdata  reserved - to be defined in a future version of MATLAB
% handles    structure with handles and user data (see GUIDATA)

% Hint: get(hObject,'Value') returns toggle state of radiobutton2


function edit1_Callback(hObject, eventdata, handles)
% hObject    handle to edit1 (see GCBO)
% eventdata  reserved - to be defined in a future version of MATLAB
% handles    structure with handles and user data (see GUIDATA)

% Hints: get(hObject,'String') returns contents of edit1 as text
%        str2double(get(hObject,'String')) returns contents of edit1 as a double
%handles.edit1 = str2double(get(hObject,'String'));

% --- Executes during object creation, after setting all properties.
```

```
function edit1_CreateFcn(hObject, eventdata, handles)
% hObject    handle to edit1 (see GCBO)
% eventdata  reserved - to be defined in a future version of MATLAB
% handles    empty - handles not created until after all CreateFcns called

% Hint: edit controls usually have a white background on Windows.
%       See ISPC and COMPUTER.
if ispc && isequal(get(hObject,'BackgroundColor'),
 get(0,'defaultUicontrolBackgroundColor'))
    set(hObject,'BackgroundColor','white');
end



function edit2_Callback(hObject, eventdata, handles)
% hObject    handle to edit2 (see GCBO)
% eventdata  reserved - to be defined in a future version of MATLAB
% handles    structure with handles and user data (see GUIDATA)

% Hints: get(hObject,'String') returns contents of edit2 as text
%        str2double(get(hObject,'String')) returns contents of edit2 as a double


% --- Executes during object creation, after setting all properties.
function edit2_CreateFcn(hObject, eventdata, handles)
% hObject    handle to edit2 (see GCBO)
% eventdata  reserved - to be defined in a future version of MATLAB
% handles    empty - handles not created until after all CreateFcns called

% Hint: edit controls usually have a white background on Windows.
%       See ISPC and COMPUTER.
if ispc && isequal(get(hObject,'BackgroundColor'),
 get(0,'defaultUicontrolBackgroundColor'))
    set(hObject,'BackgroundColor','white');
```

```
end


% --- Executes on button press in pushbutton1.
function pushbutton1_Callback(hObject, eventdata, handles)
% hObject    handle to pushbutton1 (see GCBO)
% eventdata  reserved - to be defined in a future version of MATLAB
% handles    structure with handles and user data (see GUIDATA)

% Display the surface plot of current data
% Creating data to plot
radio1 = get(handles.radiobutton1,'Value');
radio2 = get(handles.radiobutton2,'Value');
radio3 = get(handles.radiobutton3,'Value');
radio4 = get(handles.radiobutton4,'Value');
size = str2double(get(handles.Size1,'String'));
step = str2double(get(handles.edit4,'String'));
R = str2double(get(handles.R,'String'));
L = str2double(get(handles.edit1,'String'));
D = str2double(get(handles.Period1,'String'));
[x,y]=meshgrid([-size:size/step:size]);
fi = atan2(y,x);
K = 2*pi/(D);

if radio1 == 1
   n = length(x);
   nn= n/2 - 500;
   test = sin(L*fi+K*x);
    for h = 1:n
       for j  = 1:n
           if (test(h,j) >=0)
               T(h,j) = 1;
           else
               T(h,j) = 0;
```

```
            end;
        end;
    end
clear h j n nn;
end

if radio2 == 1
    H = (1/(2*pi))*mod((L.*fi-K.*x),(2*pi));
    clear fi;
    T = exp(i*R*D.*H);
    T = real(T);
end

if radio3 == 1
    T = (L.*fi);
    T = (1/(2*pi))*mod(T,2*pi);
end

if radio4 == 1
    num = str2double(get(handles.Array,'String'));
    r = size/2;
    fi1 = atan2(y+r,x+r);
    fi2 = atan2(y-r,x-r);
    fi3 = atan2(y-r,x+r);
    fi4 = atan2(y+r,x-r);
    Theta1 = (L.*fi1);Theta1 = mod(Theta1,2*pi);
    Theta2 = (L.*fi2);Theta2 = mod(Theta2,2*pi);
    Theta3 = (L.*fi3);Theta3 = mod(Theta3,2*pi);
    Theta4 = (L.*fi4);Theta4 = mod(Theta4,2*pi);

    T = 100*(Theta1 + Theta2 + Theta3 + Theta4)./num;
end

handles.current_data = T;
```

```
guidata(hObject,handles);
surf(x,y,T)
view([90,90])
shading interp
colormap gray

function Period1_Callback(hObject, eventdata, handles)
% hObject    handle to Period1 (see GCBO)
% eventdata  reserved - to be defined in a future version of MATLAB
% handles    structure with handles and user data (see GUIDATA)

%Hints: get(hObject,'String') returns contents of Period1 as text
%        str2double(get(hObject,'String')) returns contents of Period1 as a double




% --- Executes during object creation, after setting all properties.
function Period1_CreateFcn(hObject, eventdata, handles)
% hObject    handle to Period1 (see GCBO)
% eventdata  reserved - to be defined in a future version of MATLAB
% handles    empty - handles not created until after all CreateFcns called

% Hint: edit controls usually have a white background on Windows.
%       See ISPC and COMPUTER.
if ispc && isequal(get(hObject,'BackgroundColor'),
get(0,'defaultUicontrolBackgroundColor'))
    set(hObject,'BackgroundColor','white');
end



function Size1_Callback(hObject, eventdata, handles)
% hObject    handle to Size1 (see GCBO)
```

```
% eventdata  reserved - to be defined in a future version of MATLAB
% handles    structure with handles and user data (see GUIDATA)

% Hints: get(hObject,'String') returns contents of Size1 as text
%        str2double(get(hObject,'String')) returns contents of Size1 as a double


% --- Executes during object creation, after setting all properties.
function Size1_CreateFcn(hObject, eventdata, handles)
% hObject    handle to Size1 (see GCBO)
% eventdata  reserved - to be defined in a future version of MATLAB
% handles    empty - handles not created until after all CreateFcns called

% Hint: edit controls usually have a white background on Windows.
%       See ISPC and COMPUTER.
if ispc && isequal(get(hObject,'BackgroundColor'),
get(0,'defaultUicontrolBackgroundColor'))
    set(hObject,'BackgroundColor','white');
end


% --- Executes on button press in Close.
function Close_Callback(hObject, eventdata, handles)
% hObject    handle to Close (see GCBO)
% eventdata  reserved - to be defined in a future version of MATLAB
% handles    structure with handles and user data (see GUIDATA)

% Close the GUI
clear all;
close;



function edit4_Callback(hObject, eventdata, handles)
```

```
% hObject    handle to edit4 (see GCBO)
% eventdata  reserved - to be defined in a future version of MATLAB
% handles    structure with handles and user data (see GUIDATA)

% Hints: get(hObject,'String') returns contents of edit4 as text
%        str2double(get(hObject,'String')) returns contents of edit4 as a double


% --- Executes during object creation, after setting all properties.
function edit4_CreateFcn(hObject, eventdata, handles)
% hObject    handle to edit4 (see GCBO)
% eventdata  reserved - to be defined in a future version of MATLAB
% handles    empty - handles not created until after all CreateFcns called

% Hint: edit controls usually have a white background on Windows.
%       See ISPC and COMPUTER.
if ispc && isequal(get(hObject,'BackgroundColor'),
get(0,'defaultUicontrolBackgroundColor'))
    set(hObject,'BackgroundColor','white');
end


% --- Executes during object creation, after setting all properties.
function uipanel3_CreateFcn(hObject, eventdata, handles)
% hObject    handle to uipanel3 (see GCBO)
% eventdata  reserved - to be defined in a future version of MATLAB
% handles    empty - handles not created until after all CreateFcns called


% --------------------------------------------------------------------
function uipanel3_SelectionChangeFcn(hObject, eventdata, handles)
% hObject    handle to uipanel3 (see GCBO)
% eventdata  reserved - to be defined in a future version of MATLAB
% handles    structure with handles and user data (see GUIDATA)
```

```
switch get(hObject,'Tag')   % Get Tag of selected object
    case 'radiobutton4'
        set(handles.Array , 'Visible', 'on');
        set(handles.text9 , 'Visible', 'on');
    case 'radiobutton1'
        set(handles.Array , 'Visible', 'off');
        set(handles.text9 , 'Visible', 'off');
    case 'radiobutton2'
        set(handles.Array , 'Visible', 'off');
        set(handles.text9 , 'Visible', 'off');
    case 'radiobutton3'
        set(handles.Array , 'Visible', 'off');
        set(handles.text9 , 'Visible', 'off');
end



function rot_Callback(hObject, eventdata, handles)
% hObject    handle to rot (see GCBO)
% eventdata  reserved - to be defined in a future version of MATLAB
% handles    structure with handles and user data (see GUIDATA)

% Hints: get(hObject,'String') returns contents of rot as text
%        str2double(get(hObject,'String')) returns contents of rot as a double


% --- Executes during object creation, after setting all properties.
function rot_CreateFcn(hObject, eventdata, handles)
% hObject    handle to rot (see GCBO)
% eventdata  reserved - to be defined in a future version of MATLAB
% handles    empty - handles not created until after all CreateFcns called

% Hint: edit controls usually have a white background on Windows.
```

```
%       See ISPC and COMPUTER.
if ispc && isequal(get(hObject,'BackgroundColor'),
get(0,'defaultUicontrolBackgroundColor'))
    set(hObject,'BackgroundColor','white');
end


% --- Executes on button press in rotate.
function rotate_Callback(hObject, eventdata, handles)
% hObject    handle to rotate (see GCBO)
% eventdata  reserved - to be defined in a future version of MATLAB
% handles    structure with handles and user data (see GUIDATA)
rot = str2double(get(handles.rot,'String'));

view([rot,90])


% --------------------------------------------------------------------
function File_Callback(hObject, eventdata, handles)
% hObject    handle to File (see GCBO)
% eventdata  reserved - to be defined in a future version of MATLAB
% handles    structure with handles and user data (see GUIDATA)


% --------------------------------------------------------------------
function Exit_Callback(hObject, eventdata, handles)
% hObject    handle to Exit (see GCBO)
% eventdata  reserved - to be defined in a future version of MATLAB
% handles    structure with handles and user data (see GUIDATA)
close;


% --------------------------------------------------------------------
function Save_Callback(hObject, eventdata, handles)
```

```
% hObject    handle to Save (see GCBO)
% eventdata  reserved - to be defined in a future version of MATLAB
% handles    structure with handles and user data (see GUIDATA)
T = handles.current_data;
filename = uiputfile('*.jpg','Save Image As:');
imwrite(T,filename,'jpg')

% --- Executes on button press in Memory.
function Memory_Callback(hObject, eventdata, handles)
% hObject    handle to Memory (see GCBO)
% eventdata  reserved - to be defined in a future version of MATLAB
% handles    structure with handles and user data (see GUIDATA)
clear all


% --------------------------------------------------------------------
function Open_Callback(hObject, eventdata, handles)
% hObject    handle to Open (see GCBO)
% eventdata  reserved - to be defined in a future version of MATLAB
% handles    structure with handles and user data (see GUIDATA)

filename = uigetfile('*.jpg','Open Image:');
T = imread(filename,'jpg');
imshow(T)


% --------------------------------------------------------------------
function Exit_M_Callback(hObject, eventdata, handles)
% hObject    handle to Exit_M (see GCBO)
% eventdata  reserved - to be defined in a future version of MATLAB
% handles    structure with handles and user data (see GUIDATA)


% --------------------------------------------------------------------
```

```
function Exit_B_Callback(hObject, eventdata, handles)
% hObject    handle to Exit_B (see GCBO)
% eventdata  reserved - to be defined in a future version of MATLAB
% handles    structure with handles and user data (see GUIDATA)
clear all;
close;


% --- Executes on selection change in Lvalue.
function Lvalue_Callback(hObject, eventdata, handles)
% hObject    handle to Lvalue (see GCBO)
% eventdata  reserved - to be defined in a future version of MATLAB
% handles    structure with handles and user data (see GUIDATA)

% Hints: contents = get(hObject,'String') returns Lvalue contents as cell array
%        contents{get(hObject,'Value')} returns selected item from Lvalue


% --- Executes during object creation, after setting all properties.
function Lvalue_CreateFcn(hObject, eventdata, handles)
% hObject    handle to Lvalue (see GCBO)
% eventdata  reserved - to be defined in a future version of MATLAB
% handles    empty - handles not created until after all CreateFcns called

% Hint: popupmenu controls usually have a white background on Windows.
%       See ISPC and COMPUTER.
if ispc && isequal(get(hObject,'BackgroundColor'),
get(0,'defaultUicontrolBackgroundColor'))
    set(hObject,'BackgroundColor','white');
end



function Array_Callback(hObject, eventdata, handles)
```

```
% hObject    handle to Array (see GCBO)
% eventdata  reserved - to be defined in a future version of MATLAB
% handles    structure with handles and user data (see GUIDATA)

% Hints: get(hObject,'String') returns contents of Array as text
%        str2double(get(hObject,'String')) returns contents of Array as a double


% --- Executes during object creation, after setting all properties.
function Array_CreateFcn(hObject, eventdata, handles)
% hObject    handle to Array (see GCBO)
% eventdata  reserved - to be defined in a future version of MATLAB
% handles    empty - handles not created until after all CreateFcns called

% Hint: edit controls usually have a white background on Windows.
%       See ISPC and COMPUTER.
if ispc && isequal(get(hObject,'BackgroundColor'),
get(0,'defaultUicontrolBackgroundColor'))
    set(hObject,'BackgroundColor','white');
end


% --- Executes on selection change in zoom.
function zoom_Callback(hObject, eventdata, handles)
% hObject    handle to zoom (see GCBO)
% eventdata  reserved - to be defined in a future version of MATLAB
% handles    structure with handles and user data (see GUIDATA)

% Hints: contents = get(hObject,'String') returns zoom contents as cell array
%        contents{get(hObject,'Value')} returns selected item from zoom

val = get(hObject,'Value');
switch val
case 1
```

```
    zoom(1)
case 2
    zoom(0.25)
case 3
    zoom(0.5)
case 4
    zoom(0.75)
case 5
    zoom(1.0)
case 6
    zoom(1.25)
case 7
    zoom(1.5)
case 8
    zoom(1.75)
case 9
    zoom(2)
end

% --- Executes during object creation, after setting all properties.
function zoom_CreateFcn(hObject, eventdata, handles)
% hObject    handle to zoom (see GCBO)
% eventdata  reserved - to be defined in a future version of MATLAB
% handles    empty - handles not created until after all CreateFcns called

% Hint: popupmenu controls usually have a white background on Windows.
%       See ISPC and COMPUTER.
if ispc && isequal(get(hObject,'BackgroundColor'),
get(0,'defaultUicontrolBackgroundColor'))
    set(hObject,'BackgroundColor','white');
end
```

```
function R_Callback(hObject, eventdata, handles)
% hObject    handle to R (see GCBO)
% eventdata  reserved - to be defined in a future version of MATLAB
% handles    structure with handles and user data (see GUIDATA)

% Hints: get(hObject,'String') returns contents of R as text
%        str2double(get(hObject,'String')) returns contents of R as a double


% --- Executes during object creation, after setting all properties.
function R_CreateFcn(hObject, eventdata, handles)
% hObject    handle to R (see GCBO)
% eventdata  reserved - to be defined in a future version of MATLAB
% handles    empty - handles not created until after all CreateFcns called

% Hint: edit controls usually have a white background on Windows.
%       See ISPC and COMPUTER.
if ispc
    set(hObject,'BackgroundColor','white');
else
    set(hObject,'BackgroundColor',
     get(0,'defaultUicontrolBackgroundColor'));
end
```

Appendix B

List of Publications

H. I. Sztul, D. A. Nolan, G. Milione, X. Chen, J. Kohn, and R. R. Alfano, "Hybrid-polarization beam generation from spun optical fiber," Optics Letters (submitted August 2008).

H. I. Sztul and R. R. Alfano, "The Poynting vector and angular momentum of Airy beams," Opt. Express 16, 9411-9416 (2008).

I. Zeylikovich, **H. I. Sztul**, V. Kartazaev, T. Le, and R. R. Alfano, "Ultrashort Laguerre-Gaussian pulses with angular and group velocity dispersion compensation," Opt. Lett. 32, 2025-2027 (2007).

H. I. Sztul, V. Kartazayev, and R. R. Alfano, "Laguerre-Gaussian supercontinuum," Opt. Lett. 31, 2725-2727 (2006).

H. I. Sztul and R. R. Alfano, "Double-slit interference with Laguerre-Gaussian beams," Opt. Lett. 31, 999-1001 (2006).

E. J. Galvez, P. R. Crawford, **H. I. Sztul**, M. J. Pysher, P. J. Haglin, and R. E. Williams, "Geometric Phase Associated with Mode Transformations of Optical Beams Bearing Orbital Angular Momentum," Phys. Rev. Lett. 90, 203901 (2003).

Patents

R. R. Alfano, W. B. Wang, **H. I. Sztul**, and Y. Budansky, "Methods and systems for on-board realtime detection of ice formation on surfaces of airplanes, UAVs and other vehicles and structures," US Patent #7312713 Issued Dec. 25, 2007.

R. R. Alfano, **H. I. Sztul**, G. Milione, X. Chen, J. Kohn, and D. A. Nolan, "Cylindrically polarized mode converter," Provisional Patent Application Filed July 2008.

Presentations

H. I. Sztul and R. R. Alfano, "The Poynting Vector and Angular Momentum of Airy Beams," Frontiers in Optics (FiO)/Laser Science XXIV Conference, JWA23, October 9-23, 2008, Rochester, NY.

I. Zeylikovich, **H. I. Sztul**, V. Kartazaev, T. Le, and R. R. Alfano, "Ultrashort Lagguere-Gaussian Pulses With Angular and Group Velocity Dispersion Compensation," CLEO/QELS, May 22, 2007, Baltimore, Maryland.

H. I. Sztul, V. Kartazayev, and R. R. Alfano, "Laguerre-Gaussian supercontinuum," Photonics West, Proceedings of SPIE, Volume 6483, January 2007, San Jose, CA.
H. I. Sztul, V. Kartazayev, and R. R. Alfano, "Laguerre-Gaussian Supercontinuum," in Frontiers in Optics, OSA Technical Digest (CD) (Optical Society of America, 2006), paper JThB5.

Bibliography

[1] R. A. Beth, "Mechanical Detection and Measurement of the Angular Momentum of Light," Phys. Rev. 50, 115 (1936).

[2] L. Allen, M. J. Padgett, M. Babiker, Progress in Optics XXXIX (1999).

[3] J. F. Nye and M. V. Berry,"Dislocations in Wave Trains," Proceedings of the Royal Society of London. Series A, Mathematical and Physical Sciences, Vol. 336, p. 165-190 (1974).

[4] L. Allen, M. W. Beijersbergen, R. J. C. Spreeuw, and J. P. Woerdman, "Orbital angular momentum of light and the transformation of Laguerre-Gaussian laser modes," Phys. Rev. A 45, 8185 - 8189 (1992).

[5] H. He, M. E. Friese, N. R. Heckenberg, and H. Rubinsztein-Dunlop, " Direct Observation of Transfer of Angular Momentum to Absorptive Particles from a Laser Beam with a Phase Singularity," Physical Review Letters 75 826 (1995).

[6] M. E. J. Friese, J. Enger, H. Rubinsztein-Dunlop, and N. R. Heckenberg, "Optical angular-momentum transfer to trapped absorbing particles," Phys. Rev. A 54, 1593 - 1596 (1996).

[7] M. F. Andersen, C. Ryu, Pierre Clad, Vasant Natarajan, A. Vaziri, K. Helmerson, and W. D. Phillips, "Quantized Rotation of Atoms from Photons with Orbital Angular Momentum," Phys. Rev. Lett. 97, 170406 (2006).

[8] K. C. Wright, L. S. Leslie, and N. P. Bigelow, "Optical control of the internal and external angular momentum of a Bose-Einstein condensate," Phys. Rev. A 77, 041601(R) (2008).

[9] A. Vazir, G. Weihs, and A. Zeilinger, J. Opt. B Quantum Semiclass. Opt. 4, S47 (2002).

[10] Gibson, J. Courtial, M. Padgett, M. Vasnetsov, V. Pas'ko, S. Barnett, and S. Franke-Arnold, "Free-space information transfer using light beams carrying orbital angular momentum," Opt. Express 12, 5448-5456 (2004).

[11] A. Seigman, "Lasers", chapter Wave Optics and Gaussian Beams, pages 626–685.

[12] J.D. Jackson, "Classical Elecrodynamics" Wiley, New York (1975).

[13] L. Allen and M.J. Padgett, "The poynting vector in laguerre-gaussian beams and the interpretation of their angular momentum density," Opt. Comm., 184, 67-71 (2000).

[14] M.V. Berry, "Paraxial beams of spinning light," In M.S. Soskin and M.V. Vasnetsov, editors, *Singular Optics*,v. 3487, p. 6-11. SPIE (1998).

[15] E. Galvez, "Gaussian beams in the optics course," Am. Jour. Phys., 74 335 (2006).

[16] C.J. Flood, G. Giuliani, H.M. van Driel, "Preferential operation of an end-pumped Nd: YAG laser in high-order Laguerre-Gauss modes," Opt. Lett. 15, 215 (1990).

[17] M. Padgett, J. Arlt, N. Simpson, and L. Allen, "An experiment to observe the intensity and phase structure of LaguerreGaussian laser modes," Am. J. Phys. 64, 77-82 (1996).

[18] V. V. Kotlyar, A. A. Almazov, S. N. Khonina, V. A. Soifer, H. Elfstrom, and J. Turunen, "Generation of phase singularity through diffracting a plane or Gaussian beam by a spiral phase plate," J. Opt. Soc. Am. A 22, 849-861 (2005).

[19] K. Sueda, G. Miyaji, N. Miyanaga, and M. Nakatsuka, "Laguerre-Gaussian beam generated with a multilevel spiral phase plate for high intensity laser pulses," Opt. Express 12, 3548-3553 (2004).

[20] N.R. Heckenberg, R. McDuff, C.P. Smith, and A.G. White, "Generation of optical phase singularities by computer generated holograms," Opt. Lett. 17 (1992).

[21] J. Arlt, K. Dholakia, L. Allen, and M.J. Padgett, "The production of multi-ringed laguerre-gaussian modes by computer genterated holograms," J. Mod. Opt., 45 (1998).

[22] T. Young, Philos. Trans. R. Soc. London **12,** 387 (1802).

[23] Claus Jnsson, Z. Phys. **161,** 454 (1961).

[24] Claus Jnsson, Am. J. Phys. **42,** 4 (1974).

[25] A. Zeilinger, R. Ghler, C.G. Shull, W. Treimer and W. Mampe, Rev. Mod. Phys. **60,** 10671073 (1988).

[26] O. Carnal and J. Mlynek, Phys. Rev. Lett. **66,** 26892692 (1991).

[27] L. Allen, M. J. Padgett, M. Babiker, Progress in Optics XXXIX, pp. 291-372 (1999).

[28] L. Allen, M. W. Beijersbergen, R. J. C. Spreeuw, and J. P. Woerdman, Phys. Rev. A **45,** 8185 (1992).

[29] M.J. Padgett, J. Arlt, and N. Simpson. American Journal of Physics, **64**(1):7782, (1996).

[30] H. I. Sztul and R. R. Alfano, "Double-slit interference with Laguerre-Gaussian beams," Opt. Lett. **31,** 999-1001 (2006).

[31] J. M. Vaughan and D. V. Willetts, Opt. Commun. **30,** 263 (1979).

[32] N. R. Heckenberg, R. McDuff, C. P. Smith, and A. G. White, Opt. Lett. **17,** 221 (1992).

[33] N. R. Heckenberg, R. McDuff, C. P. Smith, H. Rubinsztein-Dunlop, and M. J. Wegener, Opt. Quantum Electron. **24,** S951 (1992).

[34] M. Born and E. Wolf, *Principles of Optics*, 7th Ed., Cambridge University Press, New York, Chapter 7 (1999).

[35] E. J. Galvez, P. R. Crawford, H. I. Sztul, M. J. Pysher, P. J. Haglin, and R. E. Williams, Phys. Rev. Lett. **90,** 203901 (2003).

[36] G. B. Jung, K. Kanaya, and T. Omatsu, "Highly efficient phase-conjugation of a 1 m pico-second Laguerre-Gaussian beam," Opt. Express 14, 2250-2255 (2006).

[37] I. G. Mariyenko, J. Strohaber, and C. J. G. J. Uiterwaal, "Creation of optical vortices in femtosecond pulses", Opt. Exp. **13,** 7599 (2005).

[38] K. Bezuhanov, A. Dreischuh, G. G. Paulus, M. G. Schtzel and H. Walther, "Vortices in femtosecond laser fields," Opt. Lett. **29,** 1942 (2004).

[39] I. Zeylikovich, H. I. Sztul, V. Kartazaev, T. Le, and R. R. Alfano, "Ultrashort Laguerre-Gaussian pulses with angular and group velocity dispersion compensation," Opt. Lett. 32, 2025-2027 (2007).

[40] L. Allen, M. J. Padgett, M. Babiker, Progress in Optics XXXIX, pp. 291-372 (1999).

[41] A. Vazir, G. Weihs, and A. Zeilinger, J. Opt. B Quantum Semiclass. Opt. **4,** S47 (2002).

[42] A. Mair, A. Vaziri, G. Weihs and A. Zeiligner, Nature **412,** 313 (2001).

[43] L. Allen, M. W. Beijersbergen, R. J. C. Spreeuw, and J. P. Woerdman, Phys. Rev. A **45,** 8185 (1992).

[44] G. Gibson, J. Courtial, M. Padgett, M. Vasnetsov, V. Pas'ko, S. Barnett, and S. Franke-Arnold, Opt. Ex. **12,** 5448-5456 (2004)

[45] M.S. Soskin, P.V. Polyanskii, and O.O. Arkhelyuk, New J. Phys. **6,**196 (2004).

[46] J. Leach and M.J. Padgett, New J. Phys. **5,**154 (2003).

[47] R.R. Alfano and S.L. Shapiro, Phys. Rev. Lett. **24,** 592 (1970).

[48] R. R. Alfano, The Supercontinuum laser source (2nd ed.), Springer, New York (2006).

[49] J. M. Vaughan and D. V. Willetts, Opt. Comm. **30,** 263 (1979).

[50] N. R. Heckenberg, R. McDuff, C. P. Smith, and A. G. White, Opt. Lett.**17,** 221 (1992).

[51] N. R. Heckenberg, R. McDuff, C. P. Smith, H. Rubinsztein-Dunlop, and M. J. Wegener, Opt. Quantum Electron. **24,** S951 (1992).

[52] L.T. Vuong, T.D. Grow, A. Ishaaya, A.L. Gaeta, G.W. 't Hooft, E.R. Eliel, and G. Fibich, Phys. Rev. Lett. **96,** 133901 (2006)

[53] K. Bezuhanov, A. Dreischuh, G. G. Paulus, M. G. Schtzel, and H. Walther, "Vortices in femtosecond laser fields," Opt. Lett. **29,** 1942 (2004)

[54] P. Fischer, C. Brown, J. Morris, C. Lopez-Mariscal, E. Wright, W. Sibbett, and K. Dholakia, Opt. Ex. **13,** 6657 (2005).

[55] L. Wang, P. P. Ho, G. Liu, G. Zhang, and R. R. Alfano, "Ballistic 2-D imaging through scattering wall using an ultrafast Kerr gate", Science 253, 769-771 (1991).

[56] D. Huang, E. A. Swanson, C. P. Lin, J. S. Schuman, W. G. Stinson, W. Chang, M. R. Hee, T. Flotte, K. Gregory, C. A. Puliafito, and J. G. Fujimoto, "Optical coherent tomography", Science 254, 1178-1181 (1991).

[57] K M. Yoo and R. R. Alfano, "Time-resolved coherent and incoherent components of forward light scattering in random media", Opt. Lett. 15, 320-322 (1990).

[58] M. A. OLeary, D. A. Boas, B. Chance, and A. G. Yodh, "Experimental images of heterogeneous turbid media by frequency-domain diffusing-photon tomography", Opt. Lett. 20,426-428 (1995).

[59] Y. Guo, H. E. Savage, F. Liu, S. P. Schantz, P. P. Ho, and R. R. Alfano, "Subsurface tumor progression investigated by noninvasive optical second harmonic tomography", Proc. Natl. Acad. Sci. 96, 10854-10856 (1999).

[60] A. Schmidt, R. Corey, and P. Saulnier, "Imaging through random media by use of low-coherence optical heterodyning", Opt. Lett. 20, 404-406 (1995).

[61] J. J. Dolne, K. M. Yoo, F. Liu, and R. R. Alfano, "IR Fourier space gate and absorption imaging through random media", Lasers in the life Sci. 6, 131 (1994).

[62] P. Y. Gerligand, M. H. Smith, R. A. Chipman, "Polarimetric images of a cone", Opt. Express 4, 420-430 (1999).

[63] S. G. Demos, R. R. Alfano, "Optical polarization imaging", Appl. Opt. 36, 150-155 (1997).

[64] Ashkin, A., Dziedzic, J. M., Bjorkholm, J. E., and S. Chu, "Observation of a Single-Beam Gradient Force Optical Trap for Dielectrical Particles", Optics Letters 11, pp 288-290 (1986).

[65] P.W. Smith, A. Ashkin, and W. J. Tomlinson, "Four -wave mixing in an artificial Kerr medium," Opt. Lett. 6, 284 (1981).

[66] L. Novotny, M.R. Beversluis, K.S. Youngworth, and T.G. Brown, Phys. Rev. Lett. **86,** 5251 (2001).

[67] W. D. Kimura, G. H. Kim, R. D. Romea, L. C. Steinhauer, I. V. Pogorelsky, K. P. Kusche, R. C. Fernow, and X. Wang, Phys. Rev. Lett. **74,** 546 (1995).

[68] V. G. Niziev and A. V. Nesterov, J. Phys. D: Appl. Phys. 32, 1455-1461 (1999).

[69] R. Dorn, A. Quabis, and G. Leuchs, Phys. Rev. Lett. **91,** 233901 (2003).

[70] R. Oron, S. Blit, N. Davidson, A. A. Friesem, Z. Bomzon, and E. Hasman, Appl. Phys. Lett. **77,** 13322 (2000).

[71] C. Maurer, A. Jesacher, S. Frhapter, S. Bernet, and M. Ritsch-Marte, New Jour. Phys. **9,** 78 (2007).

[72] T. Grosjean, D. Courjon, M. Spajer, Opt. Comm. **203,** 1 (2002).

[73] G. Volpe and D. Petrov, Opt. Comm. **237,** 89 (2004).

[74] L. Allen, M. J. Padgett, M. Babiker, Progress in Optics XXXIX, pp. 291-372 (1999).

[75] H.A. Haus, "Waves and Fields in Optoelectronics" (Prentice Hall, Englewood Cliffs, NJ, 1984).

[76] L. Allen, M. J. Padgett, and M. Babiker, Progress in Optics XXXIX, pp. 291-372 (1999).

[77] J. Durnin, J.J. Miceli, and J.H. Eberly, Phys. Rev. Lett. **58,** 1499 (1987).

[78] J. Durnin, J. Op. Soc. Am. A **4,** 651 (1987).

[79] M.V. Berry and N.L. Balazs, "Nonspreading wave packets," Am. J. Phys. **47,** 264 (1979).

[80] G.A. Siviloglou, J. Broky, A. Dogariu, and D. N. Christodoulides, "Observation of Accelerating Airy Beams," Phys. Rev. Lett.**99,** 213901 (2007).

[81] G. A. Siviloglou and D. N. Chistodoulides, "Accelerating finite energy Airy beams," Opt. Lett. **32,** 979 (2007).

[82] D. M. Greenberger, "Comment on 'Non-Spreading Wave Packets', " Am. J. Phys. **48,** 256 (1980).

[83] L. Torner, J.P. Torres, and S. Carrasco, "Digital spiral imaging," Opt. Exp. **13,** 873 (2005).

[84] J.D. Jackson, Classical Electrodynamics, Wiley, New York, 1962.

[85] Max Born and Emil Wolf, Principles of Optics, 7th Ed., Cambridge University Press, Cambridge, 1999.

[86] L. Allen and M.J. Padgett, "The Poynting vector in Laguerre-Gaussian beams and the interpretation of their angular momentum desnity," Opt. Comm. **184,** 67-71 (2000).

[87] H.I. Sztul and R. R. Alfano, "Double-slit interference with Laguerre-Gaussian beams," Opt. Lett. **31,** 999-1001 (2006).

[88] M. V. Vasnetsov, J. P. Torres, D. V. Petrov, and L. Torner, "Observation of the orbital angular momentum spectrum of a light beam ," Opt. Lett. **28,** 2285-2287 (2003)